POLITECNICO
MILANO 1863

SCUOLA DI INGEGNERIA INDUSTRIALE
E DELL'INFORMAZIONE

Design and prototyping of a bioinspired manta ray robot with flexible fins

TESI DI LAUREA MAGISTRALE IN
MECHANICAL ENGINEERING-INGEGNERIA MECCANICA

Author: **Michele Tealdi**

Student ID:	10456245
Advisor:	Simone Cinquemani
Co-advisor:	Giovanni Bianchi
Academic Year:	2020-21

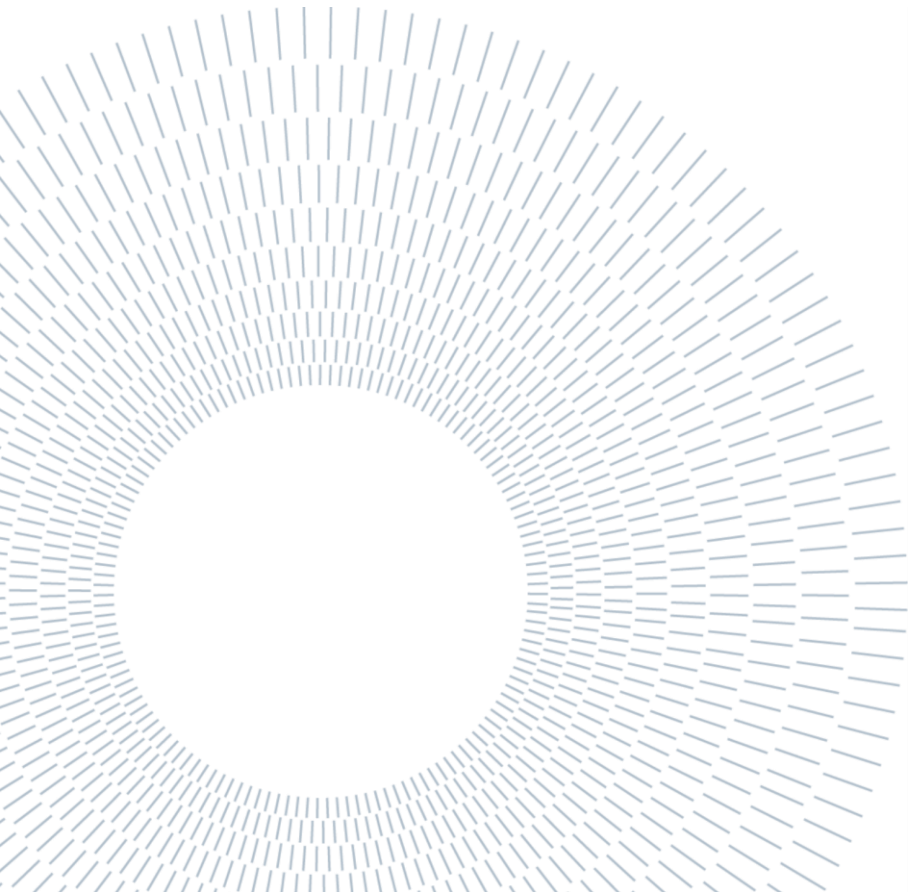

Abstract

This thesis explains the design process of bioinspired autonomous underwater vehicle.

Through natural evolution, fishes have adapted their swimming strategies to obtain high performances in terms of speed, agility and efficiency. Bioinspired design is useful to develop novel solutions to underwater propulsion which overcome the limitations of screw propellers, which are commonly applied for navigation.

The inspiration for this robot comes from the manta ray, as it is featured by very high maneuverability and efficiency with respect to other fishes. The robot replicates the characteristic movement of the manta ray while maintaining low dimensions and easiness of control. To achieve this result, the thrust is generated by the passive deformation of two pectoral fins attached to the frontal part of the central rigid body. One characteristic of this robot is the possibility to easily change the fins, so that several fin designs can be tested. In the rear part there are two rigid caudal fins used to control the stability of the robot. The electronic board Arduino controls the position of the digital servomotors which move the fins. The parameters and the data of the movement are easily accessible using a Wi-Fi connection.

The geometry of the flexible fins and their stiffness distribution are tuned to obtain a movement as similar as possible to its natural counterpart. However, they are still not optimized, and the development of this robot makes it possible to explore this research field.

Key-words: bioinspired design; manta ray robot; autonomous underwater vehicle; flexible fins.

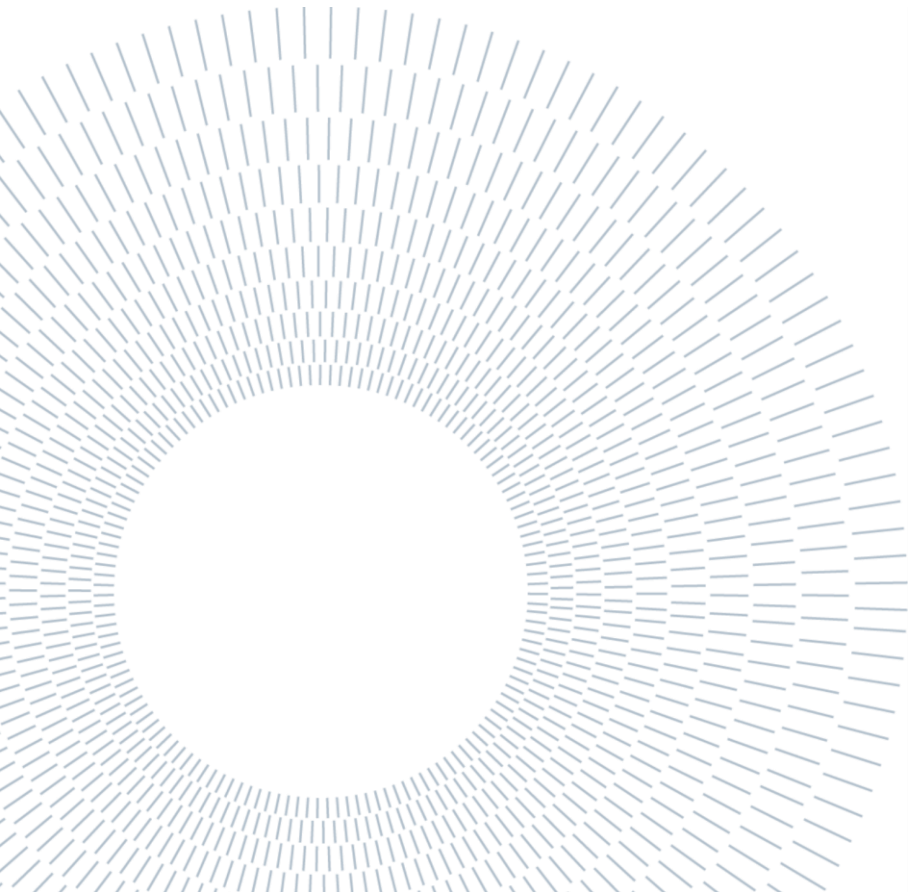

Abstract in lingua italiana

Questa tesi presenta il processo di progettazione di un veicolo subacqueo autonomo bioispirato.

Attraverso l'evoluzione naturale, i pesci hanno adattato le loro strategie di nuoto per ottenere grandi prestazioni in termini di velocità, agilità ed efficienza. La progettazione bioispirata è utile per sviluppare nuove soluzioni per la propulsione sottomarina che superino le limitazioni della propulsione a elica, solitamente applicata per la navigazione.

L'ispirazione per questo robot viene dalla manta, in quanto è dotata di manovrabilità ed efficienza molto alte in confronto agli altri pesci. Il robot imita il movimento caratteristico della manta mantenendo dimensioni ridotte e semplicità di controllo. Per ottenere questo risultato, la spinta è generata dalla deformazione passiva di due pinne pettorali collegate alla parte frontale del corpo rigido centrale. Una caratteristica di questo robot è la possibilità di cambiare facilmente le pinne, in modo tale che sia possibile testare diverse soluzioni progettuali. Nella parte posteriore ci sono due pinne caudali rigide usate per controllare la stabilità del robot. La scheda elettronica Arduino controlla la posizione dei servomotori digitali che muovono le pinne. I parametri e i dati del movimento sono facilmente accessibili usando una connessione Wi-Fi.

La geometria delle pinne flessibili e la distribuzione della rigidezza sono regolate per ottenere un movimento più simile possibile alla loro controparte naturale. In ogni caso non sono ancora ottimizzate, e lo sviluppo di questo robot consente di esplorare questo campo di ricerca.

Parole chiave: progettazione bioispirata; manta robot; veicolo subacqueo autonomo; pinne flessibili.

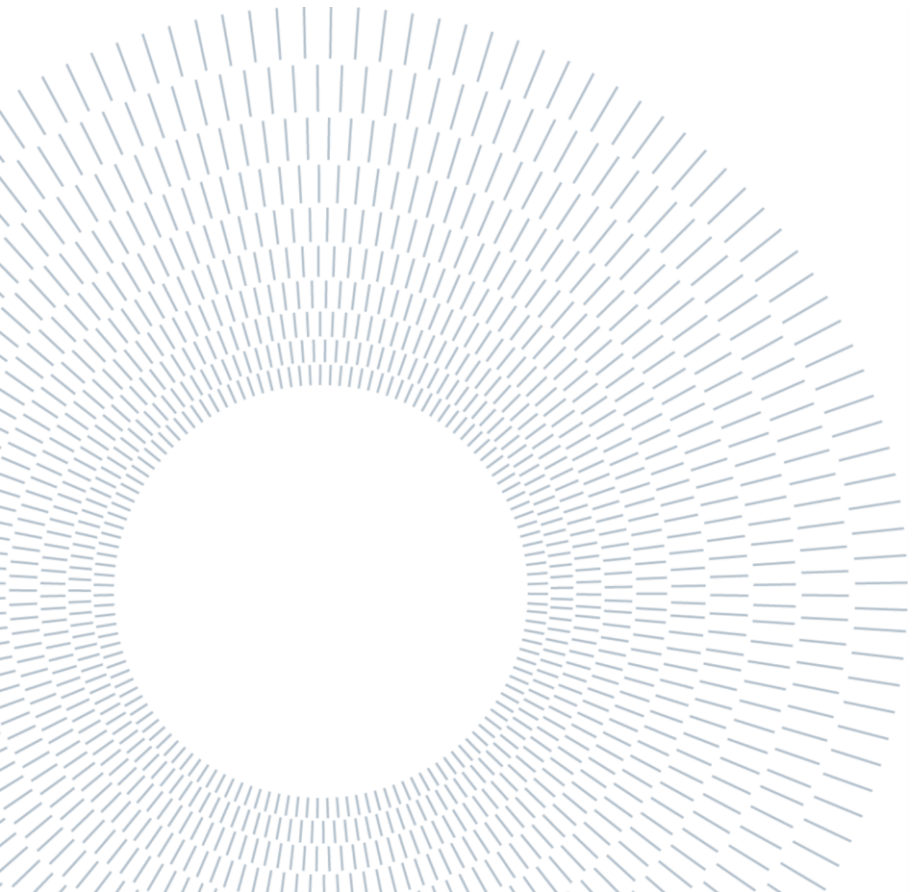

Contents

Introduction

This thesis presents the design and the manufacturing of a bioinspired autonomous underwater vehicle.

Bioinspired design is a way of designing objects taking advantage of the solutions available in nature. This can be applied to many fields, from materials to structures to movement generation. Movement in water is one of the fields where the nature is way more efficient than the human solutions applied so far.

Since the second half of the XIX century, boats, ships and submarines have been moved by screw propellers. This kind of motion allows to reach high velocities and cover great distances. On the other hand, the average efficiency of screw propellers is around 40%-50% [1]. The maneuverability of propellers vehicles is limited in acceleration and turning velocity [2]. The vehicles have big dimensions and produce a great acoustic and environmental noise [3]. Due to these characteristics, screw-propeller AUVs are not suitable for applications such as backdrop exploring and marine life monitoring.

Fishes, instead, have a swimming efficiency higher than 80%, and are able to handle sudden accelerations and perform sharp turns almost without losing velocity. A bioinspired design aims at understanding the physical characteristics that allow this swimming performances and at replicating them.

Fish can be roughly classified according to two characteristics of their movement: the first one is which body structures or fins are more active in generating thrust (BCF vs MPF). The second is the kind of movement, that can be undulatory or oscillatory[1] [4].

Body and/or Caudal Fin (BFC) locomotion is the one used by about 85% of the fish [5]. The locomotion is caused by the bending of their body. A propulsive wave moves backwards, up to the caudal fin, generating thrust.

---

[1] In nature, the distinction between undulatory and oscillatory movement can be fuzzy, while it is clearer in bionspired robots.

Median and/or Paired Fin (MPF) locomotion uses a combination of pectoral, pelvic, dorsal, and anal fins to produce thrust [6]. Compared with BCF propulsion, MPF locomotion can offer more precise maneuverability and higher propulsive efficiency at lower swimming velocity [7].

The second classification is based on the wavenumber of the normalized wavelength λ/C, where λ is the wavelength or the rearward travelling wave and C is the mean chord length of the fin. When the wave number is less than one, the movement is classified as oscillatory, otherwise it is undulatory [8].

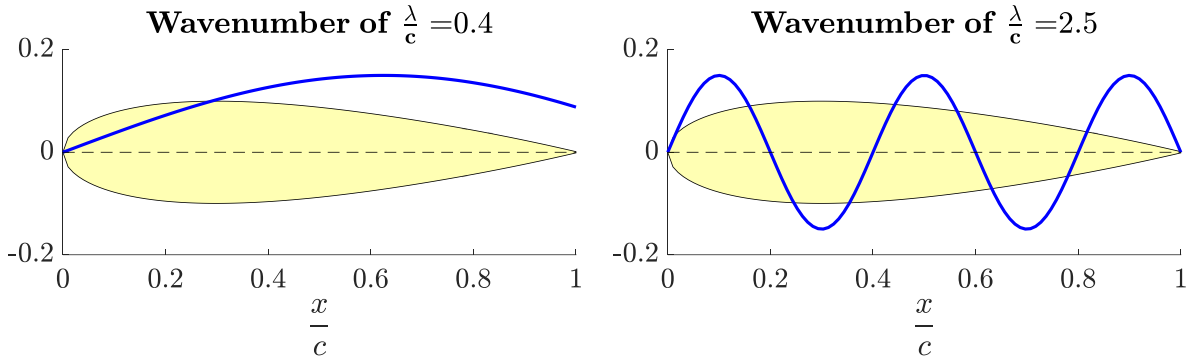

(a) Oscillatory wavenumber (b) Undulatory wavenumber

Figure 0.1: Oscillatory vs undulatory

The robot presented in this thesis, shown in Figure 0.2, is inspired to a manta ray. The manta is a fish characterized by large pectoral fins which generate the thrust similarly to the flapping of bird wings. It is classified as MPF locomotion with oscillatory movement (the wavenumber is around 0.4 [9]). The Manta was chosen for the great maneuverability and the low energy needed to generate thrust, as the aim of the robot is to obtain these two characteristics.

This thesis is organized as follows.

In chapter 1, “State of the art”, the prototypes developed in the last years are analyzed. The analysis is extended to all the MPF robots, from the undulatory ones to the manta ray-inspired ones. The main characteristics of manta ray shape and movement are analyzed as well in order to replicate them.

The other chapters are about four different aspects of the robot development. In chapter 2, “Mechanical design”, all the design choices are explained, starting from the working principle of the robot. In chapter 3, “Electronic components”, the choice and dimensioning of the robot electronics are addressed. Chapter 4, “Pectoral fins”, explains the design process of the pectoral fins. The prototype is supposed to be a

testbench on which to mount different fins to test them in the laboratory. For this reason, the pectoral fin design is independent from the design of the rest of the robot. In chapter 5, “Construction of the prototype”, the manufacturing of the robot is explained. Chapter 6, “Use of the robot” explains the strategies adopted to simplify the robot usage. Finally, in chapter 7 conclusions are drawn.

Figure 0.2: Photo of the finished robot

1. State of the art

1.1 Undulatory robots

1.1.1 Ghost Knifefish

The ghost knifefishes are a family, *Apteronotidae*, of ray-finned fishes in the order *Gymnotiformes*[2]. In detail, many projects are inspired by the Black ghost knifefish (*Apteronotus albifrons*), which is characterized by a long anal fin that starts at the base of the pectoral fins. This fin forms a wave that generates the movement, as shown in Figure 1.1

Figure 1.1: Black Ghost Knifefish[3]

Some prototypes, developed by Veenstra et al. [10] (Figure 1.2a), Epstein et al. [11] (Figure 1.2b), Liu and Curet [12] (Figure 1.2c), try to replicate this fin movement using

[2] From wikipedia web page, https://en.wikipedia.org/wiki/Ghost_knifefish, visited on 11/10/2021.
[3] Image taken from Pinterest web page, https://pin.it/17dP3GI, visited on 11/10/2021.

some rigid ribs moved by electric motors connected by flexible membrane. Their designs are different one from the other, but they all use ribs hinged to the body.

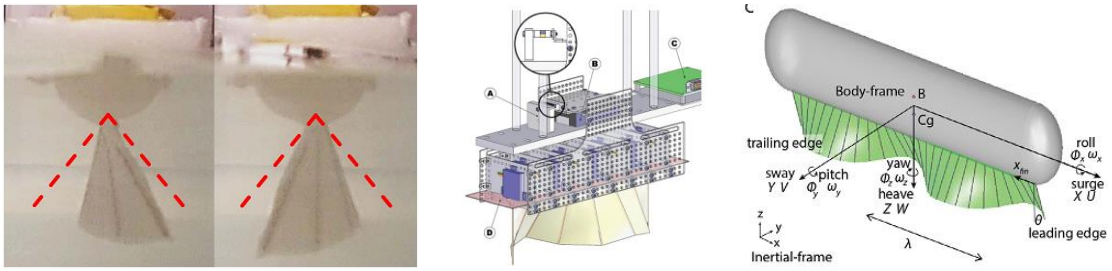

(a) Veentra ed al. [10] (b) Epstein et al. [11] (c) Liu and Curet [12]

Figure 1.2: Three undulatory robot prototypes

An interesting variation to this design is the one proposed by Low [4, 13]. In this project the ribs are connected to the body through a crank (see Figure 1.3). In this way they translate instead of rotating, and the amplitude of the generated wave is constant with respect to the vertical coordinate.

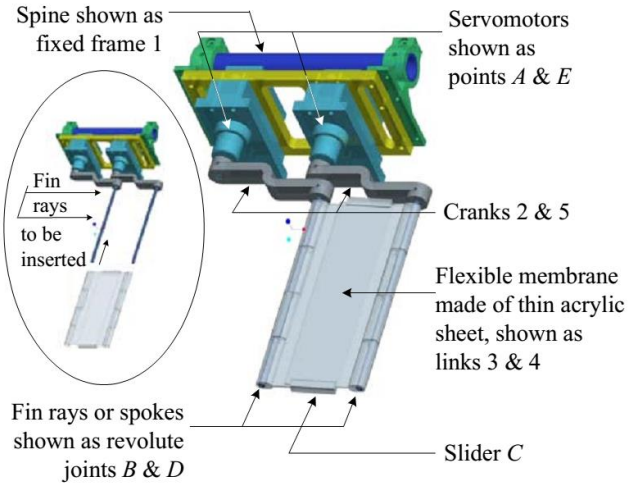

Figure 1.3: Undulatory mechanism proposed by Low

The same idea is applied by Hu et al. [14]. Anyway, their robot is inspired by the *Gymnarchus niloticus*. This species uses the dorsal fin to move instead of the anal fin. From the mechanical point of view, the design solution is the same, but it is upside-down (see Figure 1.4).

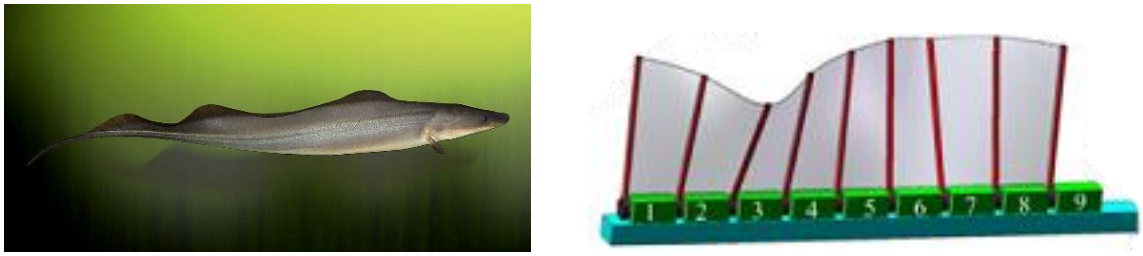

(a) *Gymnarchus niloticus*[4] (b) Robot by Hu et al. [14]

Figure 1.4: Bioinspired robot by Hu et al. compared to the fish

1.1.2 Bluespotted ray

The *Taeniura lymma*, commonly known as bluespotted ribbontail ray, is a species of stingray. Differently from the Manta Ray, the pectoral fins of these rays have a round shape and, while moving, they form a wave (see Figure 1.5)

Figure 1.5: A bluespotted ray[5]

The robots created by Zhang et al. [5], Ikeda et al. [15] and the one from Shang et al. [16] are inspired to this ray. The performed movement is similar to the one of the robots previously presented, but they have two fins placed on the sides of the body instead of only one.

[4] Image taken from Wikipedia web page, https://en.wikipedia.org/wiki/Gymnarchus, visited on 11/10/2021.

[5] Image taken from https://pixabay.com/photos/blue-spotted-stingrays-smelled-sea-1198567/, visited on 11/10/2021.

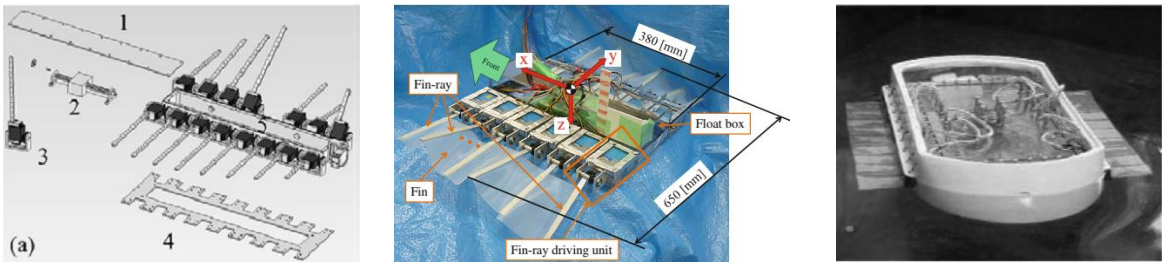

(a) by Zhang et al. [5] (b) Ikeda et al. [15] (c) Shang et al. [16]

Figure 1.6: Stingray inspired robots

1.1.3 Innovative designs

The round shape of the bluespotted ray inspired some innovative designs. Wang et al. [7] propose a prototype with a central circular body, twelve rods placed radially and a circular flexible membrane (see Figure 1.7). The axial-symmetry of the robot allows it to generate waves in any direction, and so it can change the direction of motion without performing maneuvers.

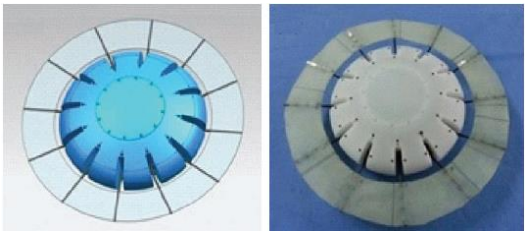

Figure 1.7: Circular robot by Wang et al. [7]

Khan and Smithmaitrie [17] proposed a similar idea, but their prototype is composed of only three fins. The whole robot is made from silicone and contributes to the propagation of the wave. The movement is transmitted using plastic tendons (see Figure 1.8). As in the previous design, the generated wave can travel in any of the three directions, allowing a great maneuverability.

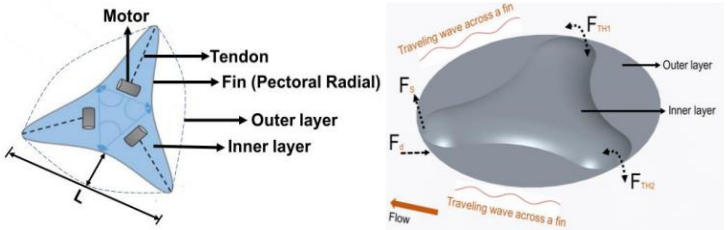

Figure 1.8: 3-fin robot proposed by Khan and Smithmaitrie [17]

1.2 Manta ray shape and movement

To develop a bioinspired robot, it is necessary first of all to understand the biological characteristics of the fishes and how they generate movement, in order to replicate them.

1.1.4 Shape

In literature mainly two different species of fish are analyzed: the manta ray (*Manta birostris*, Figure 1.9a) and the cownose ray (*Rhinoptera bonasus*, Figure 1.9b). They are quite similar for what concerns bioinspiration, so for our purposes it is possible to study both of them indifferently.

(a) Manta ray[6]

(b) Cownose ray

Figure 1.9: Rays

The shape of the manta body can be approximated to a diamond, as shown by Li et al. [3] (Figure 1.10.a,b). Cai et al. [18, 19] instead shows that the cownose ray body can be approximated as a rectangle, because it has some caudal fins almost as large as the head (Figure 1.11.a).

The pectoral fins have a shape similar to triangles. Li et al. [3] approximates it to a triangle and two trapezoids (Figure 1.10.c,d). Their bases are parallel to the fin base and forms an angle between 18° and 22°. This angle is important for the movement of the fin. Cai et al. [18, 19] instead prefers to approximate the shape of the cownose ray fin pointwise and to connect the points with linear segments.

[6] Image taken from https://www.bigfishexpeditions.com/trips/scuba-diving/giant-mantas-humpbacks/, visited on 16/10/2021.

Finally, Li et al. [3] defines the longitudinal profile with a custom airfoil shape (Figure 1.10.e) and gives no information about the fin section. On the other hand, Cai et al. [18, 19, 20] approximates three different sections of the cownose ray to three airfoils, according to NACA[7] normative.

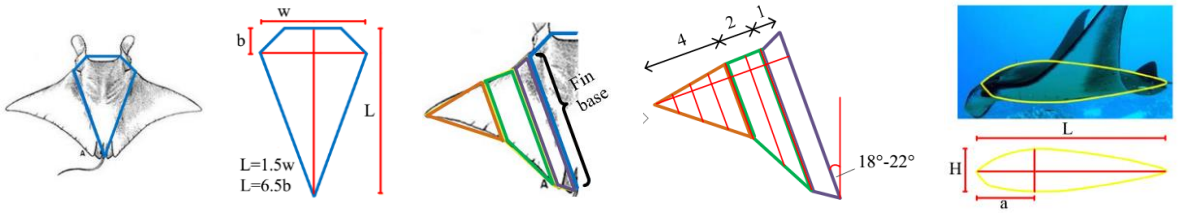

(a) (b) (c) (d) (e)

Figure 1.10: Shape of manta ray as approximated by Li et al. [3]

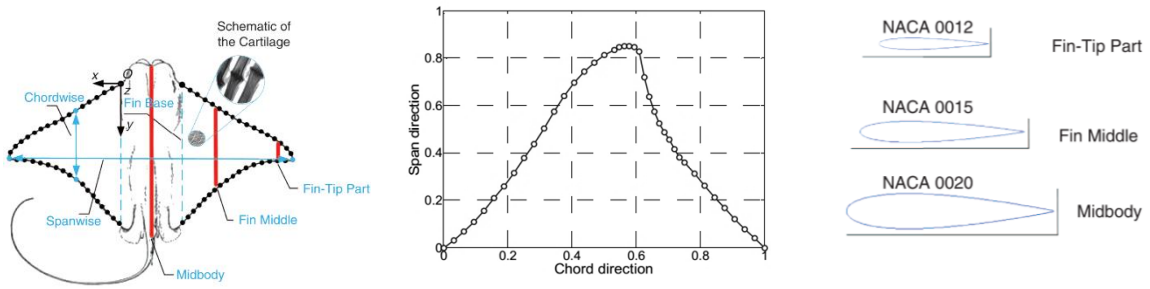

(a) (b) (c)

Figure 1.11: Shape of cownose ray as approximated by Cai et al.

The part of the pectoral fin connected to the body is called *fin base* (highlighted in blue in Figure 1.12). The front part of the fin is the *leading edge* (red in Figure 1.12), while the back part is the *trail edge* (green in Figure 1.12).

The waves propagate in the ray fin in two directions: the *chordwise* direction, parallel to the fin base (purple in Figure 1.12) and the perpendicular *spanwise* direction (orange in Figure 1.12). This way of propagating waves is directly connected to the particular fin skeleton structure, shown in Figure 1.13.

[7] National Advisory Committee for Aeronautics.

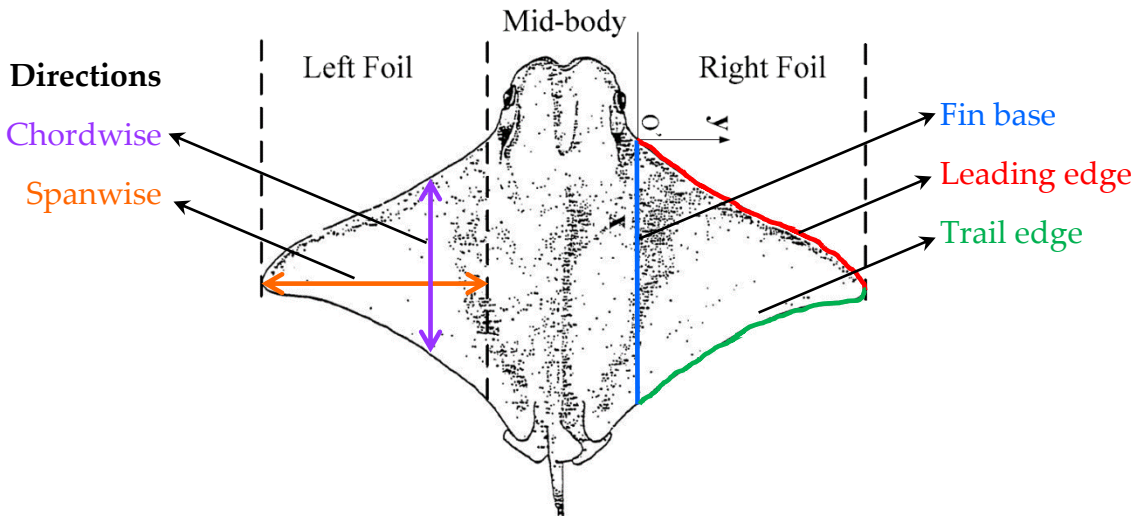

Figure 1.12: Manta ray with parts highlighted

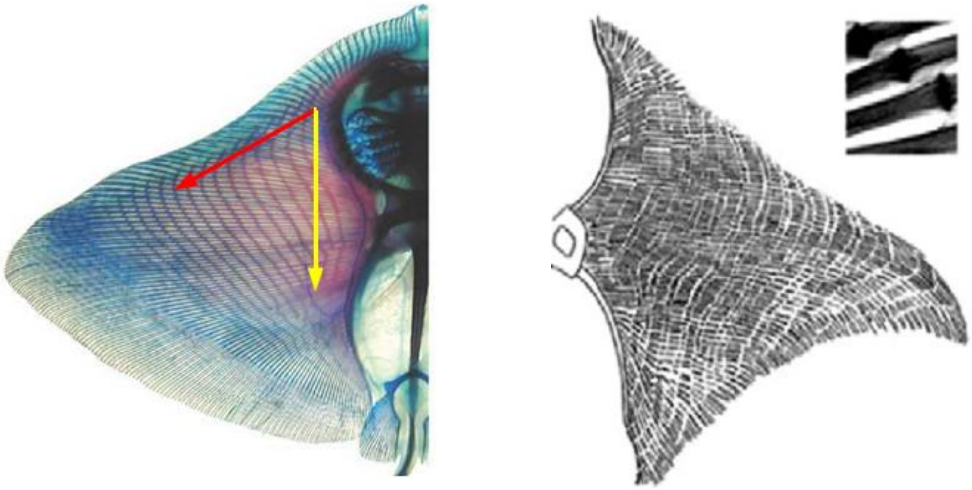

(a) Skeleton of the Gymnura marmorata [18] (b) Skeleton of the Cownose ray [20]

Figure 1.13: Ray fin skeleton

1.1.5 Movement

The manta ray pectoral fin performs a complex motion. It is composed of two waves that travel along the fin in two different directions. In literature this movement is analyzed in different terms, according to the type of robot that one is going to build.

Li et al. [3] considers the principal direction depicted also in Figure 1.10d. Two sinusoidal waves travel and generate a force along these directions (see Figure 1.14). The resultant of the four forces is the thrust that moves the manta.

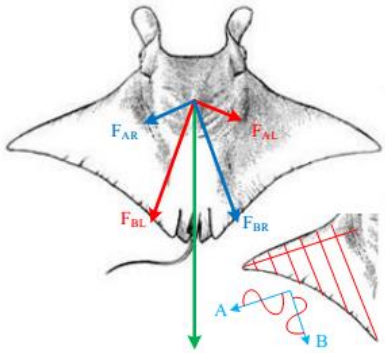

Figure 1.14: Waves across the fin and force generated [3]

Cai et al. [19] considers three points on the fin, shown in Figure 1.15a: the foil tip point (FT), the middle point on the leading edge (MPL) and the middle point on the trail edge (MPT). Each of these points performs a sinusoidal movement. Looking at the envelop of the fin position at different time instants from the frontal point of view (Figure 1.15b) it is possible to define the oscillation amplitude. The different phases of the three sinusoids show that the movement propagates along the body axis of the manta.

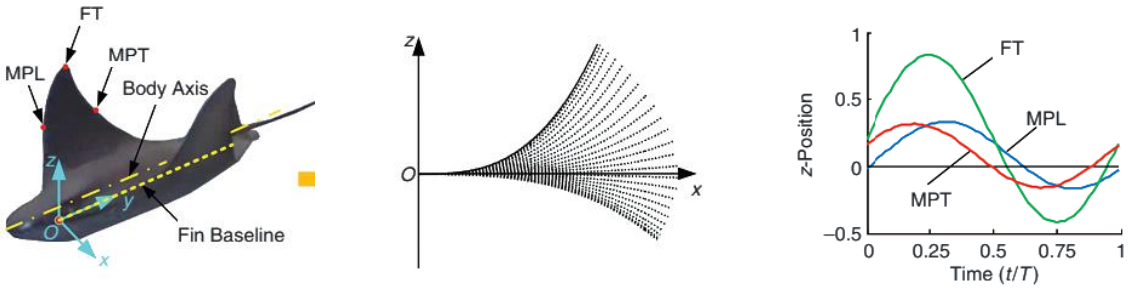

(a) (b) (c)

Figure 1.15: Flapping movement of the pectoral fin sampled in three points [19]

Zhang et al. [21] considers a further simplified movement, considering only one point of the fin and tracking its position and inclination in time (Figure 1.16). This approximation is possible because the chord length is shorter than the wavelength along chord direction (the wave number is around 0.4 [8]). A similar approach is adopted by Cai et al. in reference [18] (Figure 1.17).

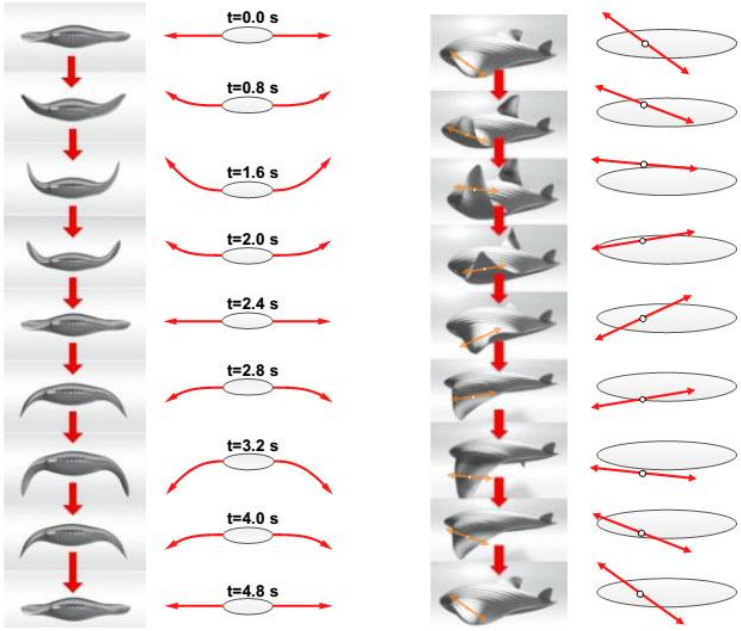

Figure 1.16: Flapping of manta's pectoral fins [21]

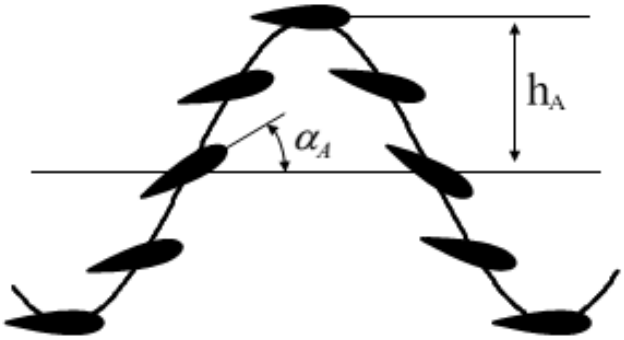

Figure 1.17: Simplified model of foil motion [18]

1.3 Manta ray inspired robots

The problem of mimicking the flapping movement of the manta ray's pectoral fin has been solved in different ways, with different complexity and accuracy. For the scope of this thesis, the solutions available in literature are divided according to the degrees of freedom number of their fins.

1.1.6 14 DOFs

Li et al. [3] proposes a simulated robot that tries to replicate the movement in a quite accurate way. The pectoral fins are divided in seven segments, each of them with two degrees of freedom, which are the rotation around the A and B axis showed in Figure 1.14. Hence, the robot has 14 total DOFs (degrees of freedom) for each fin.

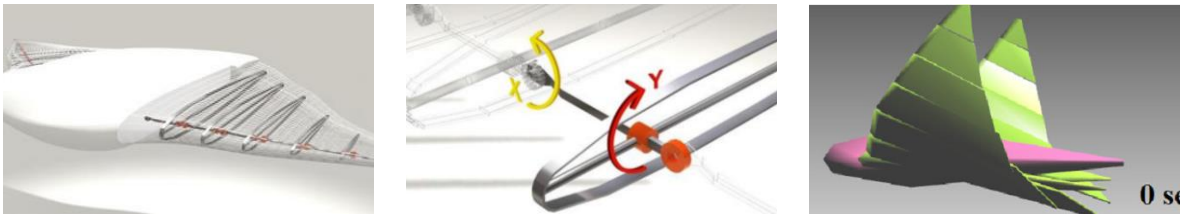

(a) Chassis (b) Mechanism (c) Simulated robot

Figure 1.18: Manta ray by Li et al. [3]

1.1.7 3 DOFs

A solution applied in some robots is to have the fin moved by three independent ribs. Some mechanism allows each rib to perform a desired deformation to replicate the fin curvature, while the phase gap between each rib movement creates the wave along traveling direction.

This solution is applied in 2009 by the team of professor Low, from the Nanyang Technological University in Singapore. The robot was called RoMan-I. This robot was later developed with the models RoMan-II [1], RoMan-III [22] and RoMan-IV [23]. The first model (Figure 1.19a) had the ribs divided in segments, and a serial mechanism allowed bending. The second and third models (Figure 1.19b, Figure 1.19c) used some flexible ribs whose deformation depends on the bending stiffness. The last model instead uses a compliance mechanism called Fin Ray Effect® to precisely control the deformation of each rib (Figure 1.19d).

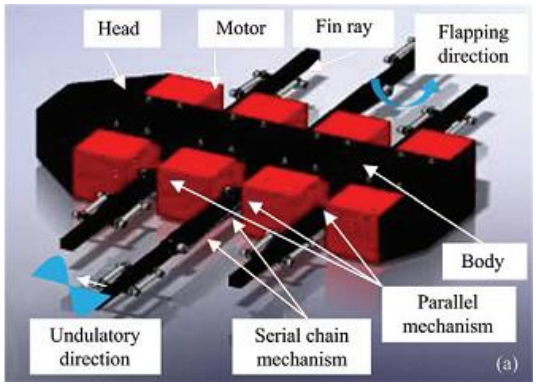

(a) RoMan-I

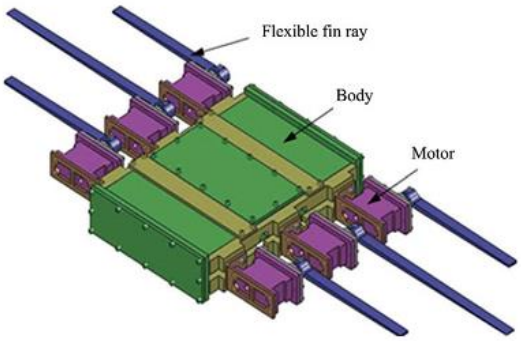

(b) RoMan-II

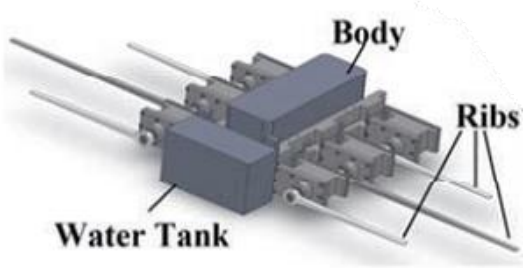

(c) RoMan-III

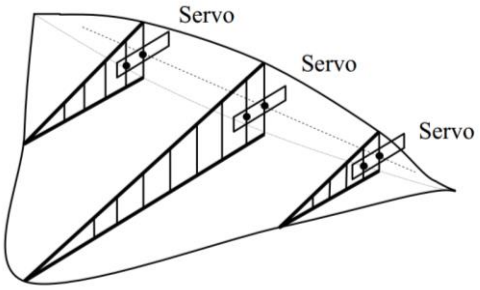

(d) RoMan-IV, fin structure

Figure 1.19: RoMan series

Another prototype with the same working principle has been developed at the Beihang University in Beijing by Cai et al. The first publication in 2012 [9] presents an innovative mechanism to follow the curvature of the cownose ray pectoral fin (Figure 1.20a). In 2018 they presented the improved version of this robot (Figure 1.20b) that maintains the same mechanism.

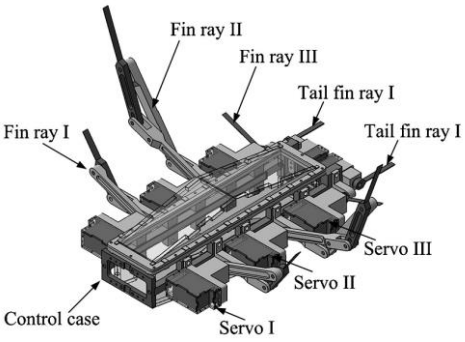

(a) Mechanism in 2012

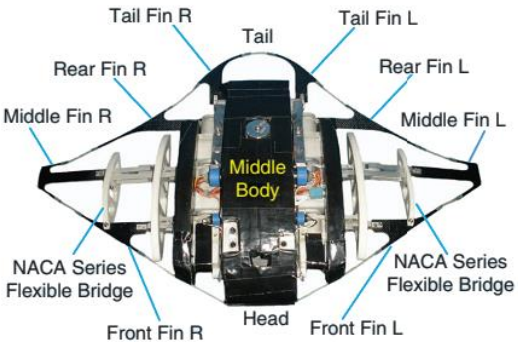

(b) Improved prototype in 2018

Figure 1.20: Manta by Cai et al.

The robot developed in Polimi exploits this principle too, having three independent mechanisms for each fin. The objective of this thesis is to build a smaller and simpler robot than the already existing one, so I kept it as a comparison term.

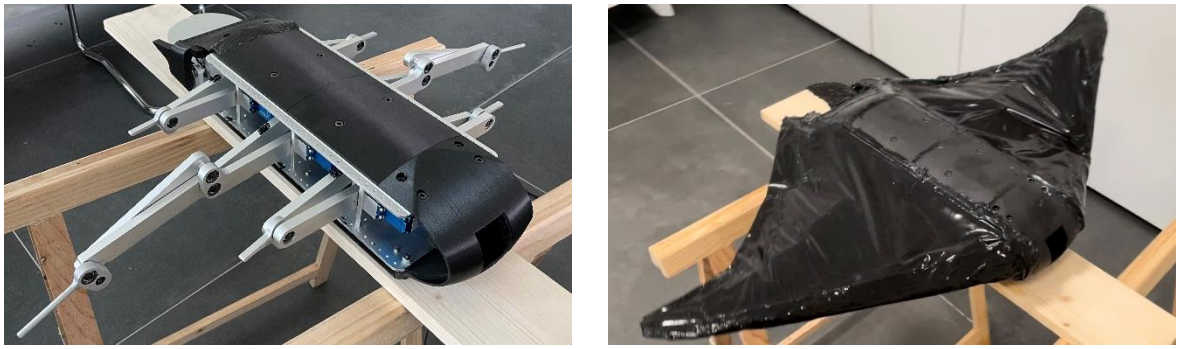

(a) Without cover (b) With cover

Figure 1.21: Manta robot prototype developed at Polimi

1.1.8 2 DOFs

A simpler solution to achieve the movement of the fin is to have only two motors: one of them controls the upside-down flapping movement, while the other one controls the rotation of the fin. These mechanisms aim to replicate the motion shown in Figure 1.17, taking advantage of the small wave number of the manta ray fin, as explained in paragraph 1.2.

The prototype by Ma et al. [24] applies this principle. The torsion of the fin is more effective if the torque is applied on the tip. Due to the lack of space inside the fin, their prototype has a motor mounted on the central body and a flexible shaft transmits the torque to the tip (see Figure 1.22). The flapping movement, instead, is provided by a motor placed on the leading edge base.

(a) Fin scheme (b) Fin photo (c) Manta assembled

Figure 1.22: 2 DOFs fin by Ma et al. [24]

Zhang et al. [21] built a similar prototype with some interesting features. In this prototype the twisting of the fin is provided by a servomotor (denoted in green in

Figure 1.23a) placed at the end of a flexible beam (denoted in red in Figure 1.23a). Some ribs are rigidly connected to this beam and are connected by some cables (denoted in purple in Figure 1.23a). The second servomotor, fixed on the central body, pulls and releases the cables, causing the deformation of the beam by Fin Ray Effect® (visible in Figure 1.23b).

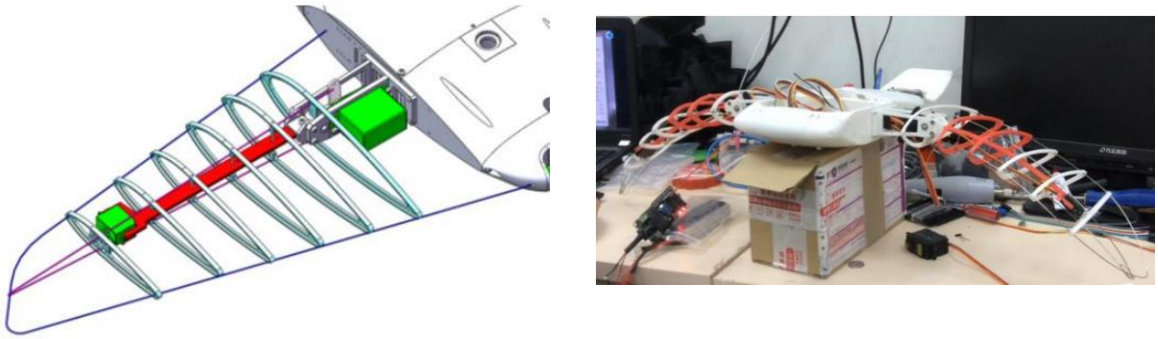

(a) Fin scheme (b) Prototype photography

Figure 1.23: Manta ray with flexible pectoral fin [21]

The same configuration (servo on the tip of the fin and deformation by Fin Ray Effect®) is applied by the German company Festo on their robot Air_ray [25]. The peculiarity of this prototype is that it flies in air using the swimming principle of manta ray. The buoyancy is achieved by filling the robot flexible cover with helium, like a balloon.

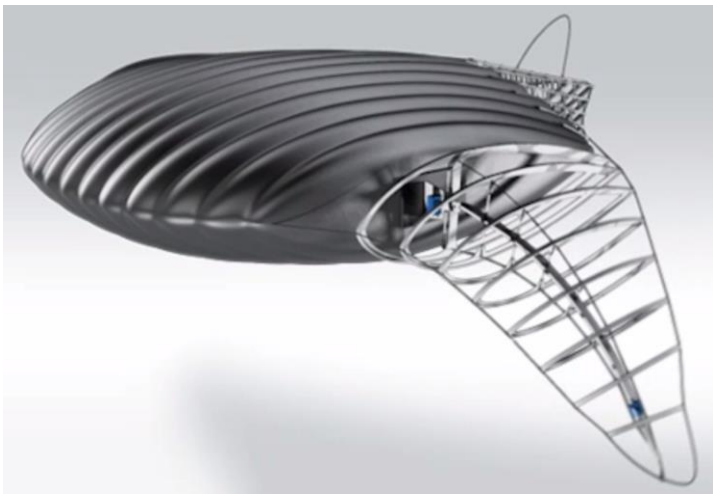

Figure 1.24: Air_ray by Festo. Frame from the video [25]

1.1.9 1 DOF

The simplest possible solution is to control the fin with just one actuator. In this case the fin is made in flexible material, and the deformation is passive.

A prototype that uses this principle has been developed at the Beihang University in Beijing. In the paper [26] a first prototype of their robotic fish is presented (Figure 1.25a). The pectoral fin is composed of a L-shaped structure (Figure 1.25b) made in carbon fiber, filled with a flexible membrane made of silicone rubber. In this first prototype there is a single motor controling both the fins using a transmission mechanism.

This prototype has been subsequently improved [18]. The new fin has a shape more similar to the real manta ray (seen in Figure 1.11b). The leading edge is in fiberboard rather than a carbon fiber beam, and its width reduces along the direction of the fin root (Figure 1.25d) in order to decrease the bending stiffness and obtain a more realistic deformation.

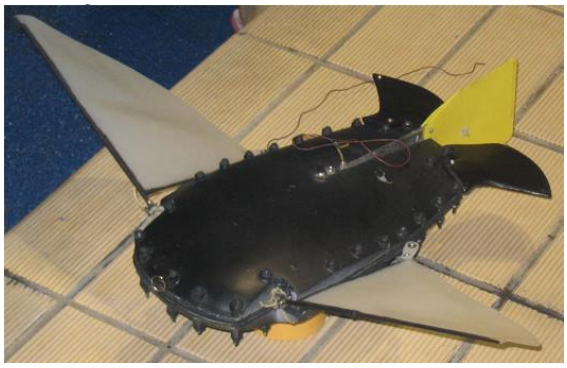

(a) First prototype

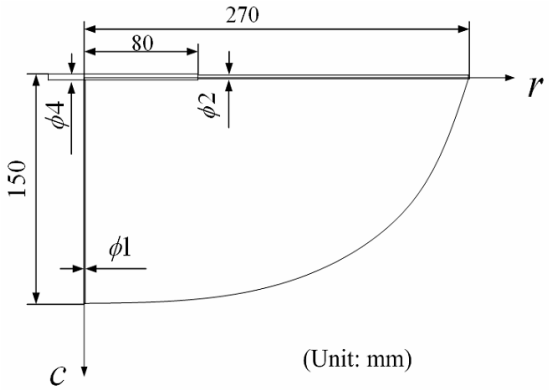

(b) First prototype fin shape

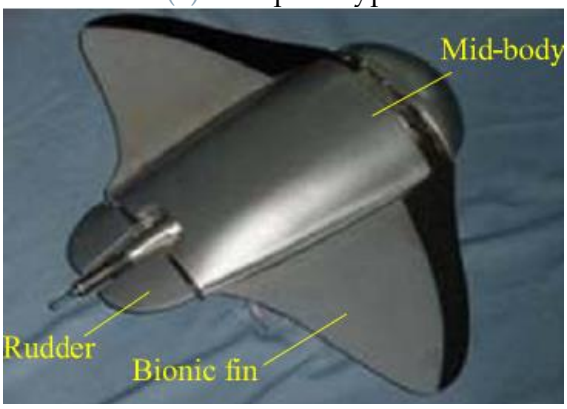

(c) Second prototype

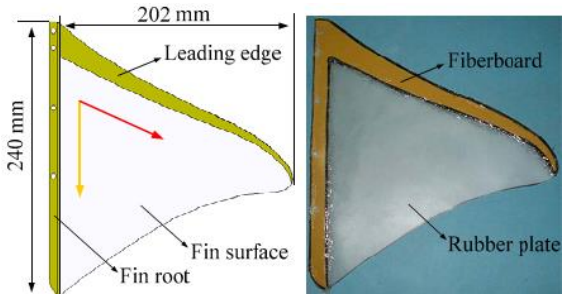

(d) Second prototype fin shape

Figure 1.25: Robots from Beihang university

Another prototype has been developed at National University of Singapore by Chew et al. [8]. Differently from the previously seen model, in this prototype the fin root is not connected to the robot body and it is free to oscillate. The leading edge is obtained by 3D printing using ABS, and it is connected directly to a servo motor (Figure 1.26a). The fin is a PVC film with uniform thickness.

The Singapore team has performed a wide research about deformable fin properties and their ability to generate thrust. The research exploited the fin thickness, the oscillation amplitude and frequency [8], the fin shape and section [27]. The first prototype (Figure 1.26b) was hence improved (Figure 1.26c) up to obtaining a speed equal to twice its body length per second and an autonomy up to 10 hours [28].

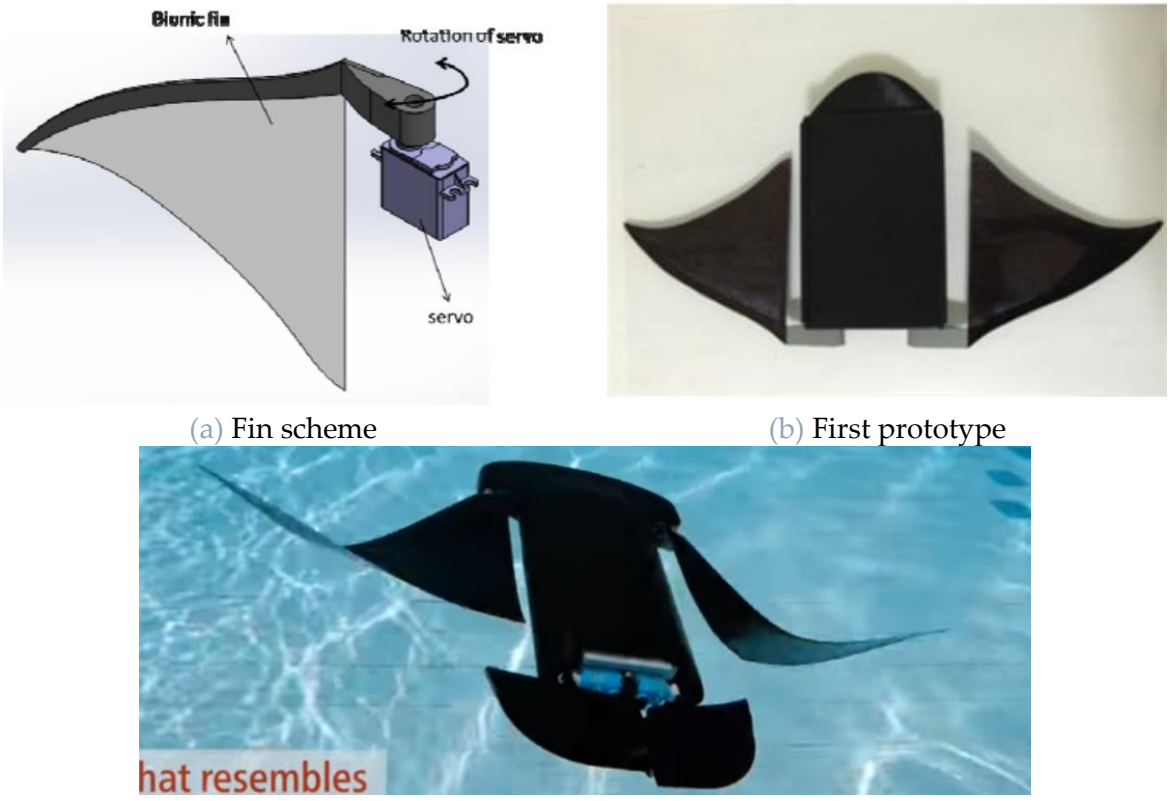

(a) Fin scheme (b) First prototype

(c) Last prototype, frame from the video at [28]

Figure 1.26: MantaDroid from NUS.

1.1.10 Innovative actuators

All the prototypes analyzed so far use electric motors to provide the motion. Some engineers instead have explored different solutions. For the scope of this thesis, these solutions are grouped in a separate class with respect to the DOFs scheme used up to now.

One possible solution, proposed by Chen et al. [29], is to use an electroactive polymer to build the fin. The electroactive polymer is a membrane composed by two metal layers with fixed anions and, between them, a solution with water and cations (Figure 1.27a). When an electric potential is applied to the two metal layers, the cations inside the solutions move toward the negative pole, causing a deflection of the membrane.

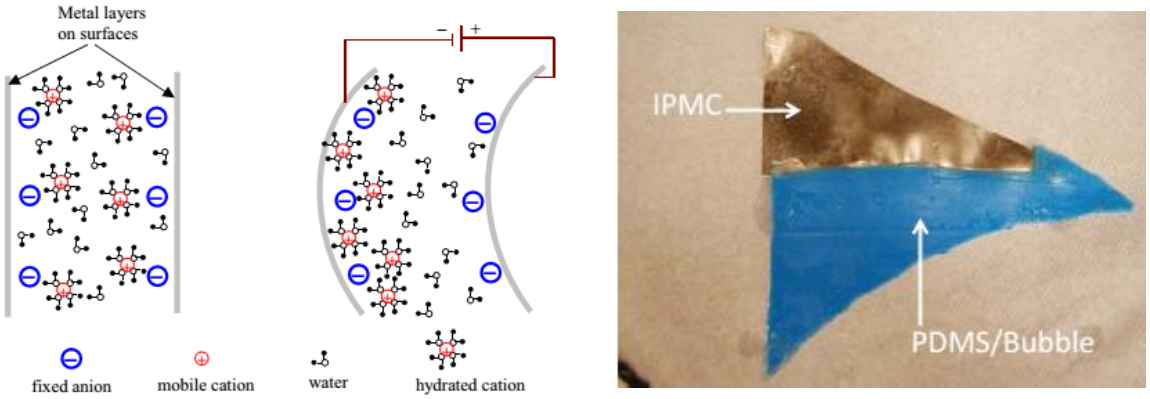

(a) Working principle (b) Fin manufactured

Figure 1.27: Pectoral fin with electroactive polymer [29].

The fin is composed by a layer of electroactive polymer at the leading edge, while the remaining part is a thin membrane in polydimethylsiloxane (PDMS), which oscillates passively and generates the movement of the robot. This solution has only one DOF and can be compared to the MantaDroid from Chew et al. [8] because the base of the fin is free.

Cai et al. [20] proposed a manta moved by pneumatic artificial muscles, called Robo-ray II. The artificial muscles are cylindrical elements that compress and elongate as a function of the inner pressure (Figure 1.28a). The artificial muscles connect the middle skeleton of the robot to a flexible rib, placed on the leading edge of the fin. The compression of the muscle causes the deflection of the rib. The entire robot is covered by a soft body made in silicone rubber, which passively oscillates causing the movement of the robot.

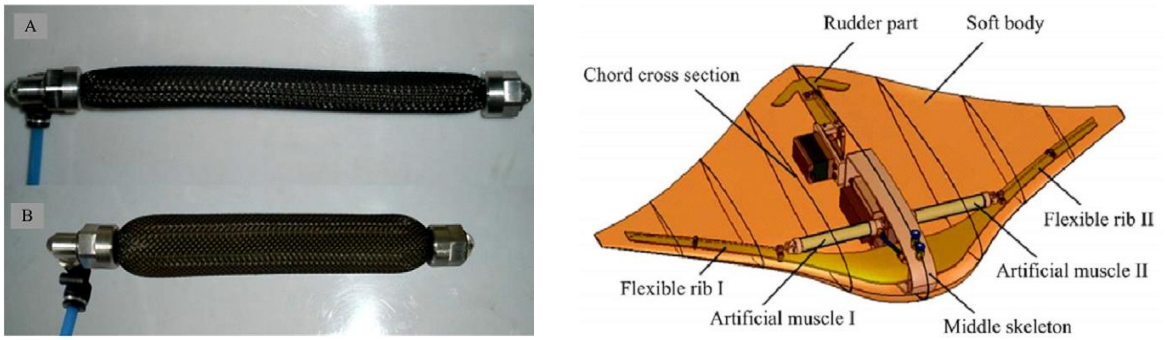

(a) Artificial muscles (b) Drawing of the manta

Figure 1.28: Robo-ray II by Cai et al [20]

This fin has one DOF. The base of the fin is connected to the body, so the solution is similar to the one proposed by Cai itself et al. in the paper [18]. The main difference is that in this Robo-ray II the fin has a three-dimensional shape, while in the other it is just a thin layer.

Franzini et al. propose a completely new design [30]. They built a soft robot where the fins are actuators themselves. The fins are molded in silicone and have some cavities inside, separated between upper and lower part (Figure 1.29). When a pressure is applied in one of the two sides, the channels expands, causing an elongation of the corresponding side of the fin and causing the bending of the fin itself. This pneumatic actuated fin is completely new and it is not comparable to any of the prototypes seen so far.

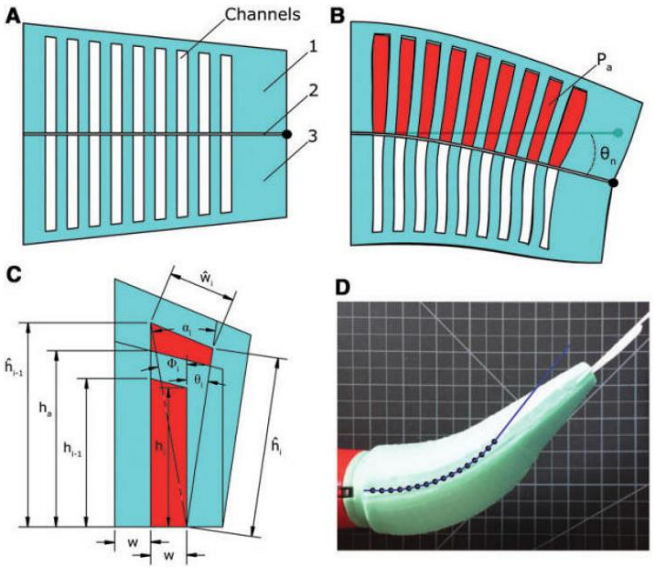

Figure 1.29: Working principle of soft robot by Franzini et al. [30]

Finally, it is worth to mention the prototype Aqua_ray from the Germany company Festo [31]. These fins take advantage of the Fin Ray Effect®, as already seen previously with Air_ray [25]. The main differences, apart from the fluid they swim in, is that Aqua_ray moves the fin using bionic fluidic muscles (Figure 1.30a) and provides only the flapping movement, while the rotation movement is passive.

(a) X-ray image with the pneumatic circuit (b) Fins flapping without cover

Figure 1.30: Festo Aqua_ray.

2. Mechanical design

The design process of this prototype starts with the choice of the working principle. The following step is the choice of the electronic components and, finally, it comes the detailed mechanical design based on the dimensions of the chosen components.

In this chapter the mechanical design will be analyzed in detail taking for granted the dimensions of the electronic components. The choice of these components will be described in chapter 3.

All the mechanical design has been performed on the CAD software Solidworks.

2.1 Working principle

One of the first requirements of the prototype is to have a simpler working principle with respect to the 3-DOFs robot already developed at Polimi. Considering the classification adopted in the state of the art, the robot fin should have one or two DOFs.

The latter solution was considered in the preliminary designs, in particular the possibility of employ the Fin Ray Effect®. This solution would generate an accurate movement of the fins. On the other hand, it would limit the design of the fins to only one shape.

For this reason, it has been considered more interesting to develop a robot whose fin has only one DOF. The design of the robot is independent from the design of the fins. Each pectoral fin is moved by one servomotor placed in the front part of the robot (Figure 2.1). The motor shaft is accessible, so that it is easy to change the fin. This design allows to use the robot as a testbench for experimenting the efficiency of different fins in a future research.

The main body has also two caudal fins in the rear part. Their role is to control the pitch of the robot and guarantee stability during the flapping of the pectoral fins. Two more servomotors are needed to control their position.

The robot buoyancy is determined a priori by adding or removing ballasts, and the robot vertical motion is controlled by the caudal fins.

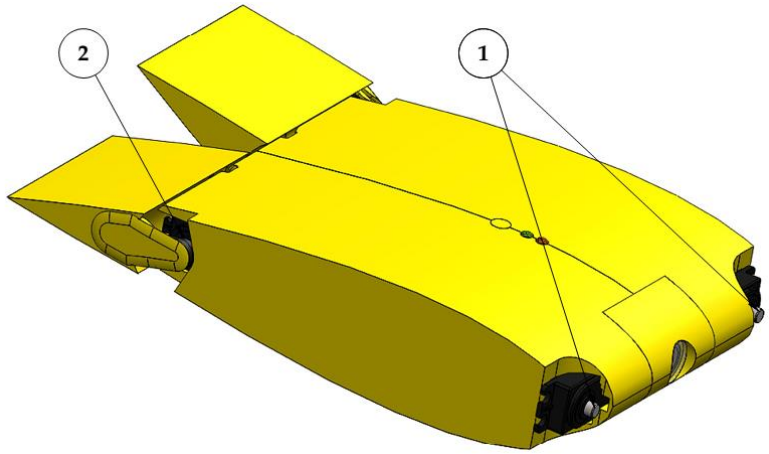

1	Front motors
2	Rear motors

Figure 2.1: Motors position in the robot

2.2 The core

The core of the robot is where all the electronic components are stored. It must be completely waterproof. It is composed by a central waterproof box, with attached two 3D-printed extensions. In the rear part are placed the power switch and a connector that allows to charge the battery and communicate with the microcontroller via USB. On the side of the box there are four waterproof cable glands for the motor cables.

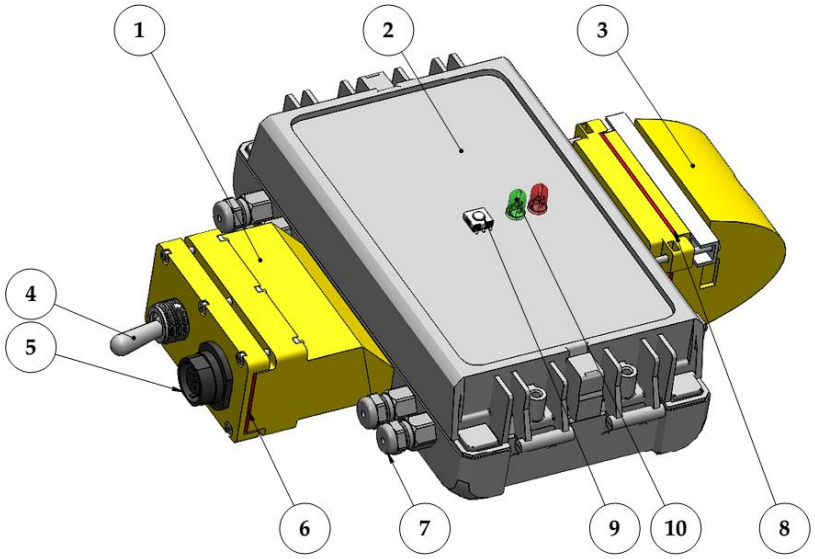

1	Rear extension
2	Central box
3	Front extension
4	Power switch
5	Connector
6	Rear gasket
7	IP68 Cable gland
8	Front Gasket
9	Button
10	LEDs

Figure 2.2: The robot core

The front extension contains the camera and it is the only part of the core visible when the robot is assembled. Finally, on the top of the box, there are a button and two LEDs to monitor the robot state.

2.2.1 Central box

The central box is a waterproof box made of ABS plastic. Its dimensions have been selected to contain the Arduino DUE as fit as possible (Figure 2.3a). Inside of it there are the batteries, the Arduino DUE and the electronic components, stacked in three layers with a plastic structure (Figure 2.3b).

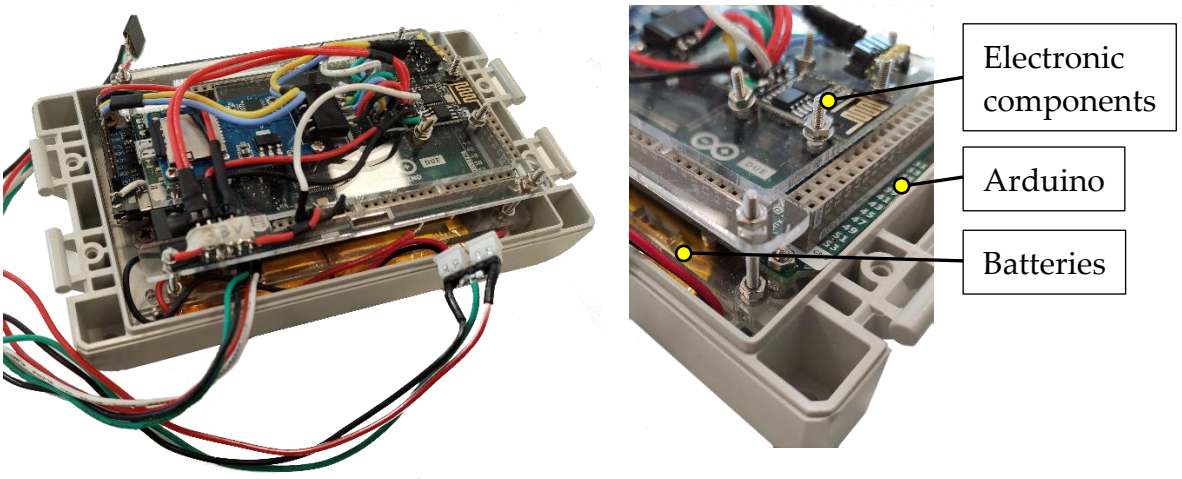

(a) Central box and content (b) Detail of stacking

Figure 2.3: Central box

The box cover is tightened by four screws, instead of using the supplied flaps. Two holes are performed in the central part of the two long sides, to let the cables pass through from the extensions to the microcontroller. Other four circular holes are performed to accommodate the cable glands.

2.2.2 Rear extension

The rear extension has the function of containing the power switch and the connector. The dimensions of the switch are remarkable because it is waterproof. The connector is quite big as well because seven pins are needed: four of these pins are connected to the USB cable to program the microcontroller while the other three are dedicated to the battery charging.

The necessity of fitting these two components defines the dimensions of the rectangular section of the extension. A small sloped part, glued to the central box, creates the offset needed to align the rear extension with the robot horizontal plane of symmetry.

The two electric components are fixed on the lid of the rear part. Six M2 bolts distribute pressure along the rectangular gasket in order to hermetically close the lid. The gasket is realized in flexible PVC.

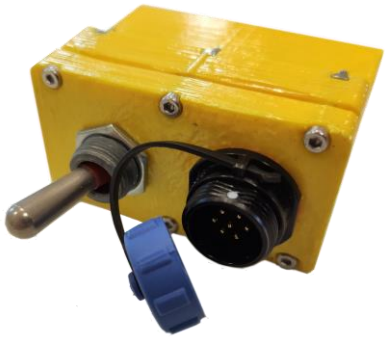

(a) Rear view

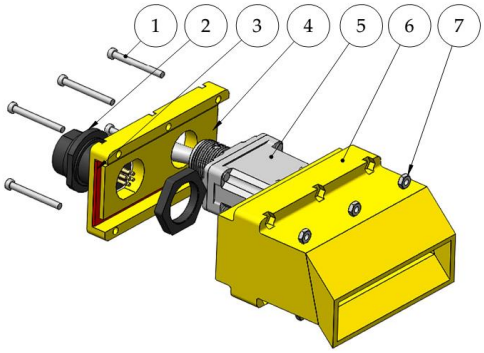

1	M2 screws
2	Connector
3	Gasket
4	Lid
5	Switch
6	Extension
7	M2 nuts

(b) Exploded view of rear assembly

Figure 2.4: The rear extension

2.2.3 Front extension

The front extension contains the camera. The front head internally has a cavity shaped in order to have the camera objective as forward as possible. For the same reason the electronic board of the camera has been trimmed in order to reduce its height.

Externally the front head is shaped as the NACA 0020 profile used for the cover (details in paragraph 2.4.1). In the front part the porthole is closed by a plastic disk hermetically joined to the head.

The base is glued to the central box in the inferior part. The ledge in the inner part creates the housing for the gasket, the interlocking with the head and, when the head is closed, constrains the camera in its position.

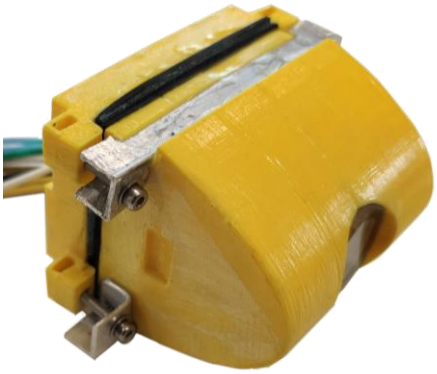

(a) Front view

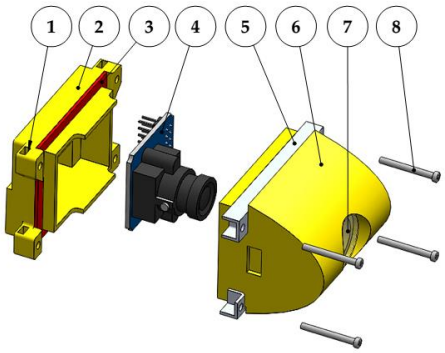

1	M2 nuts
2	Base
3	Gasket
4	Camera
5	Reinforce
6	Front head
7	Porthole
8	M2 screws

(b) Exploded view of the front assembly

Figure 2.5: The front extension

Regarding the hermetic closure of the head, the four bolts used must stay on the sides of the head in order to fit the external NACA profile. At the same time, they have to stay at the top and bottom extremities in order to allow the disassembly of the head without interfering with the motors. This position does not guarantee a uniform distribution of pressure along the gasket. In order to correctly close the gap, it is necessary to strictly tighten the bolts. For this reason, two aluminum reinforces are installed on the head part. Moreover, a gasket made in silicone rubber[8] is added to the PVC gasket already installed. The silicone has higher deformability and requires less tightening of the bolts to obtain the waterproof closure.

2.3 The chassis

The chassis is formed by a 2mm thick aluminum sheet, appropriately cut and bent. A series of threaded holes allows the mounting of the other components on it (Figure 2.6b). The central box is fixed to the central part of the chassis with four screws. The two flaps, centered with respect to the symmetry axis of the chassis, offer support to the front and rear extensions of the core. They are useful to preserve the gluing of the extensions and prevent water leakage inside of the core.

Four other flaps, two in the front and two in the back, are designed to mount the motors. They create the necessary offset to align the motors to the robot horizontal plane of symmetry. Each motor lies on the flat part and is fixed to the additional thin flap with two screws. Two screws are sufficient because the cover contributes as well to their constraining.

In the rear part there are two more vertical flaps with a hole. Here are mounted the bearings of the caudal fins. The flap position is designed in order to leave a channel for the motors cables to reach the central box.

In the central part of the chassis there are also some holes for fixing the cover, some extra holes for mounting some ballast if necessary and some great cavities to reduce the weight of the chassis. The holes can also be used to fix the robot to a testbench during the testing phase in the laboratory.

[8] It is the same material used for the fins (details in paragraph 4.2.2).

(a) Photo of the chassis

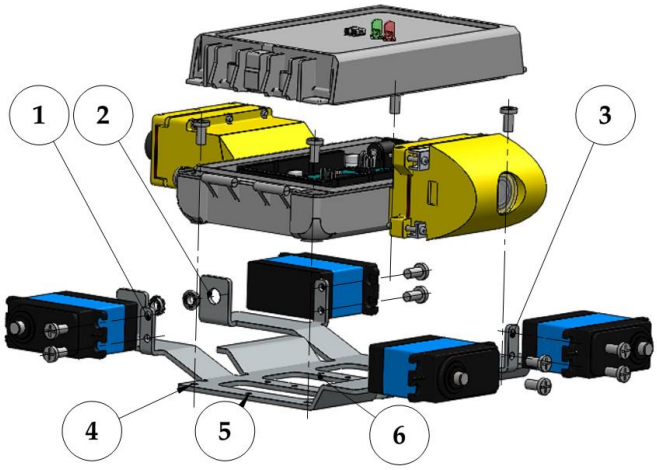

1	Rear motor mounting holes
2	Caudal fin bearings holes
3	Front motor mounting holes
4	Central box mounting holes
5	Cover mounting holes
6	Extra holes for ballast

(b) Assembly of components on the chassis

Figure 2.6: The chassis

2.4 The external part

The external part of the robot influences both the appearance of the robot and its interaction with the fluid. The latter is the most important, and it is the starting point of the cover designing process.

2.4.1 Profile

The literature, as already analyzed in paragraph 1.1.4, shows that the manta body can be well approximated by an airfoil profile. Following the profile analysis by Cai et al. [19], a NACA0020 profile has been adopted for the robot central body. This profile remains constant for all the robot width.

The NACA00xx code identifies symmetric foil profiles, where xx is the percentage of thickness to chord. The equation of a generic NACA 00xx foil[9] is:

$$y_t = 5t\left[0.2969\sqrt{x} - 0.1260x - 0.3516x^2 + 0.2843x^3 - 0.1015x^4\right] \qquad (2.1)$$

Where:

- x is the position along the chord from 0 to 1.00 (0 to 100%)
- y_t is the half thickness at a given value of x (centerline to surface)
- t is the maximum thickness as a fraction of the chord, so t gives the last two digits in the NACA 4-digit denomination divided by 100).

The airfoil adopted in the robot has a chord length $CL = 260mm$. The resulting thickness $t = 0.2 \cdot 260mm = 52mm$ is the smallest possible in order to contain all the components inside the cover. The profile is designed in the CAD software adapting the (2.1) for xx=20 and chord length $CL = 260mm$.

$$y_t = 260 \cdot 5 \cdot 0.2 \cdot \left[0.2969\sqrt{\frac{x}{260}} - 0.1260\frac{x}{260} - 0.3516\left(\frac{x}{260}\right)^2 + 0.2843\left(\frac{x}{260}\right)^3 - 0.1015\left(\frac{x}{260}\right)^4\right]$$

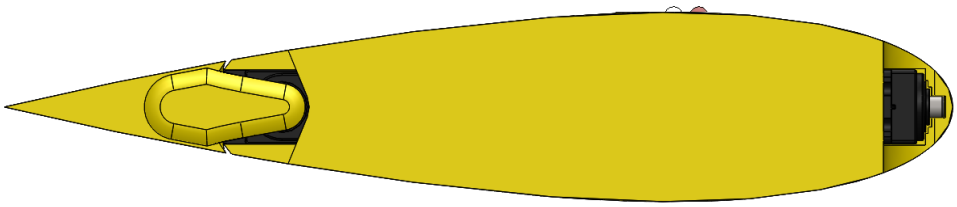

Figure 2.7: NACA0020 profile of the cover

[9] From https://en.wikipedia.org/wiki/NACA_airfoil, last visited on 05/11/2021.

The airfoil profile is divided in two parts: the cover, fixed to the central box, and the caudal fins, that can move.

2.4.2 Cover

The rigid structure that forms the cover is divided in two halves by a vertical plane. The two symmetric shells can be removed by sliding them sideways. Five coupling plugs with a trapezoidal profile guarantee the alignment of the two sides and join them by friction. The shells are connected to the central box by a compliance mechanism, taking advantage of the original flap interlocking (Figure 2.9). Finally, one M3 screw connects each shell to the chassis.

On the top part of the shells three half holes surround the LEDs and button on the top of the central box. A small lever covers the button and helps the pushing.

On the inferior part a great rectangular hole allows the access to the threaded holes in the chassis. When it is not necessary to use them, they are covered by a lid.

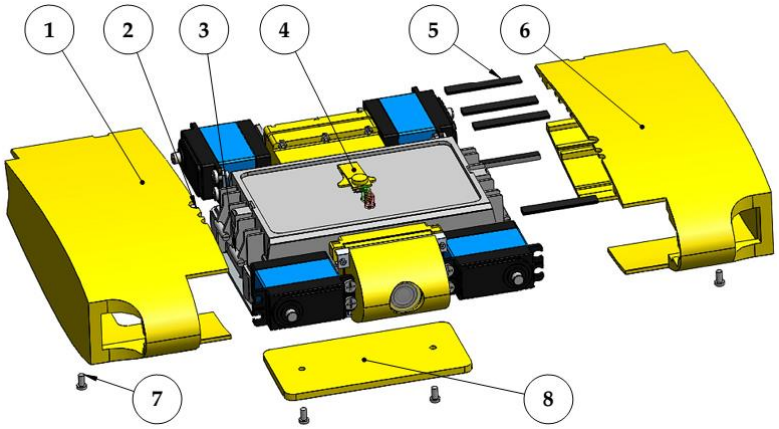

1	Left shell
2	Holes on the top
3	Joint with central box
4	Button
5	Coupling plug
6	Right shell
7	M3 screws
8	Inferior lid

Figure 2.8: Cover assembly

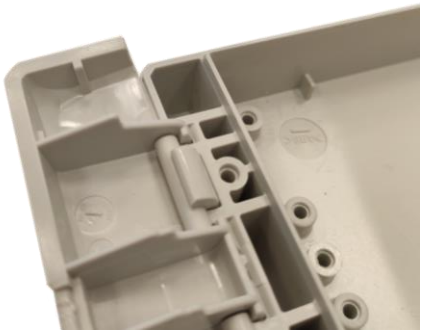

(a) Original flap, detail

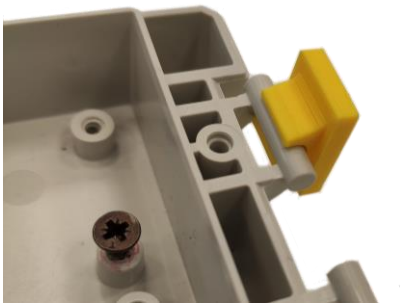

(b) Interlocking with the cover, sampling

Figure 2.9: Box-cover interlocking

On the inner side of the shells there are a series of extrusions and slots in order to surround the elements with a small tolerance. This helps the shells alignment and the motors constraining.

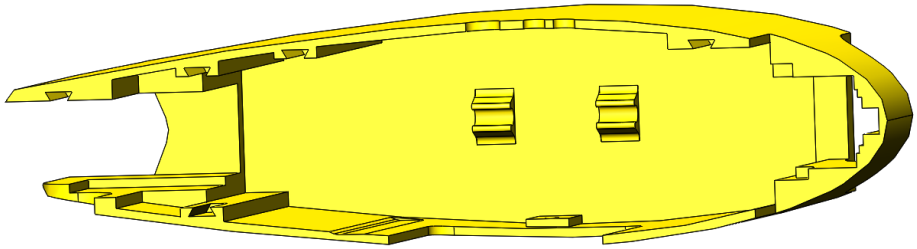

Figure 2.10: Internal view of the shell

2.4.3 Caudal fins

The caudal fins sections follow the end of the NACA 0020 profile. Each fin is connected to the original bracket of the motor with two screws. On the other side the fin is supported by a flanged bearing connected to the chassis. The bearing flange and the screws fully constrain the fin except for the allowed rotation.

A small lid fits in the fin and covers the bracket and the screws. It has a purely aesthetical function.

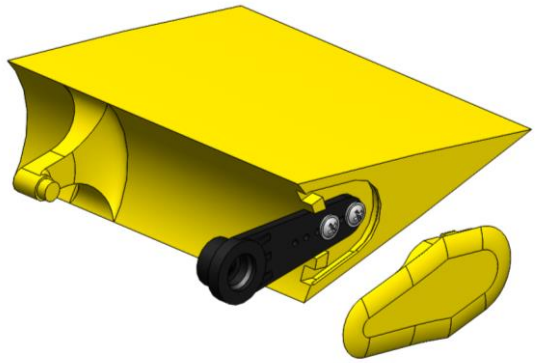

(a) Caudal fin with the small lid

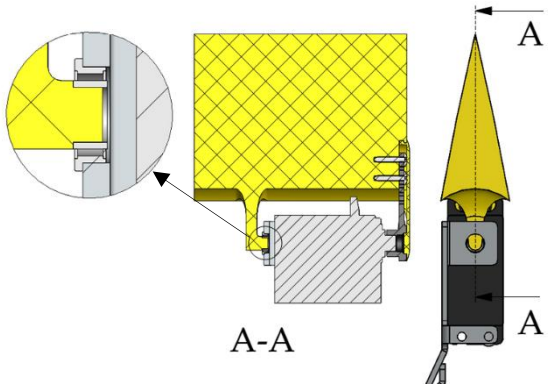

(b) Section of the caudal fin mounting, with the detail of the flanged bearing

Figure 2.11: Caudal fin

The caudal fins can rotate up to 20° upward and 75° downward. The upward movement is limited by the interference between the fin and the shell. If during the testing the angle appears to be too low, it is possible to increase the dimension of the slot in the rear part of the shell (Figure 2.12b).

The downward movement instead is limited by the interference between the motor bracket and the shell. The caudal fins have such a great freedom in downward movement in order to allow an easy access to the connector placed in the rear part of the manta for programming and battery charging.

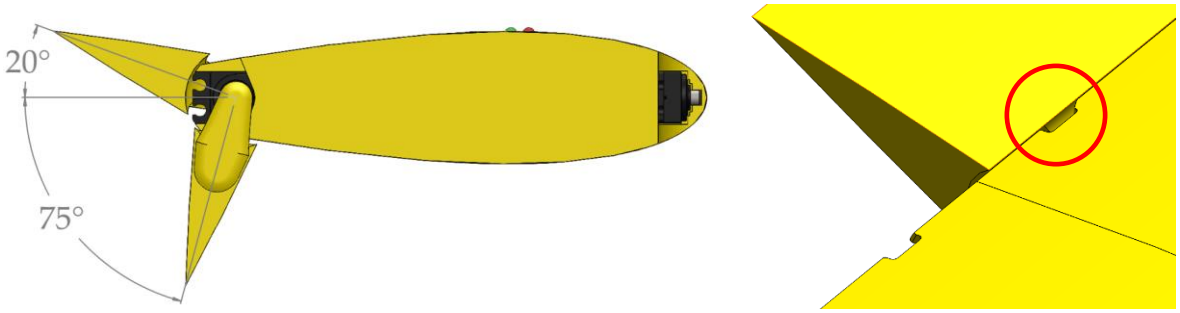

(a) Limit angles of caudal fins (b) Fin-shell interference, detail

Figure 2.12: Caudal fin movement

3. Electronic components

3.1 Microcontroller

Among all the possible microcontrollers available on the market, we decided to use Arduino, because it is low cost, easy to program and there are many compatible accessories.

There are various models of Arduino that differ in available pins number and computational power. Taking into account both aspects, Arduino Due has been chosen (Figure 3.1). It has 54 digital input/output pins, 12 analog inputs and 4 UARTs [32], which is comparable to the Arduino Mega 2560. The main difference with other Arduino boards, is the processor. It is the first Arduino board based on a 32-bit ARM core microcontroller, the Atmel SAM3X8E ARM Cortex-M3 CPU. It has an 84 MHz clock and 512 KB flash memory available for user applications. These characteristics guarantee higher computational power with respect to the Arduino Mega (or other Arduino boards), useful for programming the robot control.

The Arduino Due has a Micro-AB 2.0 USB port, called Native port, and a Micro-B 2.0 USB, called programming port, both available for programming despite of the name. Anyway, the SAM3X processor needs a complete erase of the previous program before uploading the new one. The programming port is able to perform a “hard erase” procedure, which is more reliable than the “soft erase” available on the Native port.

Figure 3.1: Arduino Due top view [32].

This last aspect introduces one of the disadvantages of this board. Due to this erasing procedure, the Arduino Due cannot be programmed through the UART pins RX0 and TX0. For this reason, it is necessary to think about some software strategies to be able to communicate with Arduino and change its behavior without plugging in the USB every time.

The dimensions (101.52mm length, 53.3mm width) are the second disadvantage of this board. The philosophy of this robot is to have a small and easy-to-test prototype, and the length of the Arduino Due sets the lower limit of the manta robot width.

3.2 Motors

3.2.1 Preliminary dimensioning

The robot is equipped with four electric servomotors. Two for the pectoral fins and two for the caudal fins.

To properly choose the motors, an approximate computation of the need torque has been performed. Based on the paper [8], some assumptions about dimensions, material and motion law of a flexible fin were made.

From the fin shape used by NUS engineers (Figure 3.2.a), the fin shape is approximated to an isosceles triangle with $b = 200mm$ base and $w = 195mm$ width (Figure 3.2.b).

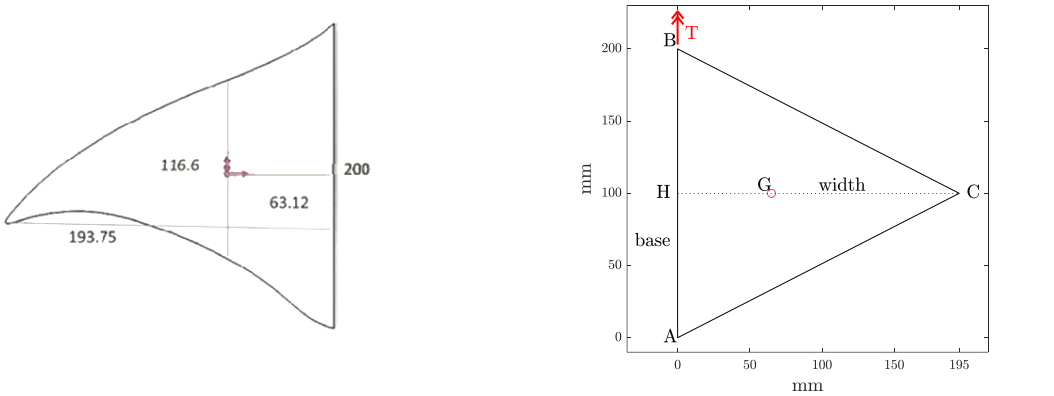

(a) Fin from reference [8] (b) Schematic fin used for dimensioning

Figure 3.2: Fin used for dimensioning of motors.

In paper [8] fins are made in PVC film of uniform thickness equal to $0.76mm$. In this project the fin thickness is, instead, $5mm$. Considering the density of flexible PVC[10] $\rho = 1.35\,{}^{g}/_{cm^3}$, the resulting mass of the fin is $0.131625\ kg$.

The second moment of inertia of a homogenous right triangle rotating around the cathetus of length b is:

$$J_b = \frac{m \cdot a^2}{6} \tag{3.1}$$

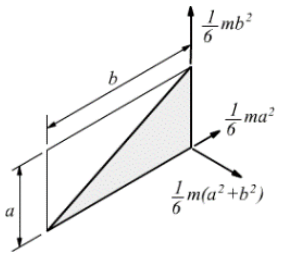

Figure 3.3: Second moments of inertia of a homogeneous right triangle

Applying the equation (3.1) to the two right triangles ACH and BCH rotating around the fin base AB, the resulting total moment of inertia is:

$$J = \frac{m \cdot w^2}{6} = 834.1734\ kg \cdot mm^2$$

Regarding the movement, a sinusoidal motion law is considered (Figure 3.4). According to the most stressful experiment from NUT [8], the angular position oscillates with amplitude $A = 80°$ at frequency $f = 1Hz$. The maximum angular acceleration is given by

$$\dot{\omega}_{max} = A \cdot (2\pi \cdot f)^2 = 3158.27\,\frac{deg}{s^2} = 55.12\,\frac{rad}{s^2} \tag{3.2}$$

[10] Data taken from web page https://en.wikipedia.org/wiki/Polyvinyl_chloride, last visited on 24/10/2021.

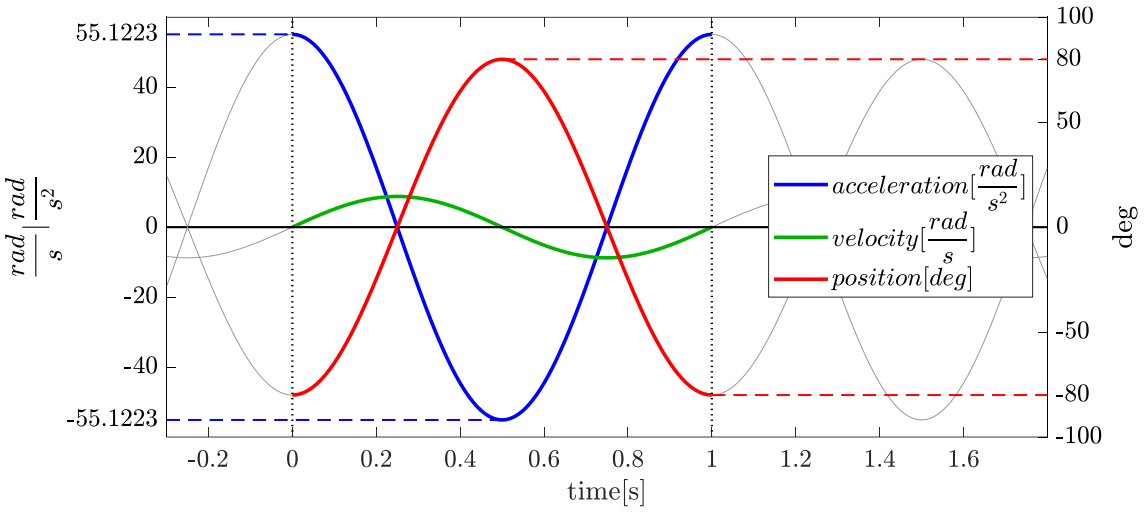

Figure 3.4: Motion law applied to the fin for the dimensioning of the motors.

Finally, the needed torque is computed as:

$$T_{max} = J \cdot \dot{\omega}_{max} = 0.045982N \cdot m = 0.468721 \text{ kg} \cdot \text{cm} \tag{3.3}$$

The applied procedure has some strong limitations, because it neglects the flexibility of the fin and the added mass due to the presence of the water. While the first limitation is acceptable, the second one is a very strong assumption. On the other hand, it is really complex to compute the added mass, and it is not reasonable at this stage of the design process. Hence, it is necessary to consider a great safety factor in order to choose a motor able to fulfill the required task.

3.2.2 Choice of motors

Apart from the torque, another important requirement is the resistance to water. The choice fell on one of the smallest waterproof servomotors available on the market, the TD-8320MG (Figure 3.5). Its technical characteristics[11] are listed in the following table.

The available torque is quite high with respect to the one previously computed. This fact should guarantee a sufficient safety factor for the correct functioning. Moreover,

[11] Characteristics available on the online stores: https://www.plexishop.it/it/servocomando-td8320mg-180-20kg.html; https://www.robotstore.it/Servo-digitale-standard-TD8320MG-20KG-Waterproof; last visited on 25/10/2021.

the MantaDroid from NUS mounts the HITEC HS646WP servomotors [8], which provide a lower torque[12] (11.6 $kg \cdot cm$).

TD-8320MG technical data			
Rotation speed	**at 4.8V**	$0.18 sec/60°$	$5.82\,{}^{rad}/_{s}$
	at 6.0V	$0.14\ sec/60°$	$7.48\,{}^{rad}/_{s}$
Torque without load	**at 4.8V**	$17.2\ kg \cdot cm$	$1.69\ N \cdot m$
	at 6.0V	$20.5\ kg \cdot cm$	$2.01\ N \cdot m$
Working voltage		$4.8 \sim 7.2\ V\ DC$	
Working frequency		$1520\mu s\ /\ 333Hz$	
Working temperature		$-20℃ \sim 60℃$	

Table 3-1: Technical data of TD-8320MG servomotor

Regarding the control of the motor, the TD-8320MG is a digital servomotor. It receives as input the position to reach. The internal microcontroller of the servomotor controls the rotation in order to reach that position but does not give any feedback. It is not possible to control the rotation speed. These characteristics limit the motion controllability, but on the other hand allow to concentrate on the manta trajectories and maneuvering with a simple feedforward approach.

Figure 3.5: The TD-8320MG servomotor

[12] Characteristic available on the online store; https://hely-go.net/servi-standard/8978-hitec-hs646wp-waterproof-ip67.html; last visited on 25/10/2021.

3.3 Batteries

The Arduino Due requires a recommended input voltage $V_{in} = 7{\sim}12V$. The servo motors have a working voltage $V_{servo} = 4.8 \sim 7.2\,V$. The battery should supply power to both of them, so it has to provide around $7 \sim 7.2\,V$. It also could be possible to connect the motors to the 5V output of the Arduino, but this would limit the available torque, so this possibility has been discarded.

3.3.1 LiPo batteries

The required power can be well supplied by a lithium polymer battery (LiPo) with two-cells. These batteries are largely used for small applications that require high specific energy[13], for example in mobile devices, car modelling, drones. The voltage of a single LiPo cell can vary between $4.2V$ when fully charged and $2.7–3.0\,V$ when fully discharged[14]. The nominal tension of each cell is $3.7V$, so a two-cell LiPo battery provides $7.4V$ and fulfills the requirement.

Apart from the voltage, the batteries are characterized by their capacity and their maximum discharge current. The capacity is expressed in milliampere-hours $[mAh]$. The max current, depending on the application of the battery itself, can be expressed in Ampere $[A]$ or C. The parameter C, multiplied by the capacity, indicates the max current.

Figure 3.6: A 2 cell LiPo battery for model applications

[13] Specific energy=energy per unit of mass [J/kg].
[14] From website https://en.wikipedia.org/wiki/Lithium_polymer_battery, last visited on 25/10/2021.

For example, the battery[15] from FullPower shown in Figure 3.6, is characterized by 2s (two cells, $7.4V$), $1800mAh$ capacity and 35C discharge capacity ($1800mAh \cdot 35C = 63A$). This is a typical battery applied in models (like cars or drones), where a great current is needed by the motors to generate the torque.

3.3.2 Choice of batteries

LiPo batteries for model application usually have two long cells stacked inside a rigid cover and very thick cables to avoid overheating while discharging at high current rate. The dimensions of the battery in Figure 3.6, for example, are $35 \times 105 \times 14.5\ mm$. This form factor is not optimal for the manta prototype.

For this reason, the battery MIKROE-1120 has been chosen (Figure 3.7a). This is a single-cell 2000mAh battery. The form factor is similar to the one of the batteries inside the mobile devices, and the dimensions are only $6mm \times 44mm \times 63mm$. Two of these batteries have been supplied and placed side by side and have been connected in series to obtain two-cell battery with dimensions $6mm \times 88mm \times 63mm$ (Figure 3.7b). The green cable, connected between the two batteries, is necessary to control the balancing between the cells during the charging[16].

In Table 3-2 are reported the most interesting information from the complete datasheet[17]

(a) Image from online shop (b) The two batteries of the manta connected in series

Figure 3.7: Battery MIKROE-1120

[15] Available on the online shop https://shop.jonathan.it/it/447914-fullpower-batteria-rx-lipo-2s-1800mah-35c-v2-jr, last visited on 26/10/2021.

[16] In general, all multiple cells LiPo batteries must be charged with a specific charger that controls the balancing of the different cells in order to prevent damages to the batteries.

[17] https://www.farnell.com/datasheets/2369105.pdf, last visited on 02/11/2021.

MIKROE-1120 technical data	
Rated voltage	3.7V
Rated capacity	2000mAh
Limited charge voltage	4.2V
Standard charge current	400mA (0.2 C)
Max Charge Current	2000mA (1 C)
Max discharge current	Continuous： 2000mA (1 C)
Over-charging Protection Voltage	4.325V±0.1V
Over-discharge Protection Voltage	2.5V±0.1V
Over-current Protection	2-5A

Table 3-2: Technical data of MIKROE-1120 battery

The main difference between these batteries and the batteries designed for modelling, like the one seen previously, is the max discharge current, which is limited to 1C. To ensure that these batteries are suitable for the application, a small experiment has been performed in order to measure the current needed by the electric motors.

3.3.3 Current measure

The experiment is based on the hypothesis that the motor works like a simple DC motor, where the torque is proportional to the current. The following equations can be applied:

$$M \cdot \left(\frac{d}{2}\right)^2 \cdot \dot{\omega} + D \cdot \omega = T_m - M \cdot g \cdot \frac{d}{2} \tag{3.4}$$

$$T_m = k_\phi \cdot i \tag{3.5}$$

A simple test bench was built (Figure 3.8). The motor is rigidly connected to a pulley with diameter $d = 39mm$. An inextensible cable connects a mass M to the motor through another pulley. The pulley and the motor are supposed to have negligible moment of inertia. The total inertia coincides with the external mass attached to the

cable times the squared radius of the pulley. The total damping coefficient D is unknown and must be derived experimentally.

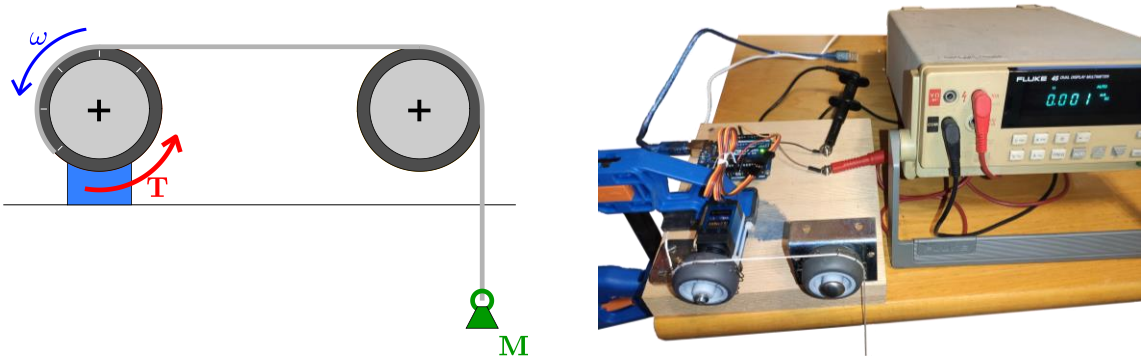

(a) Scheme (b) Bench setup

Figure 3.8: Test bench for current measurement.

The first measure is performed at null rotation speed ($\omega = 0, \dot{\omega} = 0$). The equation (3.4) becomes a simple equality between the torque and the gravity force acting on the external mass. Substituting the (3.5), the constant k_ϕ can be expressed as a function of the measure current i.

$$k_\phi = \frac{M \cdot g \cdot \frac{d}{2}}{i} \tag{3.6}$$

The following measures are performed at constant rotation speed ($\omega = const, \dot{\omega} = 0$). The constant k_ϕ is replaced by the mean value of static measures $\overline{k_\phi} = E(k_\phi)$. The damping coefficient D is:

$$D = \frac{\overline{k_\phi} \cdot i - M \cdot g \cdot \frac{d}{2}}{\omega} \tag{3.7}$$

Finally, knowing the parameters $\overline{D}$ and $\overline{k_\phi}$, it is possible to compute the needed current for a certain load and motion law.

This procedure was applied: for each load and velocity, twenty measures of current are taken[18]. The mean values of the current are shown in Table 3-3.

[18] Measurements are reported in detail in *Appendix A – Current measures.*

Mean current measured $[A]$							
$\mathbf{M}[Kg]$ / **$\omega\left[\frac{rad}{s}\right]$**	**0**	**0.5**	**1**	**1.5**	**2**	**2.5**	**3**
0	0	0	0.2772	0.4290	0.4424	0.5774	0.4510
0.3142	0.0993	0.2159	0.3422	0.5182	0.6498	0.7737	0.8430
0.5236	0.1042	0.2221	0.3460	0.5137	0.6382	0.8203	0.9289
1.5708	0.1445	0.2705	0.4195	0.5301	0.7110	0.8270	0.9605
3.1416	0.2795	0.3670	0.4515	0.5815	0.6895	0.8245	0.9520

Table 3-3: Mean values of current measured

From this result is possible to notice that, with low load, the motor does not need torque to stay still. This is due to the friction inside the motor which has not been considered in previous equations.

Applying the (3.6) on the non-null current measures of the static test, the resulting values of k_ϕ show an unexpected non-linearity.

$k_\phi \left[\frac{kg\cdot\frac{m^2}{s^2}}{A}\right]$					
$\mathbf{M}[Kg]$	1	1.5	2	2.5	3
k_ϕ	0.6900	0.6688	0.8647	0.8283	1.2724

Table 3-4: Values of k_ϕ

The mean value $\overline{k_\phi} = 0.8648$ is affected by k_ϕ variability, and it is not reliable. Anyway, the (3.7) is applied. The results are shown in Table 3-5.

Damping factor D $\left[kg \cdot \frac{m^2}{s^3}\right]$							
M$[Kg]$ / $\omega \left[\frac{rad}{s}\right]$	**0**	**0.5**	**1**	**1.5**	**2**	**2.5**	**3**
0.3142	0.2734	0.2899	0.3330	0.5133	0.5709	0.6077	0.4939
0.5236	0.1722	0.1842	0.2061	0.3005	0.3234	0.4415	0.4383
1.5708	0.0796	0.0880	0.1092	0.1092	0.1479	0.1509	0.1635
3.1416	0.0769	0.0706	0.0634	0.0687	0.068	0.0747	0.0794

Table 3-5: Damping factor D

The difference between the expected and the actual behavior of the system can be explained by the characteristics of the motor. As previously mentioned, the digital servomotor has an internal control circuit that moves the rotor to the required position. The motion law to lift the external mass was given pointwise. At slow speed, the movement was jerky. The motor rotates at speed higher than the required one, so it has to stop and start again to match the prescribed trajectory. For this reason, at each start it has to overcome the static friction, which becomes higher with the mass M. This can be noticed specially in the first two rows of Table 3-5. As speed increase, the damping D is reduced, because the movement is more fluid. At high speed, instead, the motor is not fast enough to match the required trajectory, so it never stops. For this reason, the damping is almost constant and is not affected by the increase of mass.

Going back to the choice of the batteries, looking at Table 3-3 it is possible to notice that a battery could power without problem four motors lifting 1kg mass each (current required $= 0.4515A \cdot 4 = 1.806A$. That correspond to $1\text{kg} \cdot \frac{3.9\text{cm}}{2} = 1.95\text{kg} \cdot \text{cm}$ load on each motor. The required torque for the pectoral fin motors, computed in equation (3.3), is only $0.468721\ \text{kg} \cdot \text{cm}$ and the caudal fins will have a lower load.

After these considerations, the two batteries MIKROE-1120 have been evaluated suitable for the application. Anyway, an ammeter will be installed to monitor the current consumption during the testing of the prototype.

3.4 Electronic components

The robot is equipped with some sensors and other electronic components. The only choice criteria are the compatibility with Arduino environment.

3.4.1 IMU

The Inertial Measurement Unit is needed to know the position of the robot in the 3D space. The chosen module is the GY-MPU9250[19]. It has a 3- axis MEMS gyroscope, a 3-axis MEMS accelerometer and a 3-axis MEMS magnetometer, for a total 9-axis motion tracking. It communicates with Arduino through I2C bus.

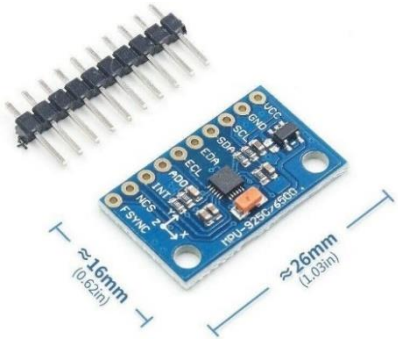

Figure 3.9: GY-MPU9250

In the Table 3-6 are reported the most interesting technical data regarding measurement range and sensitivity, extracted from the technical datasheet[19]. Gyroscope and accelerometer have a programmable scale.

[19] Datasheet available at: https://media.digikey.com/pdf/Data%20Sheets/TDK%20PDFs/MPU-9250_Rev_1.1.pdf, last visited on 02/11/2021.

GY-MPU9250 technical data		
Gyroscope	Full-Scale range $[^{\circ}/_{s}]$	$\pm 250/\pm 500/\pm 1000/\pm 2000$
	ADC Word Length	16 bits
	Sensitivity scale factor $\left[^{\mathrm{LSB}}/_{(^{\circ}/_{s})}\right]$	131/65.5/32.8/16.4
	Sensitivity scale factor tolerance @25°C	$\pm 3\%$
Accelerometer	Full-Scale range [g]	$\pm 2/\pm 4/\pm 8/\pm 16$
	ADC Word Length	16 bits
	Sensitivity scale factor $[^{\mathrm{LSB}}/_{\mathrm{g}}]$	16.384/8.192/4.096/2.048
	Initial Tolerance	$\pm 3\%$
Magnetometer	Full-Scale range [µT]	± 4800
	ADC Word Length	14 bits
	Sensitivity scale factor $\left[^{\mu\mathrm{T}}/_{LSB}\right]$	0.6
	Initial Calibration Tolerance	± 500LSB

Table 3-6: Technical data of GY-MPU9250 IMU

3.4.2 Camera

The camera module, at this stage of the prototype, has no role in the control of the swimming maneuvers. Its only scope is to record the images from the point of view of the manta. For this reason, the module OV7670 was chosen. It is available at low price and compatible with Arduino. Even if the resolution is low[20] compared to other sensors, it has been evaluated sufficient for the scope of this first prototype.

Figure 3.10: OV7670 camera module.

The sensor can operate at 640x480 VGA resolution, at 30fps. It has an automatic exposure control, gain control, white balance and image quality control. It communicates with Arduino using the I2C bus.

The camera could be improved in future developments of the manta, both on image quality side and on software implementation. Up to now, the camera has the only scope of saving the images on the SD card. A more advanced model could use the images to recognize the environment and navigate autonomously.

3.4.3 SD card reader

The micro SD is used in this project for two purposes. The first is to store data during the testing of the prototype, such as position of the motors, measurements from the IMU and images from the camera. The second one is to store some parameters outside of the main code. The Arduino reads the values of the parameters and generates the control law as a function of the parameters. In this way is possible to test the influence

[20] Technical datasheet available at the following link, last visited on 02/11/2021
https://www.google.com/url?sa=t&rct=j&q=&esrc=s&source=web&cd=&ved=2ahUKEwiKlqTdxvnzAhX5iv0HHWzlBRwQFnoECAYQAQ&url=https%3A%2F%2Fwww.openhacks.com%2Fuploadsproductos%2Fov7670_cmos_camera_module_revc_ds.pdf&usg=AOvVaw2B-z6f7rrHWNNmsExH9ENx.

of the parameters on the motion without uploading the code on the Arduino every time.

The micro SD reader is connected to the Arduino through the SPI interface

Figure 3.11: Micro SD SPI interface

3.4.4 Wi-Fi module

The wireless connection is provided by the ESP8266-01 module. It is a microcontroller with integrated Wi-Fi circuit, and can communicate with the Arduino using the UART serial communication standard. The firmware esp-link by Jeelabs[21] has been uploaded on the ESP8266-01. The firmware creates a web server with many features, included a serial console from which is possible to control the Arduino. The firmware is supposed to flash programs on Arduino as well. Unfortunately, as previously mentioned, the Arduino Due cannot be programmed via UART (differently from the other Arduino models), so the wireless communication is limited to the serial monitor and the reset of the board. The chapter 6 will deep dive in these aspects.

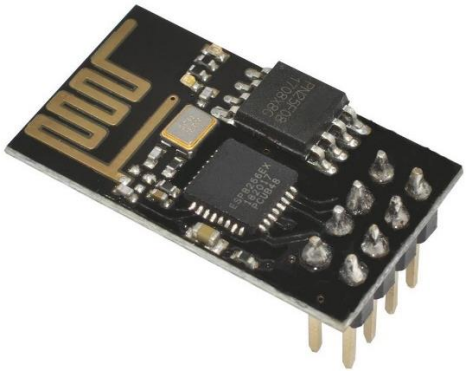

Figure 3.12: ESP8266-01

[21] Documentation available at https://github.com/jeelabs/esp-link, last visited on 02/11/2021.

3.4.5 Ammeter

The presence of the ammeter is useful to monitor the current delivered by the battery during the testing phase, to control whether the batteries are working correctly or not. (for further details see paragraph 3.3.3).

The module installed is based on the ACS712ELCTR-05B-T chip by Allegro MicroSystems[22]. It can measure currents in the range $\pm 5A$, with sensitivity equal to 185 mV/A and output for null current equal to 2.5V (see Figure 3.13b). For the Arduino Due the maximum voltage supported by the analog input is 3.3V, so the max current measurable without damaging the microcontroller is:

$$A_{max} = \frac{3.3V - 2.5V}{0.185\,{}^{V}/_{a}} = 4.32A$$

Considering that the max nominal continuous current provided by the battery is 2A, and the max peak current is $2\sqrt{2}A = 2.82A$, it has been considered safe to connect the ammeter directly to the Arduino, knowing that if the current exceeds 4.32A the microcontroller may be damaged. It also could be possible to reduce the output voltage with a voltage divider, but this would reduce also the sensitivity of the ammeter.

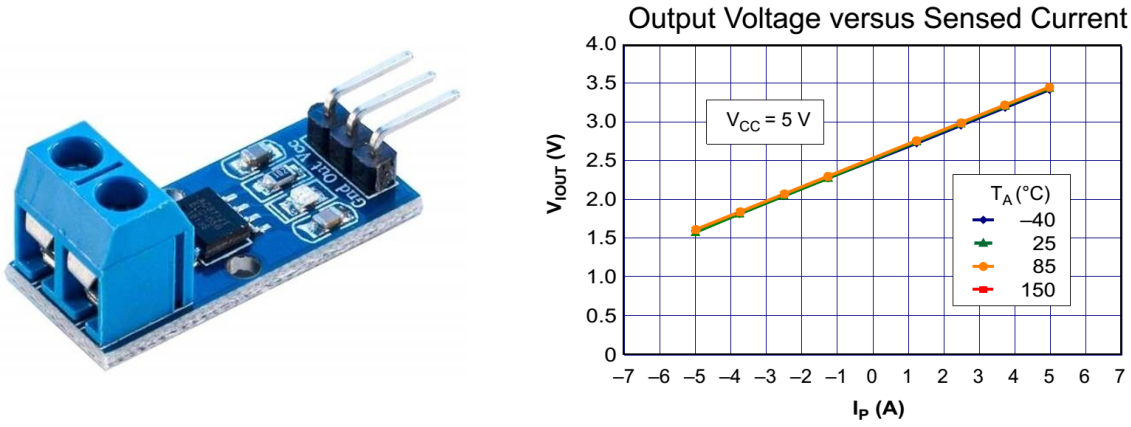

(a) The module (b) Input-Output relation

Figure 3.13: ACS712 module

[22] Technical datasheet available at: https://www.digikey.it/it/datasheets/allegromicrosystemsllc/allegro-microsystems-llcacs712datasheetashx, last visited on 02/11/2021.

4. Pectoral fins

The design of the pectoral fins is based on the researches available in literature, following the general suggestions coming from the papers. The optimization of fin shape is not an objective of this work and the result is meant to be a prototype for a future optimization work.

4.1 Shape

4.1.1 Profile

The profile of the fin reproduces as accurately as possible the fin profile oc a real cownose ray. Cai et al. [18, 19] traced the profile of the pectoral fin of a cownose ray, scaled with respect to the chord length (Figure 1.11b). The fin profile is obtained by overlapping some reference point to the image from the paper in the software MATLAB from MathWorks® and connect them with straight segments (Figure 4.1a). The obtained curve is a retracing of the profile. This curve is then scaled to the actual chord length of the robot, which is the same of the NACA 0020 profile used for the main body, $CL = 260mm$ (Figure 4.1b).

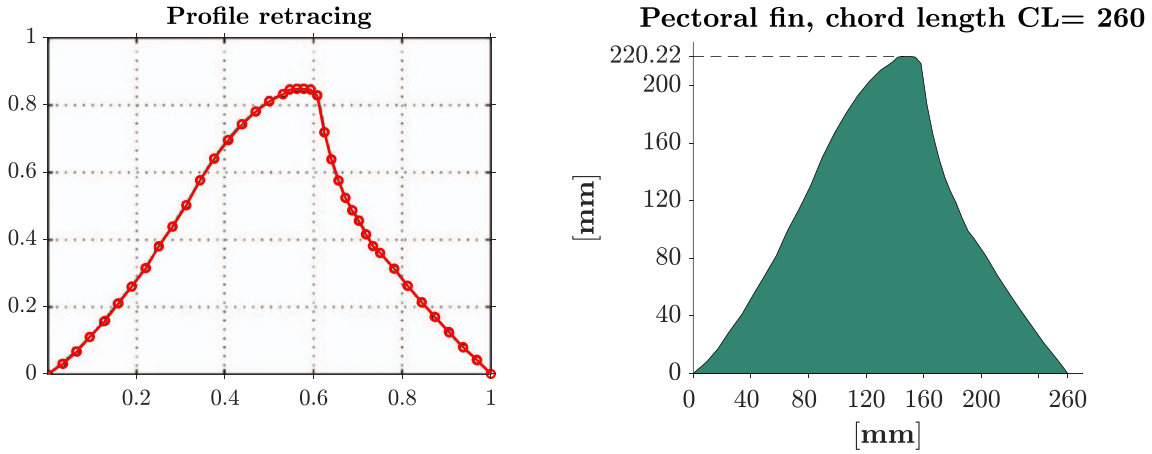

(a) Profile retracing on image from

(b) Profile scaled to the actual dimension

Figure 4.1: Pectoral fin profile

4.1.2 Thickness

In literature there are many researches about the best stiffness distribution in flexible fins. The thickness was defined according to the results of these researches.

Ziegler et al. [33] studied the best stiffness distribution in chordwise direction. They built a fin made of rigid section. Each section is connected to the other with a rotational spring. For each joint, a servomotor controls the stiffness of the spring, allowing to measure the performances of the fin with respect to stiffness distribution.

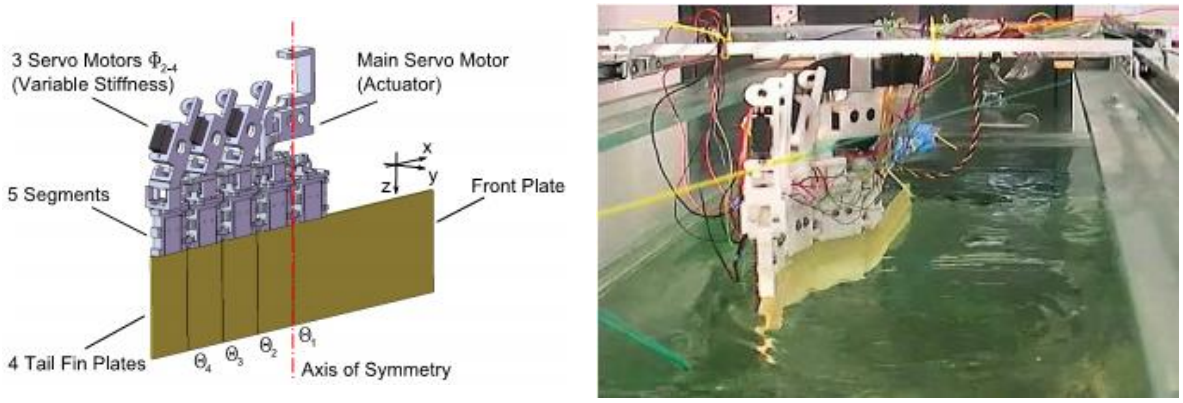

(a) CAD drawing (b) Photo

Figure 4.2: Ziegler et al. experiment [33]

The result of the experiment is that "A heterogeneous distribution […] outperforms the homogeneous distribution […] in terms of thrust."[23] In particular, the best result is obtained for stiffness decreasing along chordwise direction.

Riggs et al. [34] made a comparison between a fin with a NACA 0012 airfoil profile and the stiffness profile of the Pumpkinseed Sunfish (Lepomis gibbosus) in chordwise direction. The biomimetic profile appears to be thicker in the initial and middle section of the fin, near the leading edge, while becomes thinner in the rear part, arriving at the trail edge almost flat (Figure 4.3). Moreover, they also compared two different rubber compounds, one harder than the other.

The result of the experiment is that at low frequencies the biomimetic profile generates a slightly higher thrust while at high frequencies the performance of the airfoil drops, and the biomimetic profile generates a thrust up to 80% higher.

[23] [34], paragraph III.D.

Regarding the compounds, the experiment shows that, for the same stiffness profile, the hard compound generates around double thrust with respect to the soft one.

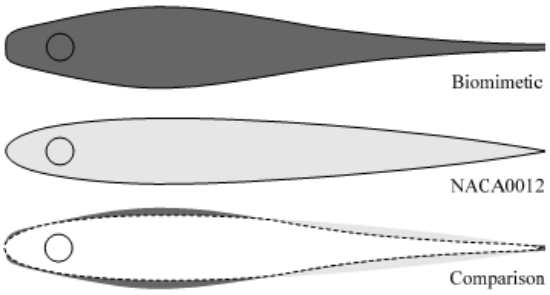

Figure 4.3: Profiles compared by Riggs et al. [34]

Chew et al. [27] performed a different experiment. They measured the performances of different fins made by a PVC sheet glued on a 3D printed leading edge. In this case, the different designs of the leading edge change the stiffness in spanwise direction, while the stiffness in chordwise direction is determined by the PVC sheet. The four leading edge profile are shown in Figure 4.4.

The object of the experiment was the effect of sweep angle on thrust generation. The results show that sweep angle does not influence the performance. At the same time, the less flexible tapered leading edge (design 3 in Figure 4.4) shows a slightly better performance both in still water and in free stream.

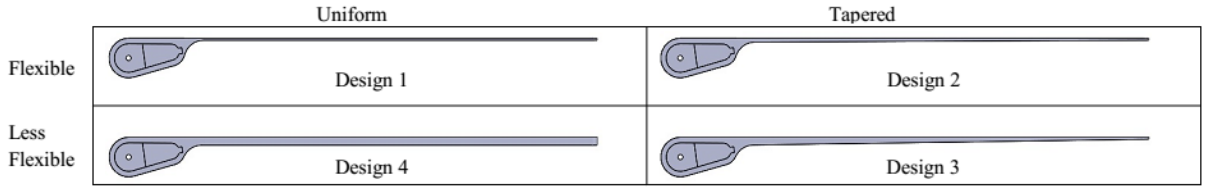

Figure 4.4: Leading edges in Chew et al. experiment [27]

Combining the results of this paper, a bidimensional fin stiffness profile was designed using Matlab. On the profile in Figure 4.1b ten sections parallel to the fin base were identified. For each section ten control points in between minimum and maximum are defined. The control points are denser near the leading edge in order to better control the shape (Figure 4.5a). In this way, the fin is divided in a 10x10 matrix[24].

[24] External profile point coordinates and half thickness in correspondence of control points are reported in detail in Appendix B.

For each point of the matrix, the half thickness of the fin in the corresponding position has been defined arbitrarily, taking into account the following constraints:

- The thickness distribution has a decreasing gradient in spanwise direction.
- The shape of each section should be similar to the biomimetic profile from Riggs et al. [34]: thick near the leading edge and thinner, almost flat, near the trail edge.
- The sections on the leading edge near the fin base should be thick enough to contain the fin stick (details in the next paragraph).
- The trail edge should not be too thin in order to be feasible. For this reason, a control point is placed at the 98% of the chord length.

The result of this process is the fin surface depicted in Figure 4.5c.

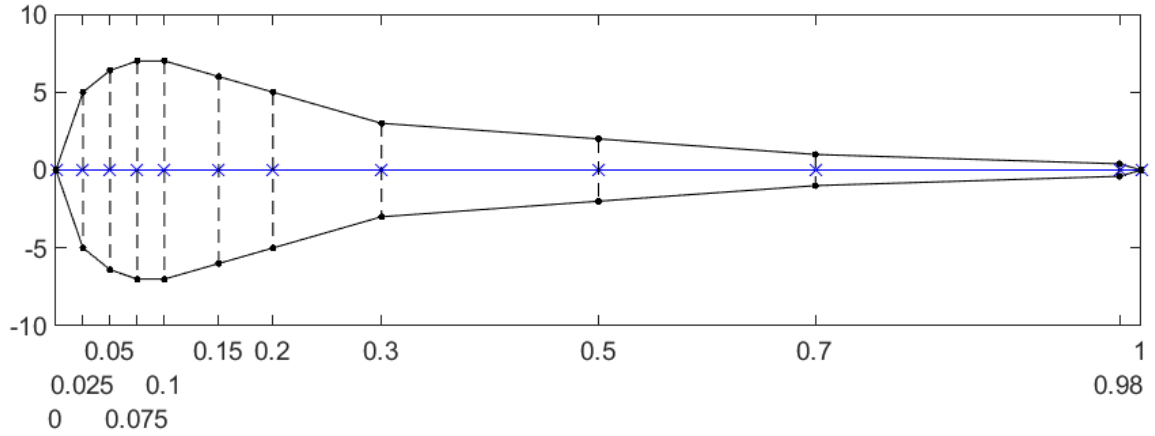

(a) A section with unitary chord length. Control points coordinate highlighted on x axis

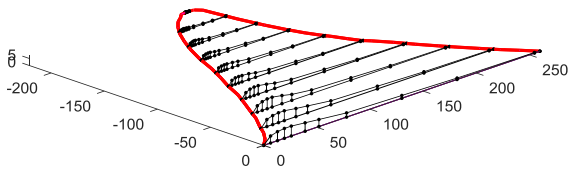

(b) The ten sections

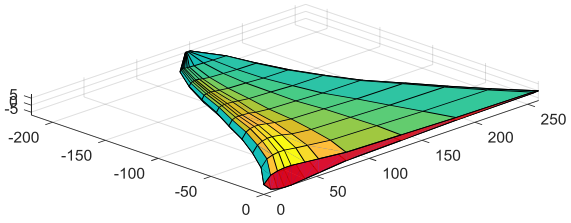

(c) The resulting fin surface

Figure 4.5: Fin surface definition

4.2 Design and manufacturing

The surface obtained in Matlab must converted to a design feasible and compatible with the motor shaft.

The idea is to create a rigid stick to connect to the motor bracket. The stick can be insert inside the fin near the leading edge. Then a system to join the fin and the stick is necessary.

4.2.1 The sticks

The first step to design the sticks is the choice of the manufacturing process. For sake of simplicity, it was chosen to build it from a C-shaped aluminum bar, with the section in Figure 4.6a. To have a comparison term, it was chosen to build a second version of the stick in a different material. The C-shaped PVC profile in Figure 4.6b was chosen. The scope of having two different versions of the stick is to insert them in the same fin and evaluate how the different stiffness influences the movement of the fin.

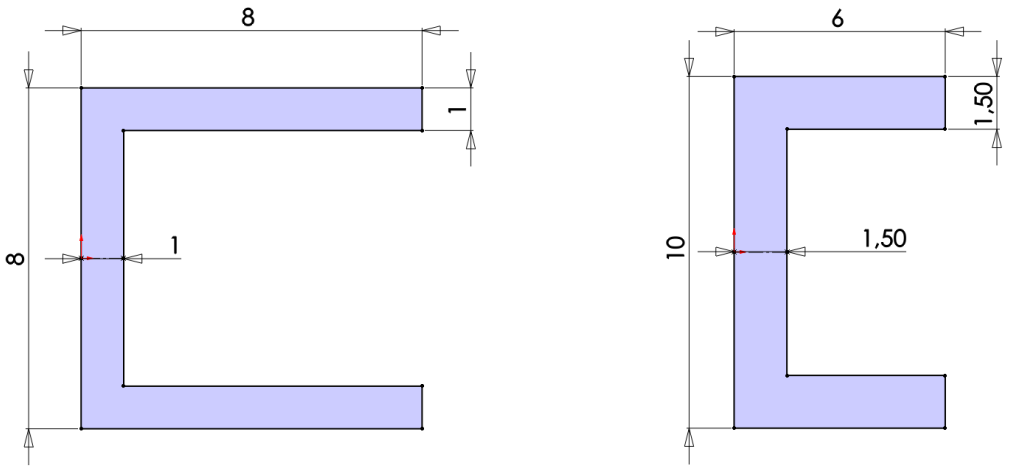

(a) Aluminum profile (b) PVC profile

Figure 4.6: Profiles of fin sticks

The sticks are bent in order to form two specific angles with respect to the manta front (Figure 4.7a). The 25° angle is designed to align the stick with the leading edge of the fin. The 50° angle instead is needed to shift the fin backward in order to align the base of the fin with the chord of the airfoil profile. From Figure 4.7b is possible to notice that the fin profile remains slightly ahead with respect to the body. On the other hand, an angle greater than 50° would cause interference between the stick and the shell, preventing the correct motion of the fin.

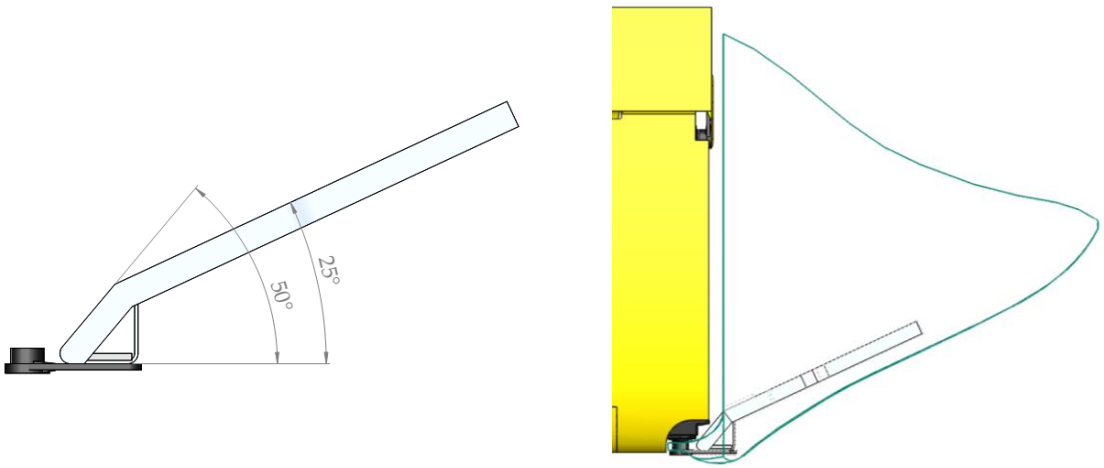

(a) Stick angles (b) Fin position with respect to the body

Figure 4.7: Pectoral fin stick, top view

The profile of the stick along the leading edge is reduced near to the tip (Figure 4.8). In this way the bending stiffness of the tip is reduced, according to the results of experiments by Chew et al. [27] (see Figure 4.4).

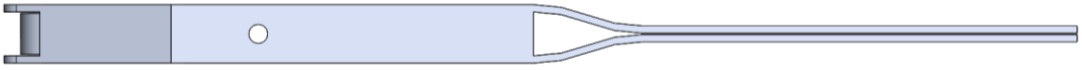

Figure 4.8: Pectoral fin stick, perpendicular view

During the manufacturing process, described in paragraph 5.2.1, the PVC profile turned out to be unfeasible due to the fragility of the material when subjected to bending. For this reason, a hybrid stick is realized. The initial part is in aluminum, while the tip is in PVC in order to take advantage of the higher flexibility.

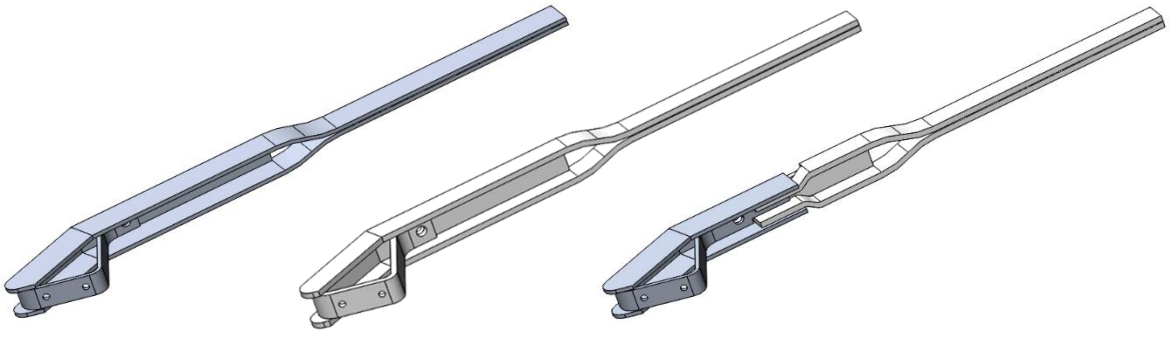

(a) Aluminum (b) PVC (unfeasible) (c) Hybrid

Figure 4.9: Pectoral fin sticks

Finally, to connect the fins to the motors, the sticks are joined to the motor bracket using a bolt joint.

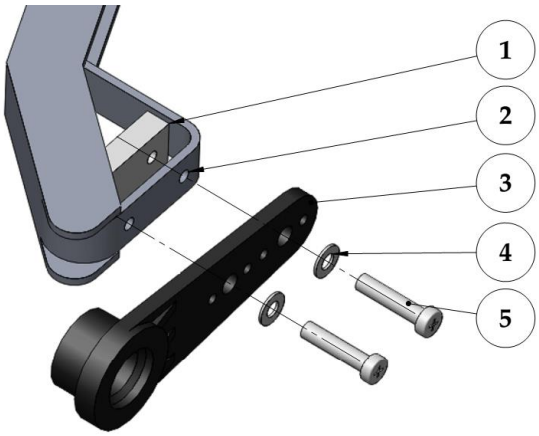

1	Aluminum plate with threaded holes
2	Pass-through holes
3	Motor bracket
4	Washer
5	M2 screws

Figure 4.10: Fin stick-bracket joint

The stick design limits the movement of the fin due to the interference with the shell. The amplitude of the movement allowed by the nominal design is almost ±30° (Figure 4.11a). The interference is near the superior edge of the shell (Figure 4.11b), so it could be possible to chamfer the angle in order to eliminate the interference. This modification on the shell has not been performed yet because the fin design is meant to be improved and changed.

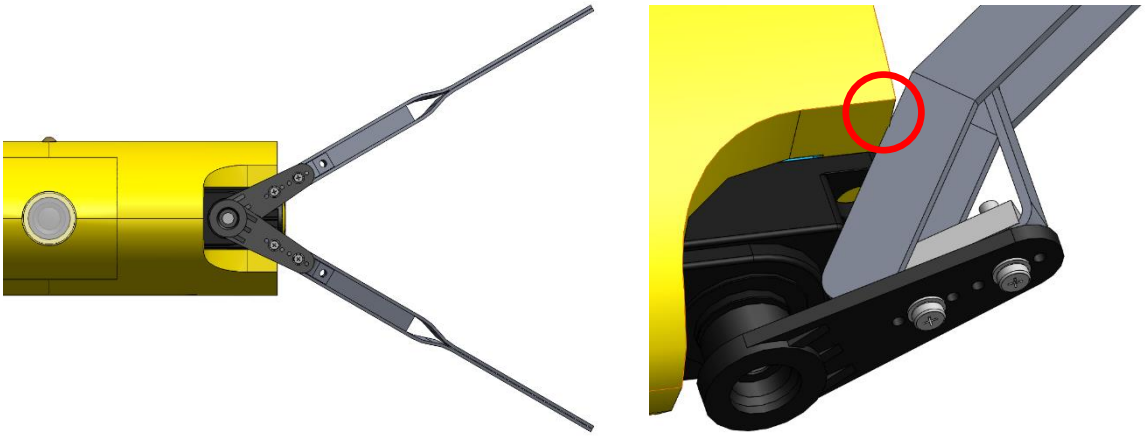

(a) Fin angles without interference (b) Stick-shell interference, detail

Figure 4.11: Fin movement limits

4.2.2 The fins

The profiles built in MATLAB in the previous step are imported inside SolidWorks as 3D curves. The curves are joined with a loft in order to obtain the solid geometry. Then, for the connection with the sticks, the cavity is created. The dimensions of the cavity are designed for containing both the aluminum and hybrid sticks. The presence of the hole and the cavity defines the thickness in this part of the fin. Some material is added in the front part to cover the screws. An elastic loop turns around the shaft of the bracket to prevent the slipping out.

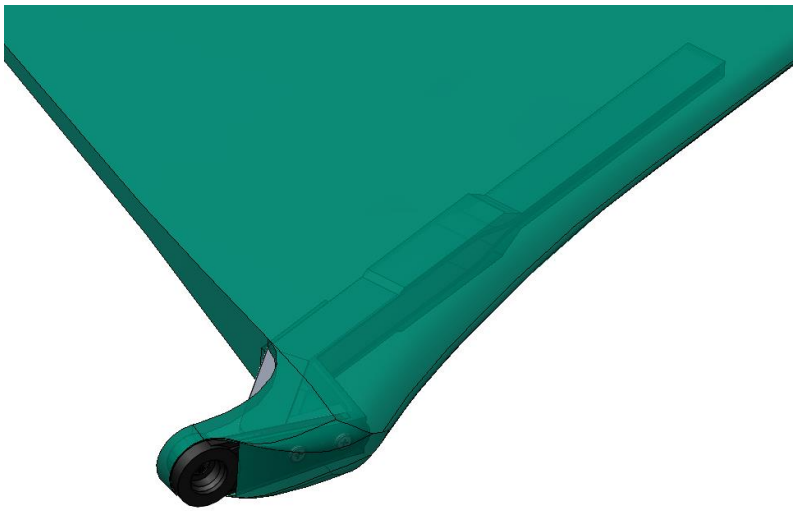

Figure 4.12: Detail of fin-stick joint

4.3 Simulation and testing

4.3.1 Frequency reduction ratio

The robot thrust is generated by the movement of the flexible fins in the water. The interaction between the solid and the fluid generates vortices that push the robotic fish in forward direction. This interaction is quite complex to simulate. The use of CFD (Computational Fluid Dynamic) together with FEA to determine the deformation of the fin would produce an enormous computational load.

To reduce the time required for simulation, a different approach is applied. As the most common way of generating thrust in water is by propellers, researches in that field are analyzed. Carlton [35], analyzing the vibrations in propellers blades, shows that it exists a frequency reduction ratio defined as:

$$\Lambda = \frac{frequency\ of\ mode\ in\ water}{frequency\ of\ mode\ in\ air} \tag{4.1}$$

Under the hypothesis of undamped motion, considering the blade of the propellers as a one degrees of freedom system, the mode frequency can be written as:

$$f = \frac{1}{2\pi}\sqrt{\frac{k}{m}} \tag{4.2}$$

Considering that the stiffness of the blade does not change, substituting the (4.2) in the (4.1), the frequency reduction ratio can be expressed as a mass ratio:

$$\Lambda = \sqrt{\frac{mass\ of\ the\ blade}{mass\ of\ the\ blade + added\ mass\ of\ water}} = \sqrt{\frac{m_b}{m_b + m_w}} \tag{4.3}$$

This ratio is shown to be variable with the frequency mode: it is around 0.6 for the fundamental and tends to 1 as the harmonic number increase. At the same time, Carlton shows that the mode shape inside and outside water are quite similar.

The testing applied of the fin are oriented to verify if a similar approach can be applied to flexible fins. The FEA is used to identify the modes of vibration of the fin. Then, the deformation of the fin underwater is observed. Comparing the mode shapes underwater and the natural frequencies, the reliability of the method is discussed. The results of the test could be used to develop an optimization method for flexible fin design.

4.3.2 Finite Element Analysis

The Finite Element Analysis is performed on the software Abaqus. The geometries of the fin, the sticks and the bracket are imported from the CAD. The bracket has been considered as a rigid body, because its deformability is negligible with respect to the other parts.

The base units of measure used for the analysis are millimeters, seconds and kilograms. The derived units of measures are shown in Table 4-1.

	Units of measure in Abaqus	
	Physical quantity	**Unit of measure**
Base	Length	mm
	Time	s
	Mass	kg
Derived	Acceleration	$\frac{mm}{s^2}$
	Force	$kg \cdot \frac{mm}{s^2} = 10^{-3}N$
	Pressure	$\frac{10^{-3}N}{mm^2} = 10^{-3}MPa$

Table 4-1: Units of measure in abaqus

The materials are defined as elastic homogeneous materials, characterized by density, Young's modulus and Poisson ratio.

While for aluminum and PVC the material properties are taken from literature, for the silicone rubber it was necessary to compute them. The density is measured from a sample in the laboratory. The Young's modulus E can be computed from Shore hardness S using different empirical formulae[25]. Gent's relation (4.4) is valid for A-Shore>40, while the formula that uses the error function (4.5) better fits the experimental data at any hardness.

$$E[MPa] = \frac{0.0981(56 + 7.62336S)}{0.137505(254 - 2.54S)} \tag{4.4}$$

$$S = 100\ erf\left(3.186 \times 10^{-4} E[Pa]^{1/2}\right) \tag{4.5}$$

Applying the (4.4) and the inverse of the (4.5), the resulting Young modulus for $S = 45$ is, respectively, $E_{Gent} = 2.0379MPa$ and $E_{erf} = 1.76MPa$. The first-try value used is E_{erf}. This parameter is later tuned comparing the physical and simulated behavior of the fin (details in paragraph 4.3.4).

[25] From https://en.wikipedia.org/wiki/Shore_durometer, last visited on 10/11/2021.

	Material properties		
	Density $\left[k/mm^3\right]$	**Young's modulus** $[10^{-3}MPa]$	**Poisson Ratio**
Aluminum	$2.7 \cdot 10^{-6}$ [26]	$69 \cdot 10^{6}$ [26]	0.32 [27]
PVC	$1.4 \cdot 10^{-6}$ [28]	$3.4 \cdot 10^{6}$ [28]	0.4 [29]
Silicone rubber	$1.22 \cdot 10^{-6}$	1760	0.495 [27]

Table 4-2: Material properties

The rigid motor bracket has all the six degrees of freedom constrained. The stick is constrained by imposing a tie connection between the bracket and stick on the faces bolted together in the real fin. The rubber fin is constrained by imposing again a tie connection between the face of the cavity and the face of the stick. This last constraint is slightly different from the real one. In fact, in the real fin the cavity is a bit larger than the stick in order to fit both the stick version. The connection is caused by friction, and some slippage is possible. For the Abaqus model instead it was necessary to create a cavity that perfectly fits each of the sticks and any slip in prevented.

The analysis is formed by two steps. First, a static step with the gravity load active is applied. This step is useful to measure the fin deflection and compare it to the physical fin. Then, a frequency step is performed. The first five modes of vibration are analyzed for each fin.

4.3.3 Deflection measure

The first observation performed is a measure of the deflection of the fin in air due to gravity load. The experiment is performed by fixing the electric motor, place the motor hinge parallel to the ground, marking the height reached by the fin tip and measuring the distance from the top of the vertical wall. The experiment is performed with the

[26] https://www.agnellimetalli.com/prodotti/alluminio/leghe/caratteristiche-fisiche.
[27] https://en.wikipedia.org/wiki/Poisson%27s_ratio.
[28] https://en.wikipedia.org/wiki/Polyvinyl_chloride.
[29] https://polymerdatabase.com/polymer%20physics/Poisson%20Table2.html.

aluminum and hybrid sticks placed inside the two fins. The results, considering also the offset of the motor shaft with respect to the top of the wall, are shown in Table 4-3.

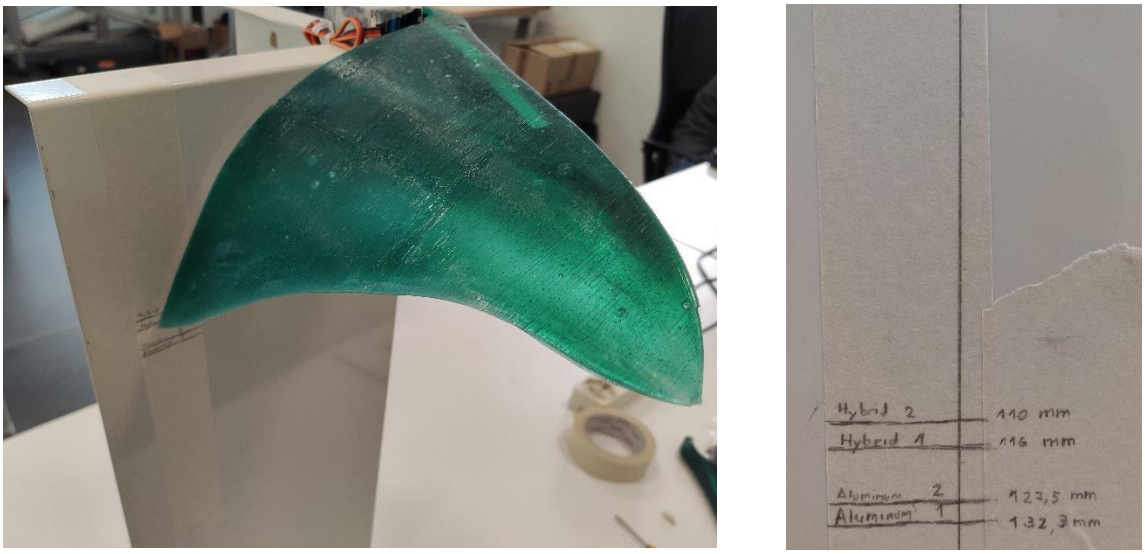

(a) Experiment setup (b) Measurements

Figure 4.13: Fin tip deflection measurement

	Fin tip deflection [mm]	
	Fin 1	**Fin 2**
Aluminum stick	142.5	137.7
Hybrid stick	126.2	120.2

Table 4-3: Fin tip deflection

The result is different from expectations, because the more flexible hybrid fin shows a lower deflection. The reason is that the aluminum stick is thinner than the hybrid one, so it has some backlash in vertical direction inside the cavity. This backlash causes the higher deflection measured experimentally.

Another observation is that the deflection of the two fins are not identical. The reason is the different density due to the presence of bubbles in the rubber. Anyway, the deflection difference between the two fins is $\approx 5.5 \div 6\ mm$, which is negligible during the motion.

This experiment shows that the FEM model should be improved. In fact, the fin model was simplified neglecting the backlash and rigidly connecting the faces of the stick and

the fin. The measurements show that this coupling should be improved in order to have a reliable model.

4.3.4 Young's modulus tuning and results

The tuning of the Young's modulus is performed on the hybrid stick model. For this stick the effect of backlash should be less relevant, because the stick is thicker.

For $E = E_{erf} = 1.76MPa$ the deflection of the fin computed by Abaqus is $u = 298.5mm$, way higher than the measured one. Even for $E = E_{Gent} = 2.0379MPa$ the deflection is $u = 251.3mm$ really high. The correct deflection $u = 123.7mm$ is obtained for $E = 4.3MPa$.

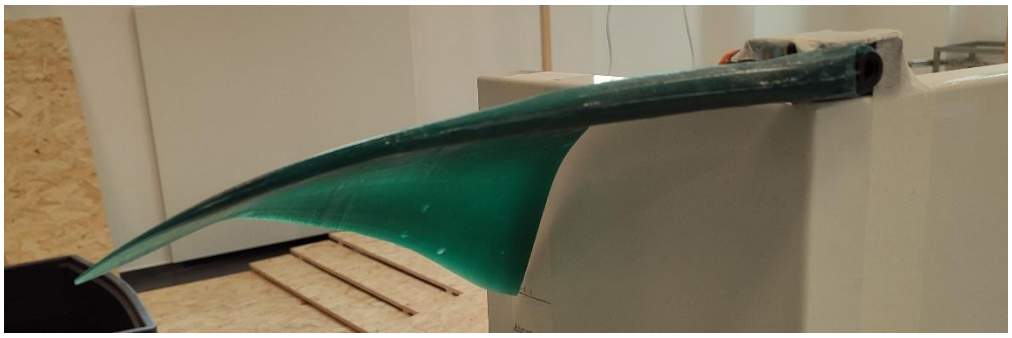

(a) Fin deflection from the experiment

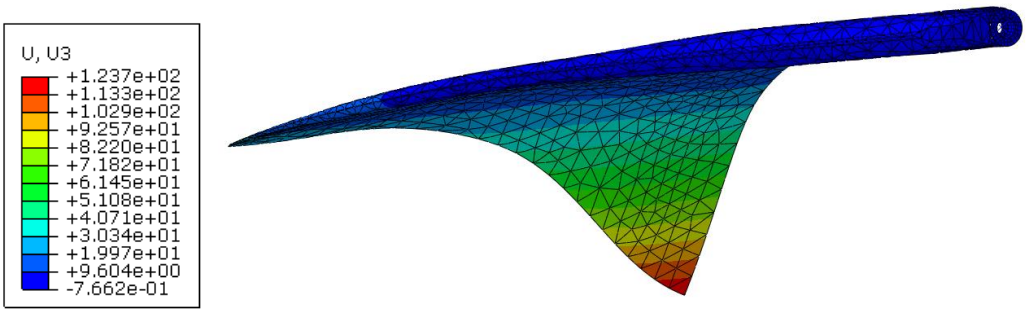

(b) Fin deflection from the finite element model. Contour of vertical displacement

Figure 4.14: Fin deflection with tuned Young's modulus

From the comparison of the real deflection and the simulated one (Figure 4.14) is possible to notice that the fin base deflects in the same way. The leading edge, instead, appears to be more flexible in the real fin than in the finite element model.

The reason could be, again, the inaccurate modelling of the interaction between the rubber fin and the stick. The contact is over-constrained in the model, causing the slightly higher stiffness of the leading edge.

Looking instead at the vibration modes[30], the frequencies are higher than the ones initially computed due to the change of Young's modulus. During the design process of the fin, the modes analysis was considered in order to have the natural frequencies in a feasible range for the motor[31]. Due to the change of parameter, the fins are no more optimized for the frequency range, so it could be difficult to oscillate the fin at the right frequency for the observation.

4.3.5 Underwater movement observation

The underwater behavior of the fin is observed in a small tank. An aluminum structure holds the fin and the motor inside the tank. The observation is performed by filming the flapping movement from underwater.

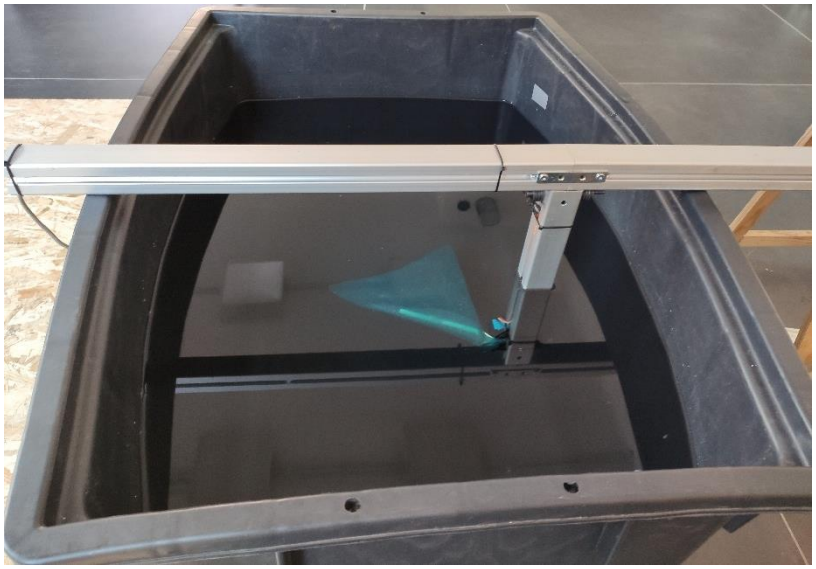

Figure 4.15: Water tank to test the fin movement

The first thing to notice is that, when the motor is still, the fin stays horizontal. This observation allows to neglect the gravity load when performing the frequency analysis in Abaqus.

For the dynamic observations, the motor moves the fin with a sinusoidal oscillation. Different amplitudes and frequencies have been observed from different point of views. As an example, in Figure 4.16 are shown eight instants from a flapping cycle

[30] Mode shapes are shown in Appendix C.

[31] From Carlton computations, the frequency in water is around 0.6 times the frequency in air [35].

from the frontal point of view. The motor oscillates at frequency $f = 0.65Hz$ and amplitude $A = 45°$.

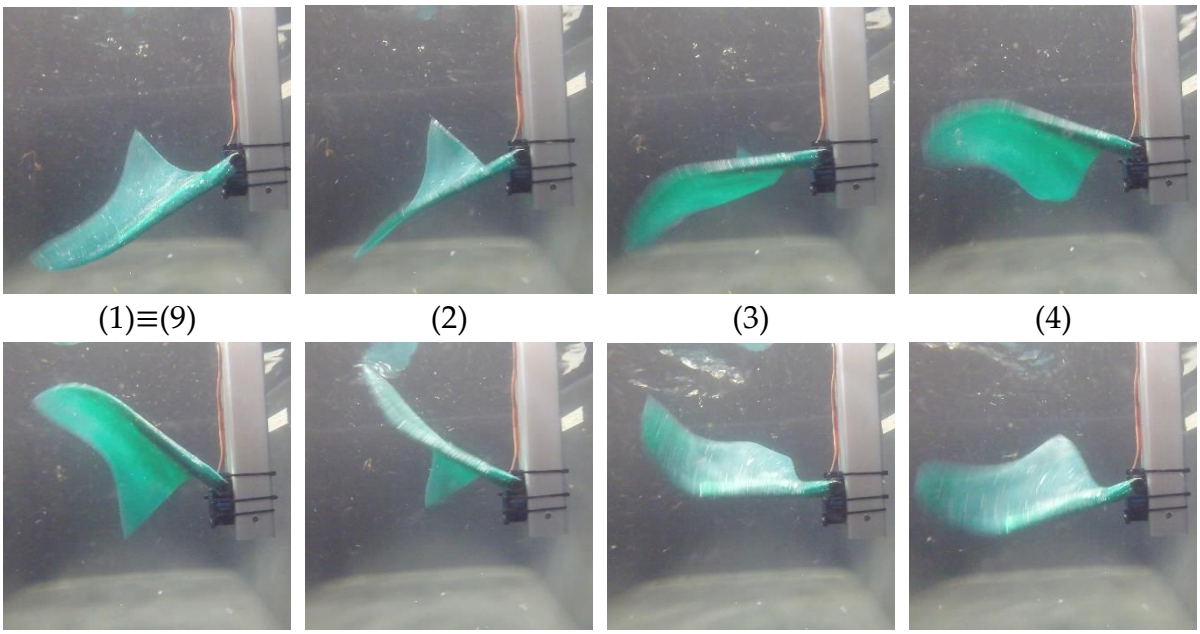

Figure 4.16: 8 frames from one flapping cycle

At this stage of the work, the comparison between the modes of vibration from the FEA and the modes of vibration observed on the physical fin has not been performed yet.

Some qualitative observations can be done. The fin tip, at the end of the leading edge, deforms in a similar way compared to the biological reference. The movement of the fin moves the water backward generating a perceivable thrust force on the aluminum structure.

The fin also has some limitations, that could be taken into account for improving it in the next design. The tip of the fin trail edge does not contribute to the thrust generation. It can be observed in frame (2) that it remains up when the stick moves upward and vice versa in frame (6). In the following frames (3) and (7) the movement of the stick inverts the deformation of the fin base, and when the stick is steady in the peak position (5) and (9) the tip is again on counterphase.

This behavior is caused by the low stiffness of the fin base. The fin has not enough elastic potential energy to move the water and recover its shape and so it deforms passively under the effect of water resistance. The fin should be improved by increasing the base stiffness, in order to move the water and generate thrust.

5. Construction of the prototype

5.1 Main body

5.1.1 3D-printed components

The main body of the prototype is handcrafted in the laboratory except for few components. The cover, the caudal fins and the core extensions of the robot are realized by LPD (Layer Plastic Deposition) 3D printing. The material used is the Z-ULTRAT in yellow color, a proprietary ABS blend from Zortrax[32].

This technology allowed the realization of complex shapes like the shell, and the production of multiple versions of the same component in order to improve the design.

On the other hand, 3D-printed pieces have some defects and needs to be refined.

The surface created by LPD presents some cracks and porosities, even increasing the density settings of the 3D-printer. This aspect is a problem for the impermeability of the core. In order to fill the cavities, the pieces are treated with acetone. The acetone chemically melts the plastic material and allows to merge the layers, obtaining a smother surface. This process is applied to all the 3D printed parts.

Using the same principle, some material can be melted an added to fill cracks, as for the detail of the shell shown in Figure 5.1.

[32] https://zortrax.com/filaments/z-ultrat/, last visited on 06/11/2021.

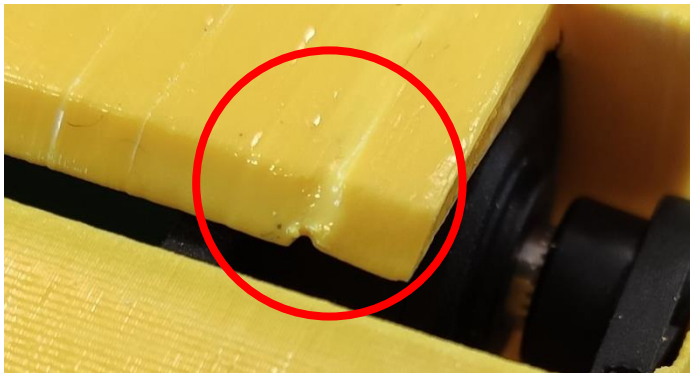

Figure 5.1: Filled crack in the shell

A second problem related to the layer structure of the 3D-printed parts is the anisotropy. Each layer is resistant with respect to in-plane stresses, but the out-of-plane traction stress induces the delamination of the layers. The acetone treatment slightly improves this behavior reducing anisotropy, but some attention regarding printing direction is still needed. For example, the coupling plugs have fibers parallel do disassembly direction to guarantee the mechanical resistance.

Sometimes the smoothness of the surface prevails on the mechanical requirements. For example, the two shells are printed so that each layer follows the airfoil profile. In this way, the layers are perpendicular to the disassembly directions, thus the most stressed points of the shells had to be reinforced with some brass wires 0.6mm thick which are glued to the inner surface of the shells, perpendicular to the layers. They contribute to absorb traction stress and avoid delamination.

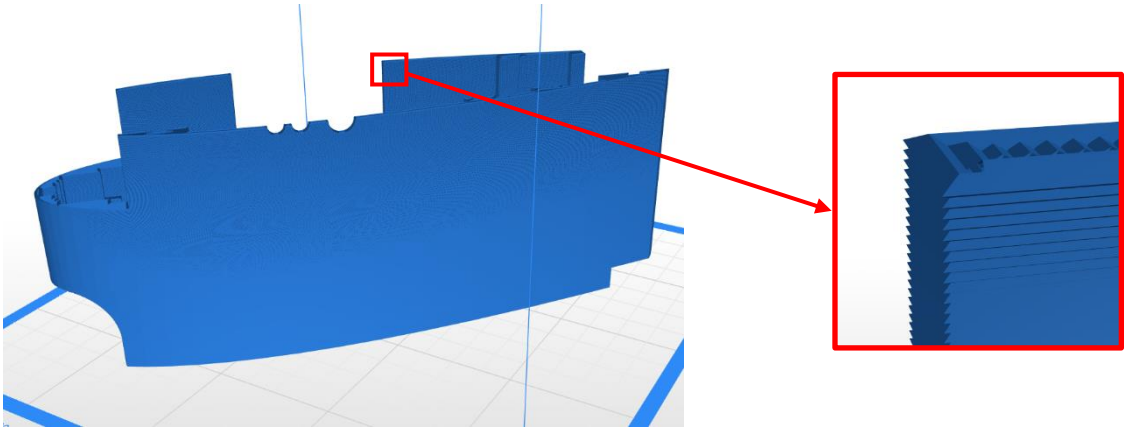

Figure 5.2: Printing direction of the shells

Figure 5.3: Brass wire reinforce, detail

A further limitation of the 3D-printed parts are the coarse tolerances, due to the limited resolution of 3D printing, the thermal stresses induced during the printing and the acetone treatment. In order to align the pieces and consent the interlockings, some finishing process is applied.

5.1.2 Chassis

The aluminum structure of the chassis is obtained laser cutting from an aluminum layer 2mm thick. The threading of the holes and the bending, instead, is handcrafted in the laboratory.

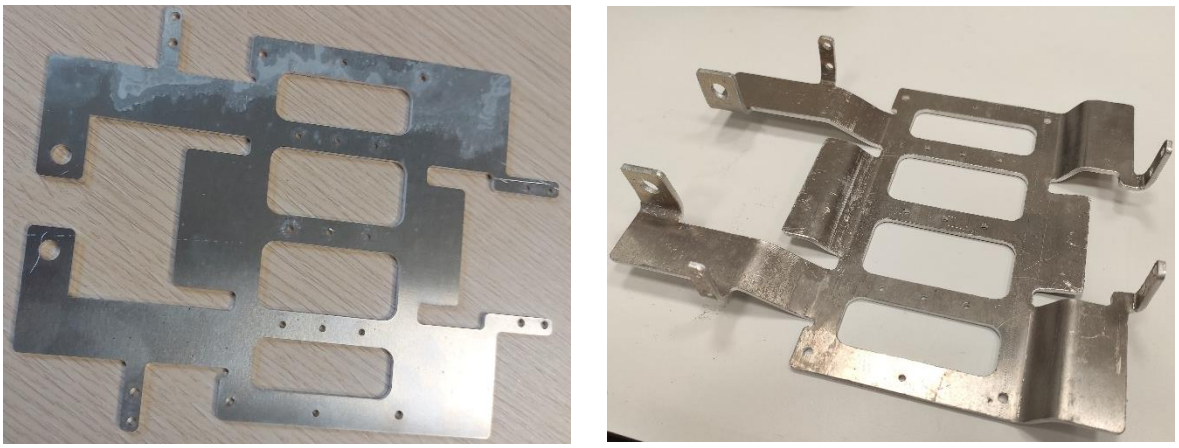

(a) Chassis before bending (b) Chassis after bending

Figure 5.4: Making of the chassis

The tolerances of the folds are not precise due to the handcraft job. The interlockings between all the pieces are obtained by filing both the metal and the 3D-printed pieces and adding material to the plastic components while assembling.

All the refinements needed to allow mounting have been carried out and the assembly of the robot has been completed, as shown in Figure 5.5.

Figure 5.5: Main body assembled

5.2 Fins

5.2.1 Sticks

As previously mentioned, the sticks are manufactured starting from C-shaped bars. In order to obtain the designed geometry, the extruded profiles are cut and bend by hand. In the initial part the flanges are removed, and the web is bent in order to obtain the flat surface that connects to the motor bracket. On this surface there are two pass-through holes for the bolts. The web then is bent up to meet the web of the 25° part. The bolted joint of the two webs increases the stiffness and the mechanical resistance of the part. In the hybrid version of the stick, the web of the PVC bar is connected to the same bolt, closed between the two aluminum webs.

To further join the two sticks, the PVC flanges are bent inside the aluminum flanges, and the aluminum web keeps them separated. Finally, the connection is fixed with some glue

The reduced section at the tip of the stick is obtained by removing the web, and by bending the two flanges toward the middle plane. As PVC cannot be bend plastically, some tape keeps the flanges in the desired position.

For the bolted joint between the stick and the motor bracket, the two nuts are substituted by a small aluminum plate 3mm thick, with two threaded holes. The plate is glued to the stick to keep it in the right position, easing the assembly of the two pieces.

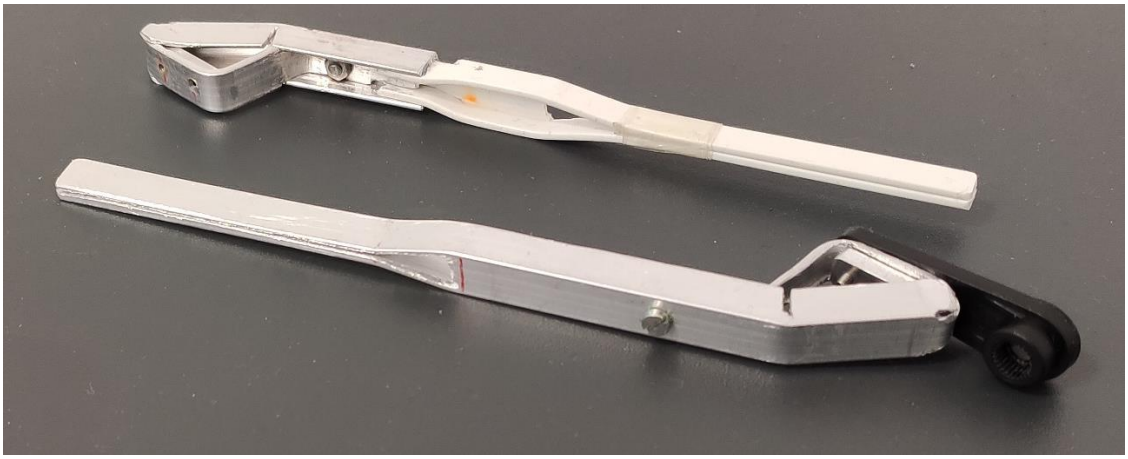

Figure 5.6: The two sticks manufactured

5.2.2 Flexible fins

The fins are realized in silicone rubber. The hardness of the material is Shore A 45, which is quite high among the rubbers available on the market. The manufacturing is performed by mixing the base and the catalyst in equal ratio and casting them in a mold. Some pigment is added in order to obtain the desired color.

The mold is realized in 3D printing. It is composed by a superior mold, and inferior mold, and a core for the cavity for the sticks. The superior mold has some holes for the spill of the extra material. Each of the two molds is formed by three pieces joined due to the limited dimensions of the 3D printer. During the curing of the material the molds are closed by M6 bolts.

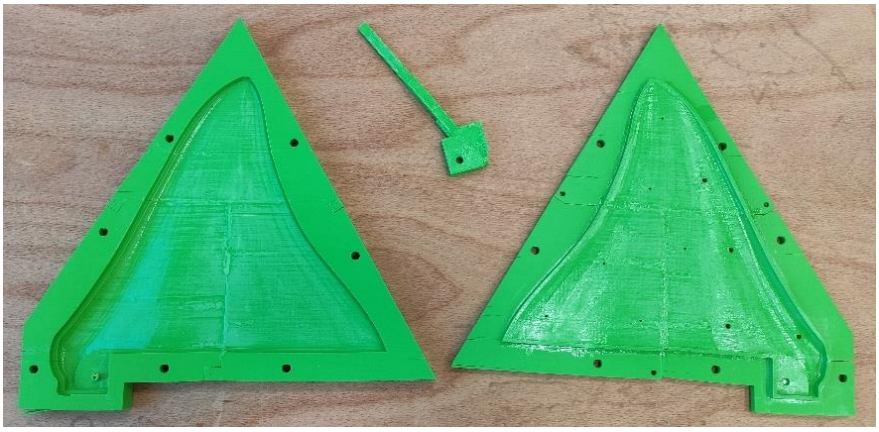

Figure 5.7: Photo of the molds

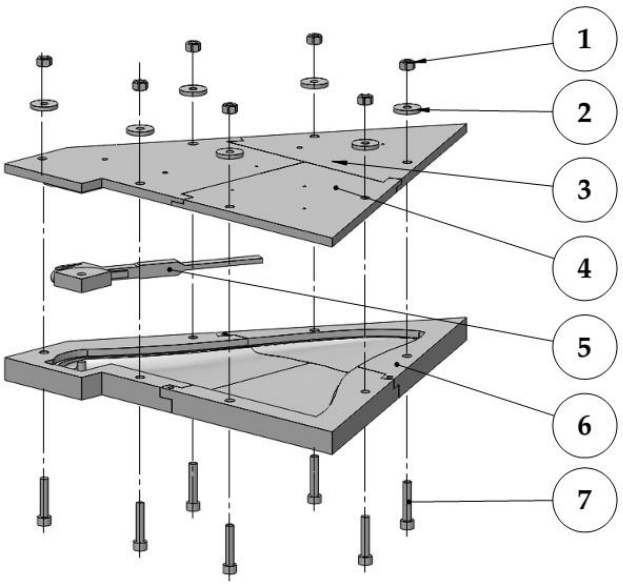

1	Nuts
2	Washers
3	Holes on the superior mold for material spilling
4	Superior mold
5	Core
6	Inferior mold
7	Screws

Figure 5.8: Fin mold assembly

Figure 5.9: The two fins with the two different sticks

Figure 5.10: Fins assembled on the main body

5.3 Electronic cabling

The cabling of the electronic components deals with two problems: the small space inside the box and the large amount of cables.

In order to facilitate the cabling operations, the cables are soldered to some connectors that groups together the adjacent cables. For example, the connector in Figure 5.11 groups all the cables of the camera. It is also possible to notice how, during the soldering, a preferred direction was given to the cables, in order to minimize the required space.

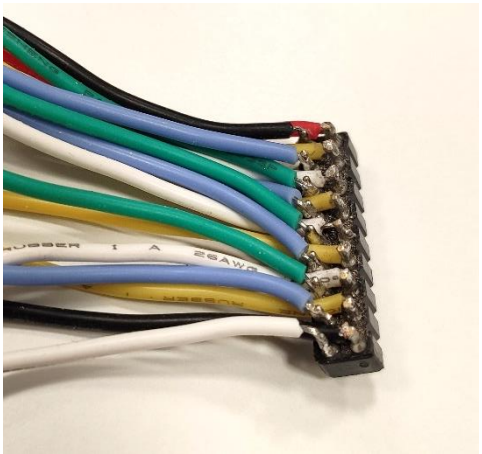

Figure 5.11: Camera connector

The use of this connectors allows to plug and unplug all the components with few moves. It also reduces the needed length for the cables, saving space and weight.

In Figure 5.13 is shown the complete scheme of the cabling. The colors of the cables are the same used in the real circuit. The only exception are the power cables, divided on the scheme between 3.3V or 5V (red) and 7.4V (red and white dashed).

The two batteries are connected in series. The positive pole, the ground and the balance cable, needed for the charging, are wired to three poles of the IP68 connector in the rear part of the robot. The same power and ground cables are linked to a multiple plug socket (Figure 5.12) to which are connected the Arduino and the four servomotors. On the power cable there are the switch to open the circuit and the ammeter to measure the current supplied by the batteries.

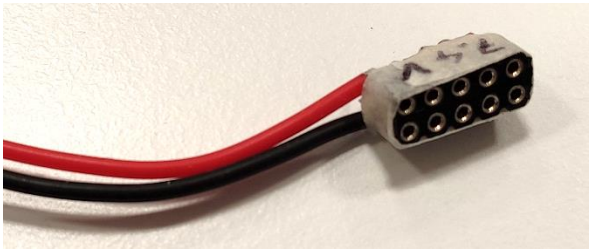

Figure 5.12: 7.4V multiple plug socket

A second multiple plug pocket is needed to supply the 3.3V to the IMU, to the camera and to the ESP8266-01. Both the SD card reader and the ammeter requires 5V power, but the SD card uses the available pin on the SPI interface in the central part of the Arduino.

The IMU and the camera uses the I2C bus to communicate with Arduino. A third multiple plug socket is used to connect both of them to the SDA and SCL pins.

The external connector has seven pins. Three of them are connected to the batteries as previously explained, the other four are connected to the USB programming port of the Arduino DUE.

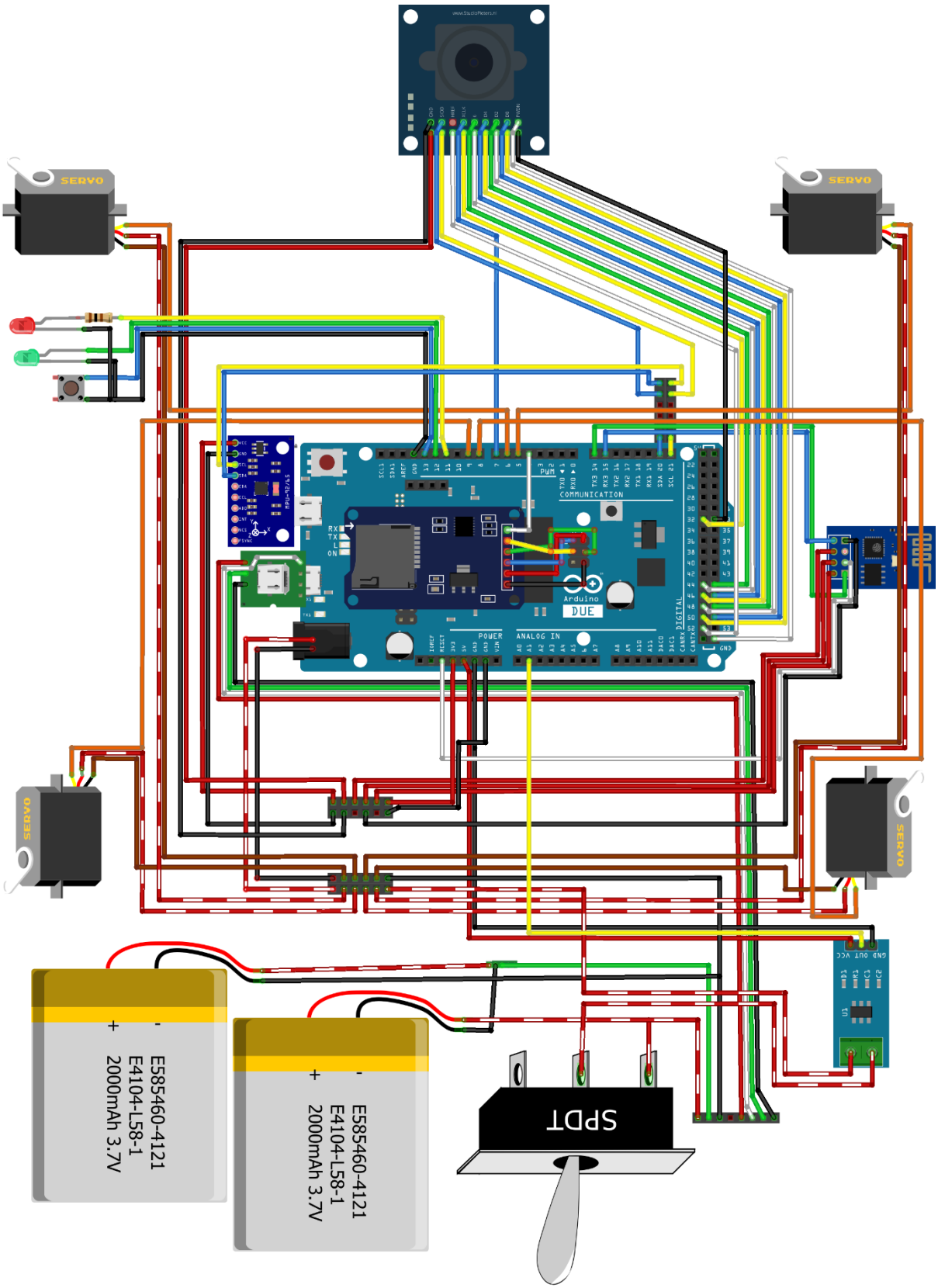

Figure 5.13: Cabling scheme

6. Use of the robot

The aim of the robot is to use it mainly in the laboratory for prototyping and testing. These activities require some interaction with robot itself. The user should be able to access the microcontroller without the fins starting flapping. They should be able to easily access the data stored in the SD card. At the same time, the robot should be easy to use without a computer during the tests in a swimming pool.

For all this purposes some features have been insert in the code in order to have a "user friendly" robot.

6.1 Running mode

During the simple running phase, the user interacts with the robot with the switch, the button and the two LEDs.

The switch opens and closes the battery circuit, switching on the Arduino and supplying current to the robots.

The button on the top of the manta is a momentary button, programmed to act as a logical on-off switched. When it is turned on, the robot fins start flapping, according to the programmed movement. In the same time, a new file is created on the SD card, and the data from the IMU, the ammeter and the camera[33] are stored. The naming of the files follows a sequential order.

The two LEDs on the back of the robot indicate the state. When powered, the Arduino starts the booting. After the initializing phase the red led switches on. In this state, the ESP module is powered, and Wi-Fi communication can be established. The two pectoral fin motors go to the horizontal position, so that the fins can be changed knowing the exact orientation of mounting.

[33] By the time this thesis is being written, the camera is not implemented yet.

If the button is pressed, the red LED switches off and the green LED switches on.

Sometimes, during the booting phase, the initialization of the IMU or the SD reader fails. In this case the red LED starts blinking.

6.2 Serial communication

Serial communication between the computer and the microcontroller can be performed both via USB and via Wi-Fi.

Due to the limitations of Arduino DUE (see paragraph 3.1) the flashing of programs on the microcontroller can be done only via USB. For this purpose, the connector on the rear part of the manta is connected to Arduino programming port. If the switch is off, the USB cable powers the Arduino but not the motors. In this way, it is possible to move the caudal fin to easily access the connector.

On the Wi-Fi module ESP8266-01 is installed the firmware esp-link by Jeelabs[34]. This firmware creates a web server with some interesting features. For the purposes of this project, the only interesting features are the Wi-Fi settings and the microcontroller console.

When the ESP module is powered, it generates a Wi-Fi network called "Manta_ray_AP" (Figure 6.1a). The user can connect to this network from any device and browse to the address http://192.168.4.1/ and find the home page of the esp-link server (Figure 6.1b).

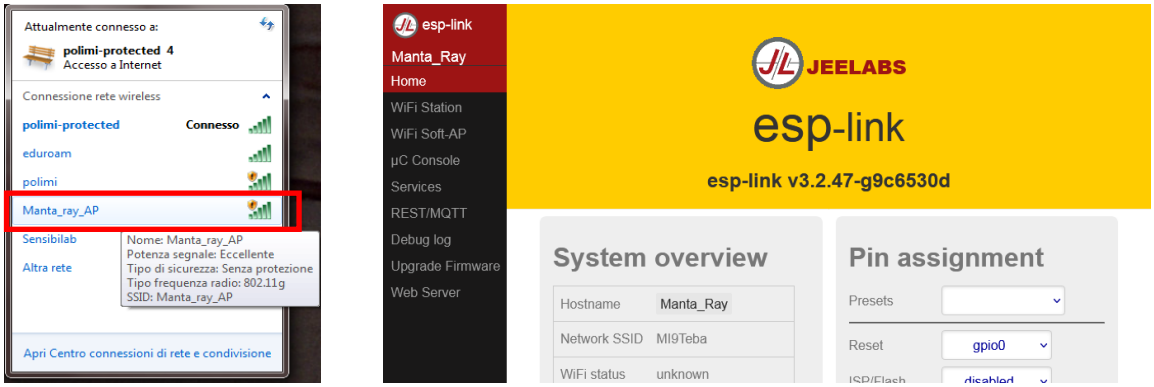

(a) Network SSID (b) The server home page

Figure 6.1: The Wi-Fi network from the robot

[34] Documentation available at https://github.com/jeelabs/esp-link, last visited on 02/11/2021.

From the menu on the left is possible to browse the different pages of the server. From "WiFi Soft-AP" the settings of the Wi-Fi network generated from the manta can be changed, such as name, protection, number of allowed connections.

From "WiFi Station" is possible to change the Wi-Fi mode to STA and connect the ESP to an existing network. Doing this, the network "Manta_ray_AP" will be no longer available, and the server page can be accessed by any device connected to the same network by browsing to the address http://192.168.43.9/. This mode would be useful for domestic applications, but for the scope of the robot it has not been applied.

The "μC Console" page allows to control the microcontroller to which the ESP module is cabled. From here is possible to reset the microcontroller, to receive and send messages through a serial port. In this project the ESP is connected to the serial 3. To fulfill the requirements listed at the beginning of this paragraph, a sort of user interface has been programmed on this serial port.

6.3 User interface

After the resetting, the welcome message from the Manta Ray appears (Figure 6.2). It indicates that everything on the Arduino is set up correctly. Below the welcome message, the inscription "User: " indicates that the robot is waiting for a command from the user. The commands can be written in the line "Console entry" below the console window. The command will appear on the screen and the robot will execute the command.

Typing "Help" a list of the available command appears. So far, the commands concern two aspect of the user experience: the file management and the parameters control.

On the SD card there is a folder named "RUNdata". Here are stored the .txt files that contains the records from all the sensors. So far, the file contains in columns the time instant, the values from the IMU and the value from the ammeter measured at that time instant. Each file is named "RUNxxx.txt", where xxx is the number of the run, between 001 and 999.

The command "FileList" shows a list of the available files. The command "PrintFile" asks which file the user is interested in. The user has to type the number and the content of the corresponding file is shown on the command window. In this way, it is possible to copy and paste the data to store them on the PC. Finally, the command "DeleteFile" allows to erase a specified file from the memory, or all the files together.

The control law of the robot is based on a series of parameter. During the testing phase could be useful to change the parameters to see their effect on the robot behavior. To do so without the necessity to flash the Arduino at every parameter change, the values

of the parameters are stored on the SD card. In the SD folder named “PARAM” each parameter is saved as a txt file. The Arduino reads the files and assigns the value to the corresponding variable.

The command “Parameters” shows on the Console window the list of parameters and their value. The command “ChangeParameter” asks for the parameter to change, asks the new value, and then substitutes the file on the SD with a new one containing the new value. Then the variable is initialized again and the robot starts following the trajectory according to the new parameters.

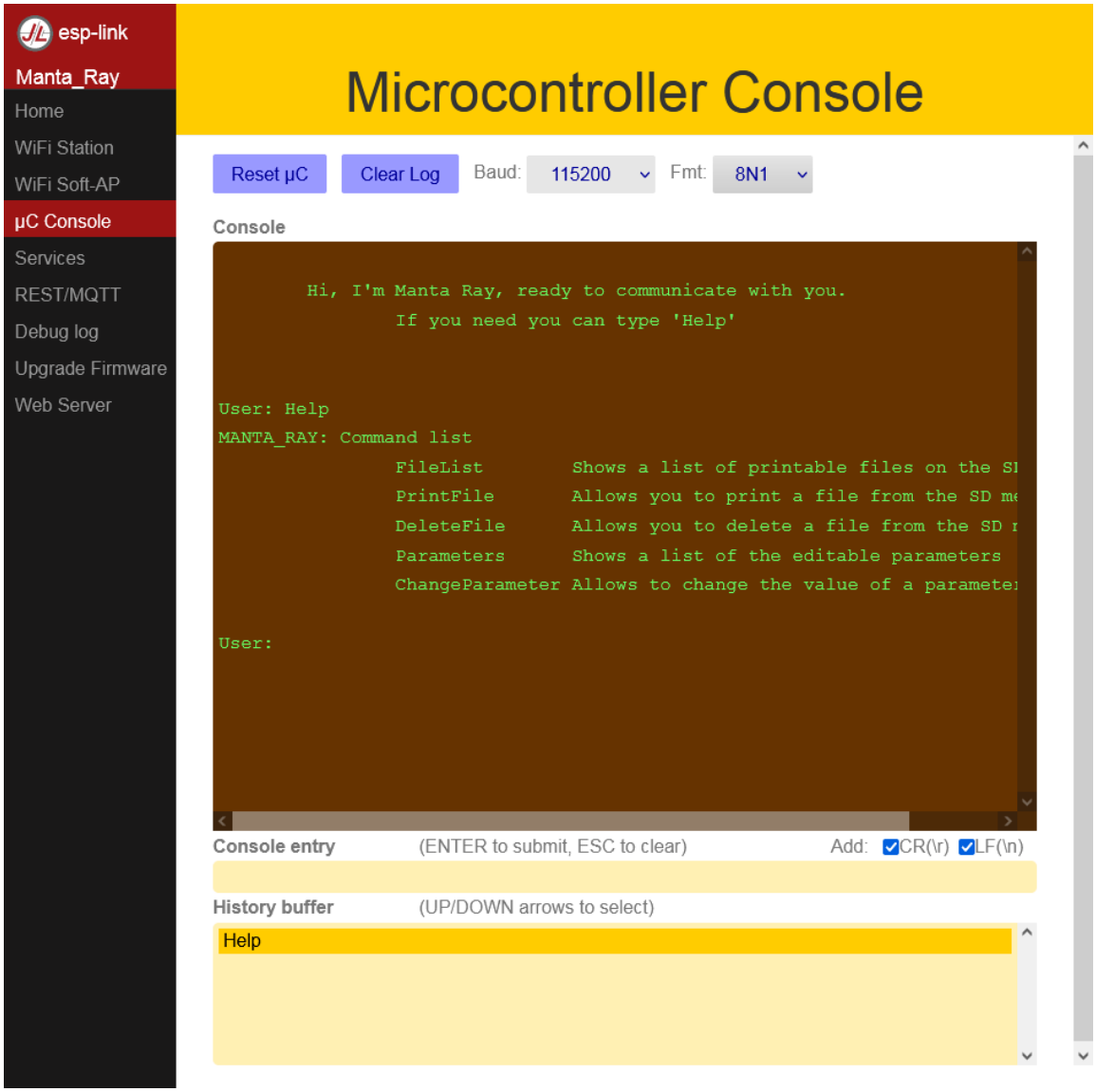

Figure 6.2: Welcome message and Help menu

7. Conclusion and future development

The research work presented in this thesis describes the design and the manufacturing of the working prototype of bioinspired autonomous underwater vehicle shown in Figure 7.1. The bioinspiration comes from the Manta Ray, for the capability of the fish to have great autonomy and maneuverability.

The robot was designed from scratch and manufactured in the laboratory. The basic principle of this prototype is to use two flexible pectoral fins to generate thrust. This solution is innovative with respect to the other manta ray robots developed at Polimi that actively control fin deformation.

The main purpose of this robot is experimenting the capability of flexible fins to generate thrust, and the whole design of the prototype is oriented to assist this function. The main body of the robot has limited dimensions, in order to be easy to handle and to test in a small swimming pool. The external shape is an airfoil profile in order to minimize water resistance during swimming. The fins are easy to change, thanks to the accessible front motors.

The Arduino microcontroller and the other electronic components are chosen in order to fit in the small dimensions and, at the same time, guarantee all the necessary functions.

A simplified user interface has been developed exploiting ESP-link firmware to assist testing. The user can interact with the robot via Wi-Fi and access the data and the parameters from the serial monitor. These functions are integrated in the code of the robot.

Finally, a fin has been developed and manufactured. Its design is based on some general principles and a primitive finite element model. The comparison between the finite element model and the physical fin allows to refine the FEA model and use it for future work.

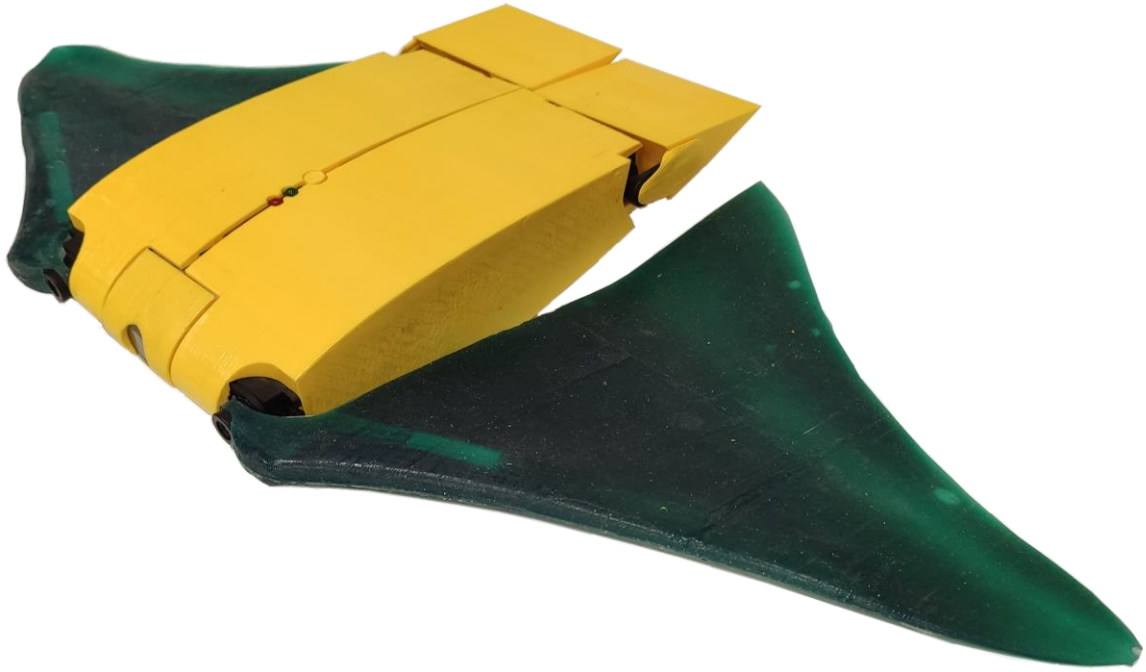

Figure 7.1: Photo of the finished robot

The future developments of this research involve both the control of the robot movements and the design of the fins.

The first step to control the robot is to program the movement of the caudal fins in order to stabilize the flapping oscillations. Later, a trajectory following strategy could be developed. This last control could take advantage of the studies on fin thrust generation for a feedforward trajectory generation.

The fin design can be both analytical and experimental. The finite element model introduced in this thesis could be refined and validated by experiments, in order to exploit it for an analytical optimization of fin design. In the same time, a test bench for measuring the thrust generated by different fins could be a practical way to analyze how the different parameters of the fin shape influences their performance.

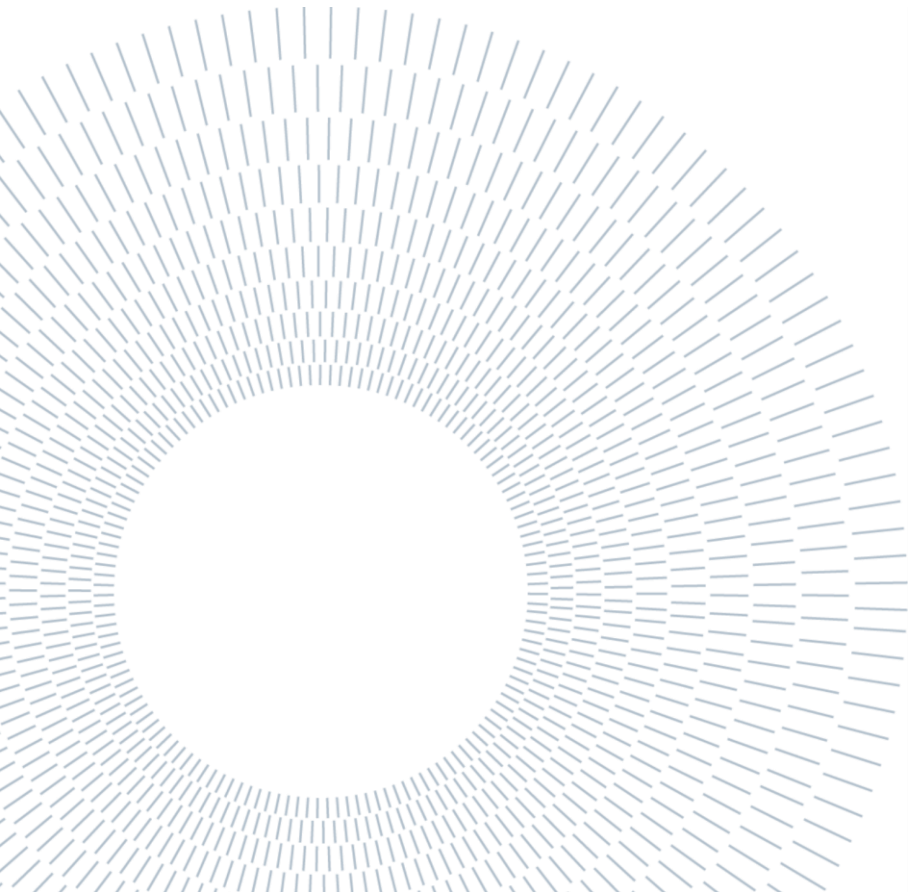

Bibliography

[1] C. Zhou and K.-H. Low, "Better Endurance and Load Capacity: An Improved Design," *Journal of Bionic Engineering,* no. 7, pp. 137-144, 2010.

[2] M. Ikeda, S. Hikasa, K. Watanabe and I. Nagai, "A pectoral fin analysis for diving rajiform-type fish robots by fluid dynamics," *Artif Life Robotics,* vol. 19, pp. 136-141, 2014.

[3] G. Li, Y. Deng, O. L. Osen, S. Bi and H. Zhang, "A Bio-inspired Swimming Robot for Marine Aquaculture Applications: from Concept-design to Simulation," April 2016.

[4] K. H. Low and A. Willy, "Biomimetic Motion Planning of an Undulating Robotic Fish Fin," Singapore, 2006.

[5] Y. Zhang, J. He e K. H. Low, «Parametric Study of an Underwater Finned Propulsor Inspired by Bluespotted Ray,» *Journal of Bionic Engineering,* n. 9, p. 166–176 , 2012.

[6] J. J. Long, "Biomimetics: Robotics Based on Fish Swimming," Elsevier, Vassar College, Poughkeepsie, NY, USA, 2011.

[7] Y. Wang, J. Tan and D. Zhao, "Design and Experiment on a Biomimetic Robotic Fish Inspired by Freshwater Stingray," *Journal of Bionic Engineering,* no. 12, pp. 204-216, 2015.

[8] C.-M. Chew, Q.-Y. Lim and K. Yeo, "Development of Propulsion Mechanism for Robot Manta Ray," in *2015 IEEE Conference on Robotics and Biomimetics*, Zhuhai, China, December 6-9, 2015.

[9] Y. Cai, S. Bi and L. Zheng, "Design Optimization of a Bionic Fish with Multi-Joint Fin Rays," *Advanced Robotics,* no. 26, p. 177–196, 2012.

[10] F. Veenstra, J. Jørgensen and S. Risi, "Evolution of Fin Undulation on a Physical Knifefish-inspired Soft Robot," in *GECCO '18: Genetic and Evolutionary Computation Conference*, Kyoto, Japan, July 15–19, 2018.

[11] M. Epstein, J. E. Colgate and M. A. MacIver, "Generating Thrust with a Biologically-Inspired Robotic Ribbon Fin," in *2006 IEEE/RSJ International Conference on Intelligent Robots and Systems*, Beijing, China, October 9 - 15, 2006.

[12] H. Liu and O. Curet, "Swimming performance of a bio-inspired robotic vessel with undulating fin propulsion," *Bioinspiration & Biomimetics,* vol. 13, 2018.

[13] K. H. Low, «Locomotion Simulation and System integration of Robotic Fish with Modular Ondulating Fin,» *International Journal of Modelling and Simulation,* vol. 7, n. 8.

[14] T. Hu, L. Shen, L. Lin and H. Xu, "Biological inspirations, kinematics modeling, mechanism design and experiments on an undulating robotic fin inspired by Gymnarchus niloticus," *Mechanism and Machine Theory,* no. 44, p. 633–645, 2009.

[15] M. Ikeda, K. Mikuriya, K. Watanabe, S. Hikasa, Y. Hamano e I. Nagai, «Infuence on the propulsive performance due to the diference in the fin shape of a robotic manta,» *Artif Life Robotics,* n. 22, p. 276–282, 2017.

[16] L. Shang, S. Wang, M. Tan and L. Cheng, "Swimming locomotion modeling for biomimetic underwater vehicle with two undulating longfins," *Robotica,* vol. 30, pp. 913- 923, October 2012.

[17] M. B. Khan and P. Smithmaitrie, "Design and Fabrication of a 3-Fin Symmetric Ray-Inspired Soft Robot for Underwater Exploration," *International Journal of Mechatronics and Applied Mechanics,* no. Issue 4, 2018.

[18] Y. Cai, S. Bi and L. Zhang, "Design and implication of a bionic pectoral fin imitating cow-nosed ray," in *The 2010 IEEE/RSJ International Conference on Intelligent Robots and Systems*, Taipei, Taiwan, October 18-22, 2010.

[19] Y. Cai, S. Bi, G. Li, H. P. Hildre and H. Zhang, "From Natural Complexity to Biomimetic Simplification: The Realization of Bionic Fish Inspired by the Cownose Ray," *IEEE Robotics and Automation Magazine,* no. 26, pp. 27 - 38, September. 2019.

[20] Y. Cai, S. Bi and L. Zheng, "Design and Experiments of a Robotic Fish Imitating Cow-Nosed Ray," *Journal of Bionic Engineering,* no. 7, p. 120–126, 2010.

[21] Y. Zhang, S. Wang, X. Wang and Y. Geng, "Design and Control of Bionic Manta Ray Robot With Flexible Pectoral Fin," in *14th International Conference on Control and Automation (ICCA)*, Anchorage, Alaska, USA, June 12-15, 2018.

[22] K. H. Low, C. Zhou, G. Seet, S. Bi and Y. Cai, "Improvement and Testing of a Robotic Manta Ray (RoMan-III)," in *2011 IEEE International Conference on Robotics and Biomimetics*, Phuket, Thailand, December 7-11, 2011.

[23] W. Chi and K. H. Low, "Review and Fin Structure Design fir Robotic Manta Ray (RoMan IV)," *Journal of Robotics and Mechatronics,* vol. 24, no. 4, pp. 620-628, 2012.

[24] H. Ma, Y. Cai, Y. Wang, S. Bi and Z. Gong, "A biomimetic cownose ray robot fish with oscillating and chordwise twisting flexible pectoral fins," *Industrial Robot: An International Journal,* no. 42, pp. 214-221, 2015.

[25] Festo AG & Co. KG, "Air_ray | Festo Corporate," [Online]. Available: https://www.festo.com/group/en/cms/10245.htm. [Accessed 20 October 2021].

[26] J. Gao, S. Bi and C. Liu, "Development and Design of a Robotic Manta Ray Featuring Flexible Pectoral Fins," in *2007 IEEE International Conference on Robotics and Biomimetics*, Sanya, China, December 15 -18, 2007.

[27] C.-M. Chew, S. Arastehfar, G. Gunawan and K. S. Yeo, "Study of Sweep Angle Effect on Thrust Generation of Oscillatory Pectoral Fins," in *2017 IEEE/RSJ International Conference on Intelligent Robots and Systems (IROS)*, Vancouver, BC, Canada, September 24–28, 2017.

[28] NUSnews, «NUS-developed manta ray robot swims faster and operates up to 10 hours,» 08 November 2017. [Online]. Available: https://news.nus.edu.sg/nus-developed-manta-ray-robot-swims-faster-and-operates-up-to-10-hours/. [Consultato il giorno 05 October 2021].

[29] Z. Chen, T. I. Um, J. Zhu and H. Bart-Smith, "Bio-Inspired Robotic Cownose Ray Propelled by Electroactive Polymer Pectoral Fin," in *ASME 2011 International Mechanical Engineering Congress & Exposition*, Denver, Colorado, USA, 2011.

[30] G. H. Franzini, N. Schmidt, J. F. Fuller and J. H. Price, "Manta Ray Robot," Worcester Polytechnic Institute, 2016.

[31] Festo AG & Co. KG, "Aqua_ray | Festo Corporate," [Online]. Available: https://www.festo.com/group/en/cms/10246.htm. [Accessed 20 October 2021].

[32] Arduino , "Arduino Due - Arduino Official Store," [Online]. Available: https://store.arduino.cc/collections/boards/products/arduino-due#. [Accessed 23 October 2021].

[33] M. Ziegler, M. Hoffmann, J. P. Carbajal and R. Pfeifer, "Varying Body Stiffness for Aquatic Locomotion," Artificial Intelligence Laboratory, Department of Informatics, University of Zurich, Zurich, Switzerland.

[34] P. Riggs, A. Bowyer and J. Vincent, "Advantages of a Biomimetic Stiffness Profile in," *Journal of Bionic Engineering,* no. 7, p. 113–119, 2010.

[35] J. S. Carlton, in *Propeller blade vibration in Marine Propeller and Propulsion*, 3rd ed. ed., Oxford, UK, Butterworth-Heinemann, 2012, pp. ch. 21, pp. 430-431.

[36] G. Bianchi, S. Cinquemani and F. Resta, "A bio-inspired design of underwater robot exploiting fin undulation propulsion," Milano, 2021.

A. Appendix A – Current measures

Current measures $[A]$, $\omega = 0 \left[\frac{rad}{s}\right]$										
$M[kg]$	#1	#2	#3	#4	#5	#6	#7	#8	#9	#10
0	0	0	0	0	0	0	0	0	0	0
0.5	0	0	0	0	0	0	0	0	0	0
1	0.2758	0.2761	0.2763	0.2785	0.2768	0.2766	0.2798	0.2767	0.2777	0.2776
1.5	0.4208	0.4228	0.4224	0.4267	0.4261	0.4297	0.4310	0.4319	0.4331	0.4321
2	0.4421	0.4386	0.4424	0.4396	0.4410	0.4389	0.4381	0.4408	0.4446	0.4391
2.5	0.5796	0.5952	0.6070	0.5959	0.5919	0.5719	0.5671	0.5692	0.5981	0.5902
3	0.4489	0.4498	0.4523	0.4520	0.4504	0.4512	0.4492	0.4440	0.4396	0.4483
$M[kg]$	#11	#12	#13	#14	#15	#16	#17	#18	#19	#20
0	0	0	0	0	0	0	0	0	0	0
0.5	0	0	0	0	0	0	0	0	0	0
1	0.2778	0.2793	0.2795	0.2824	0.2802	0.2800	0.2802	0.2811	0.2790	0.2532
1.5	0.4332	0.4330	0.4324	0.4308	0.4307	0.4297	0.4295	0.4287	0.4293	0.4269
2	0.4455	0.4441	0.4439	0.4450	0.4402	0.4467	0.4456	0.4441	0.4434	0.4451
2.5	0.5924	0.5869	0.5776	0.5872	0.5940	0.5738	0.5231	0.5584	0.5218	0.5666
3	0.4468	0.4517	0.4567	0.4523	0.4567	0.4541	0.4519	0.4538	0.4571	0.4537

Table A-1: Current measures at ω=0 rad/s

Current measures $[A]$, $\omega = 0.3142 \left[\frac{rad}{s}\right]$										
$M[kg]$	#1	#2	#3	#4	#5	#6	#7	#8	#9	#10
0	0.0884	0.0989	0.1003	0.1002	0.0997	0.1029	0.0981	0.1003	0.1012	0.0992
0.5	0.2145	0.2200	0.2195	0.2185	0.2213	0.2186	0.2176	0.2139	0.2219	0.2117
1	0.3471	0.3487	0.3505	0.3469	0.3524	0.3517	0.3533	0.3440	0.3404	0.3527
1.5	0.5004	0.5113	0.5115	0.5210	0.5151	0.5278	0.5217	0.5317	0.5115	0.5087
2	0.6423	0.6797	0.6392	0.6327	0.6674	0.6620	0.6573	0.6440	0.6455	0.6456
2.5	0.8014	0.7017	0.7916	0.7914	0.6886	0.7731	0.9674	0.6823	0.7914	0.8230
3	0.8077	0.7945	0.8876	0.7809	0.8229	0.7610	0.9277	0.8167	0.8038	0.8214
$M[kg]$	#11	#12	#13	#14	#15	#16	#17	#18	#19	#20
0	0.0978	0.1015	0.0975	0.1009	0.0990	0.1003	0.0984	0.1014	0.1002	0.1000
0.5	0.2128	0.2139	0.2162	0.2124	0.2111	0.2085	0.2142	0.2130	0.2192	0.2193
1	0.3207	0.3428	0.3328	0.3467	0.3331	0.3358	0.3428	0.3357	0.3376	0.3273
1.5	0.5252	0.5129	0.5193	0.5436	0.4942	0.5227	0.5272	0.5346	0.5065	0.5178
2	0.6366	0.6463	0.6403	0.6424	0.6628	0.6566	0.6391	0.6584	0.6493	0.6476
2.5	0.7330	0.7047	0.7188	0.7934	0.7724	0.7435	0.7989	0.8176	0.7920	0.7883
3	0.8956	0.8626	0.8263	0.8625	0.8887	0.8898	0.8241	0.8808	0.8430	0.8621

Table A-2: Current measures at ω=0.3142 rad/s

Current measures $[A]$, $\omega = 0.5236 \left[\frac{rad}{s}\right]$										
$M[kg]$	#1	#2	#3	#4	#5	#6	#7	#8	#9	#10
0	0.1046	0.1039	0.1045	0.1016	0.1052	0.1036	0.1067	0.1034	0.1024	0.1045
0.5	0.2230	0.2250	0.2282	0.2224	0.2269	0.2409	0.2306	0.2267	0.2271	0.2308
1	0.3225	0.3415	0.3482	0.3489	0.3528	0.3525	0.3439	0.3302	0.3472	0.3467
1.5	0.4979	0.5138	0.5118	0.5221	0.5254	0.5251	0.5164	0.5153	0.5118	0.5211
2	0.6292	0.6335	0.6334	0.6385	0.6392	0.6362	0.6032	0.6311	0.6338	0.6352
2.5	0.8214	0.8264	0.8269	0.8424	0.8106	0.8235	0.7745	0.7899	0.8247	0.8352
3	0.9003	0.8964	0.9811	0.9164	0.9630	0.9825	0.9516	0.8779	0.9013	0.9331
$M[kg]$	#11	#12	#13	#14	#15	#16	#17	#18	#19	#20
0	0.1020	0.1038	0.1044	0.1051	0.1053	0.1022	0.1032	0.1048	0.1034	0.1100
0.5	0.2261	0.2249	0.2045	0.2158	0.2146	0.2180	0.2163	0.2110	0.2142	0.2153
1	0.3509	0.3455	0.3467	0.3487	0.3448	0.3476	0.3435	0.3476	0.3525	0.3576
1.5	0.5224	0.5130	0.4991	0.5018	0.5136	0.5126	0.5226	0.5202	0.5099	0.4983
2	0.6404	0.5779	0.6516	0.6705	0.6431	0.6633	0.6815	0.6338	0.6449	0.6429
2.5	0.8335	0.8162	0.7995	0.8261	0.7991	0.8424	0.8395	0.8345	0.8151	0.8237
3	0.9658	0.9648	0.8939	0.8530	0.8861	0.9673	1.0043	0.8809	0.9297	0.9295

Table A-3: Current measures at ω=0.5236 rad/s

Current measures $[A]$, $\omega = 1.5708 \left[\frac{rad}{s}\right]$										
$M[kg]$	#1	#2	#3	#4	#5	#6	#7	#8	#9	#10
0	0.146	0.148	0.143	0.148	0.145	0.141	0.152	0.142	0.150	0.139
0.5	0.27	0.26	0.25	0.24	0.27	0.29	0.28	0.30	0.29	0.28
1	0.41	0.42	0.36	0.42	0.39	0.41	0.44	0.42	0.44	0.45
1.5	0.60	0.61	0.51	0.67	0.53	0.51	0.72	0.42	0.54	0.51
2	0.73	0.71	0.73	0.70	0.72	0.70	0.71	0.70	0.71	0.68
2.5	0.95	0.85	0.81	0.80	0.82	0.81	0.81	0.83	0.84	0.82
3	0.92	0.94	0.96	0.94	0.96	0.95	0.96	0.98	0.96	0.97
$M[kg]$	#11	#12	#13	#14	#15	#16	#17	#18	#19	#20
0	0.165	0.148	0.138	0.163	0.154	0.115	0.148	0.138	0.125	0.142
0.5	0.25	0.28	0.27	0.25	0.24	0.27	0.30	0.27	0.28	0.270
1	0.44	0.40	0.41	0.42	0.44	0.42	0.46	0.41	0.43	0.40
1.5	0.72	0.42	0.54	0.71	0.41	0.49	0.69	0.50	0.52	0.45
2	0.74	0.70	0.71	0.77	0.71	0.70	0.71	0.69	0.71	0.69
2.5	0.83	0.82	0.81	0.84	0.83	0.82	0.81	0.81	0.82	0.81
3	0.95	0.93	0.98	0.96	0.97	0.98	0.95	1.00	0.98	0.97

Table A-4: Current measures at ω=1.5708 rad/s

Current measures $[A]$, $\omega = 3.1416 \left[\frac{rad}{s}\right]$										
$M[kg]$	#1	#2	#3	#4	#5	#6	#7	#8	#9	#10
0	0.37	0.42	0.49	0.31	0.28	0.23	0.19	0.27	0.26	0.24
0.5	0.41	0.38	0.35	0.34	0.36	0.35	0.34	0.44	0.38	0.36
1	0.55	0.49	0.46	0.45	0.44	0.45	0.43	0.49	0.46	0.45
1.5	0.57	0.58	0.57	0.58	0.59	0.58	0.62	0.59	0.58	0.57
2	0.69	0.70	0.68	0.69	0.70	0.69	0.70	0.69	0.68	0.71
2.5	0.83	0.81	0.83	0.82	0.83	0.84	0.82	0.81	0.82	0.84
3	0.94	0.95	0.92	0.96	0.98	0.94	0.97	0.93	0.95	0.94
$M[kg]$	#11	#12	#13	#14	#15	#16	#17	#18	#19	#20
0	0.23	0.38	0.29	0.25	0.22	0.23	0.24	0.23	0.24	0.22
0.5	0.43	0.38	0.35	0.35	0.34	0.39	0.36	0.35	0.34	0.34
1	0.44	0.45	0.44	0.45	0.45	0.44	0.45	0.44	0.38	0.42
1.5	0.58	0.57	0.58	0.56	0.58	0.57	0.58	0.60	0.58	0.60
2	0.70	0.68	0.69	0.68	0.69	0.68	0.69	0.68	0.69	0.68
2.5	0.83	0.82	0.84	0.83	0.81	0.83	0.82	0.83	0.82	0.81
3	0.95	0.96	0.95	0.96	0.97	0.96	0.93	0.96	0.95	0.97

Table A-5: Current measures at ω=3.1416 rad/s

B. Appendix B – Pectoral fin surface

Fin external profile. Spline points coordinates [mm]								
x	0.00	9.10	17.16	24.70	33.80	41.60	49.40	57.72
y	0.00	7.80	17.16	28.60	41.08	54.60	67.60	81.90
x	65.26	73.32	81.38	89.44	97.76	106.08	114.14	122.20
y	98.80	113.88	130.26	149.76	166.40	180.70	192.92	202.80
x	130.00	138.06	141.96	146.12	150.28	154.18	158.08	162.24
y	210.60	216.06	219.70	220.22	220.22	219.70	215.28	186.68
x	166.40	170.56	174.72	178.62	182.52	186.68	190.84	195.00
y	165.88	149.50	135.98	126.36	118.30	107.90	98.80	93.60
x	203.32	211.12	219.44	226.98	235.30	243.62	251.68	260.00
y	81.38	68.12	55.38	44.20	32.50	20.80	10.92	0.00

Table B-1: Fin external profile

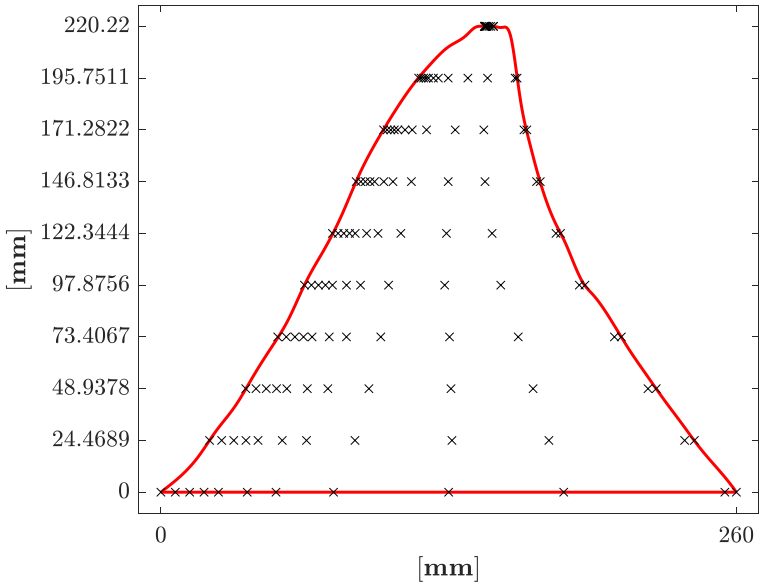

Figure B.1: Fin profile and control points

		Fin surface half thickness in control points [mm]											
		Leading edge			← Chordwise direction % →								Trail edge
		0	**2.5**	**5**	**7.5**	**10**	**15**	**20**	**30**	**50**	**70**	**98**	**100**
Tip	**100**	0	0.1	0.12	0.13	0.12	0.11	0.1	0.08	0.06	0.02	0.01	0
	88.9	0	1	1.2	1.5	1.5	1.4	1.2	1	0.7	0.5	0.3	0
← Spanwise direction % →	**77.8**	0	2	2.6	3	3	2.7	2.2	1.5	1	0.5	0.3	0
	66.7	0	2.7	3.3	3.5	3.5	2.9	2.6	1.8	1.3	0.5	0.3	0
	55.5	0	3	3.6	3.8	3.8	3.5	3	2	1.4	0.6	0.4	0
	44.4	0	3.5	4.5	4.6	4.5	4.2	3.2	2.2	1.5	0.6	0.4	0
	33.3	0	4	5.5	6	6	5	3.8	2.4	1.6	0.7	0.4	0
	22.2	0	4.5	6.2	7	7	5.8	4.2	2.6	1.7	0.8	0.4	0
	11.1	0	5	6.4	7	7	5.8	4.8	2.8	1.9	0.9	0.4	0
Base	**0**	0	5	6.4	7	7	6	5	3	2	1	0.4	0

Table B-2: Fin surface half thickness in control points

C. Appendix C – Fin modes of vibration

Fin with hybrid stick modes of vibration
Mode 1 Frequency: 2.1478 Hz 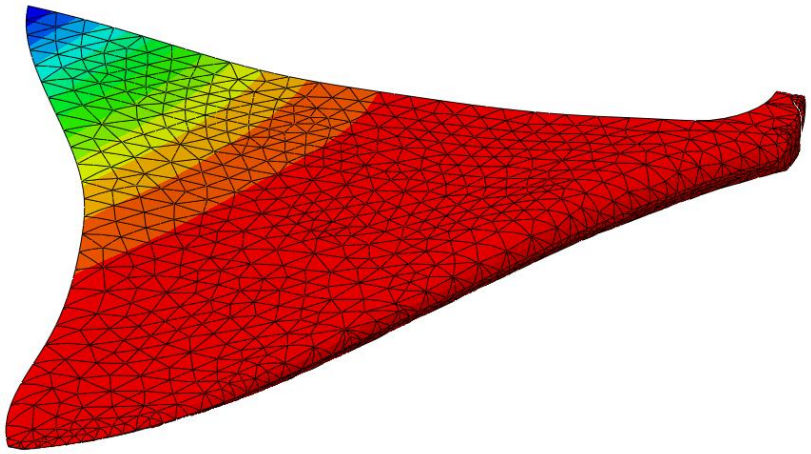   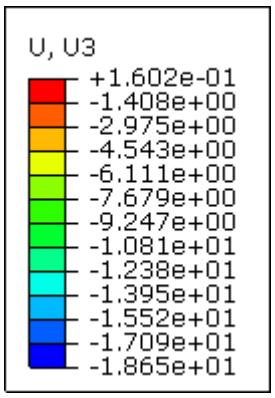
Mode 2 Frequency: 3.8314 Hz 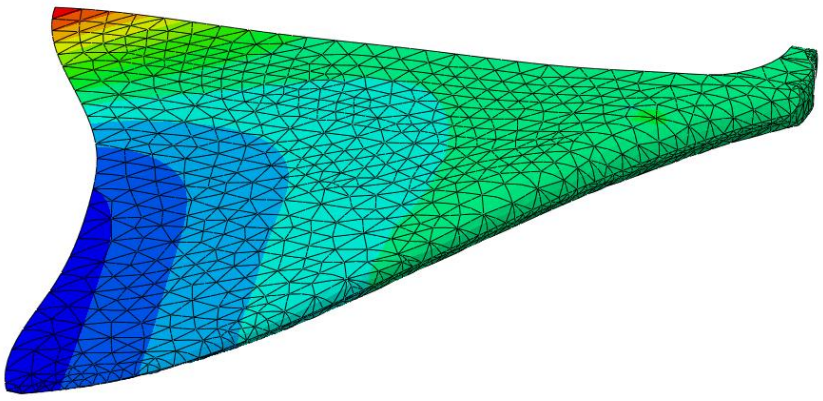   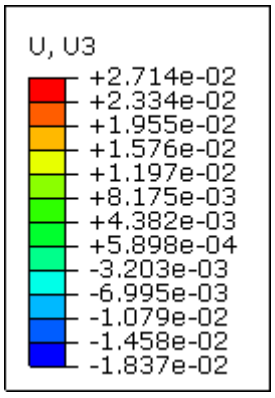

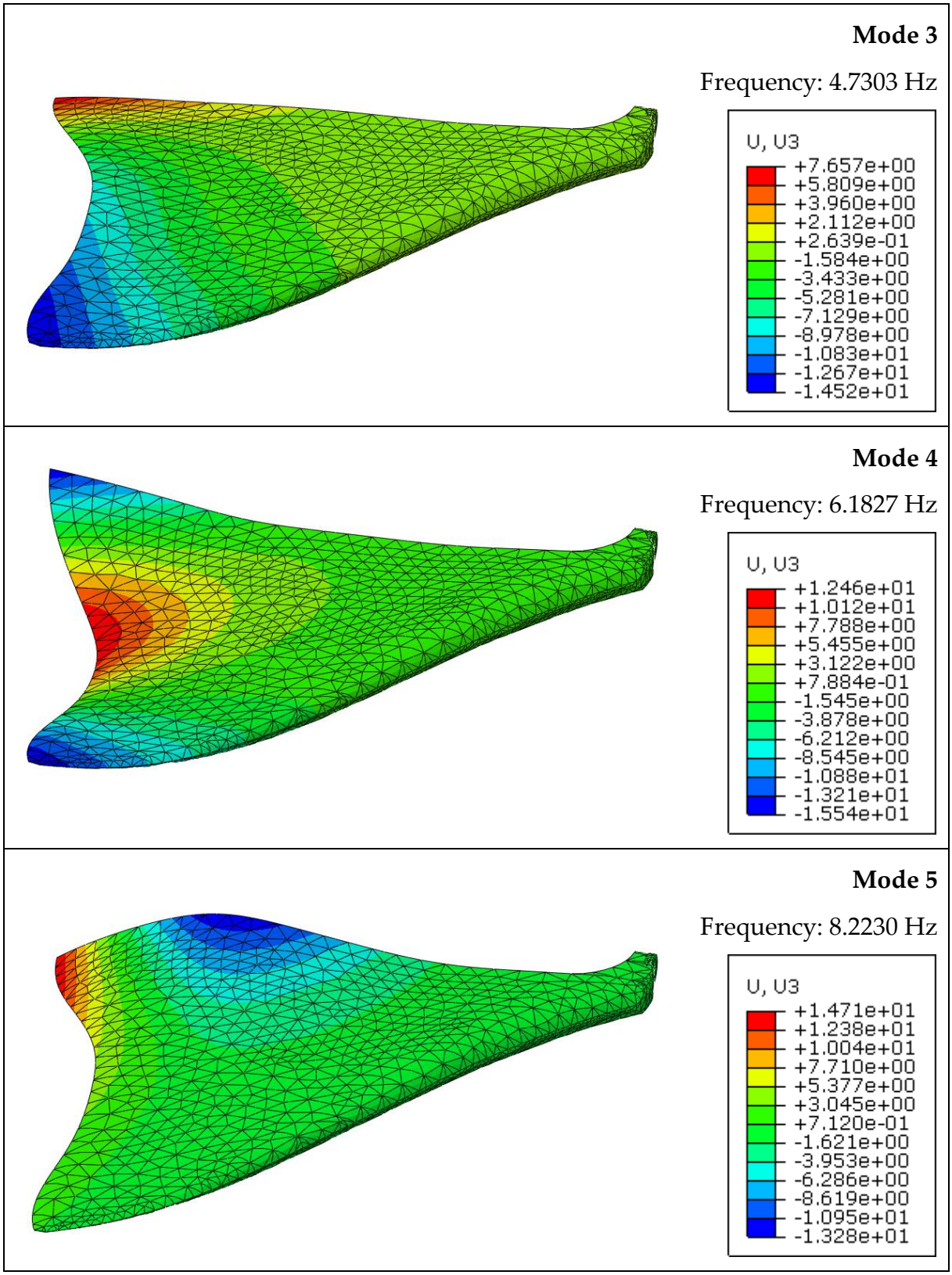

Figure C.1: Modes of vibration with the hybrid stick

List of Figures

List of Tables

List of Abbreviations

AUV	Autonomous Underwater Vehicle
FEA	Finite Elements Analysis
BCF	Body and/or Caudal Fin (locomotion)
MPF	Median and/or Paired Fin (locomotion)
DOFs	Degrees of freedom
CL	Chord length
IMU	Inertial Measurement Unit
CFD	Computational Fluid Dynamic
LPD	Layer Plastic Deposition